Panagiotis Herodotou

Design, Modelling and Experimental Evaluation of a Compact Actuator for a Portable Lower Extremity Exoskeleton

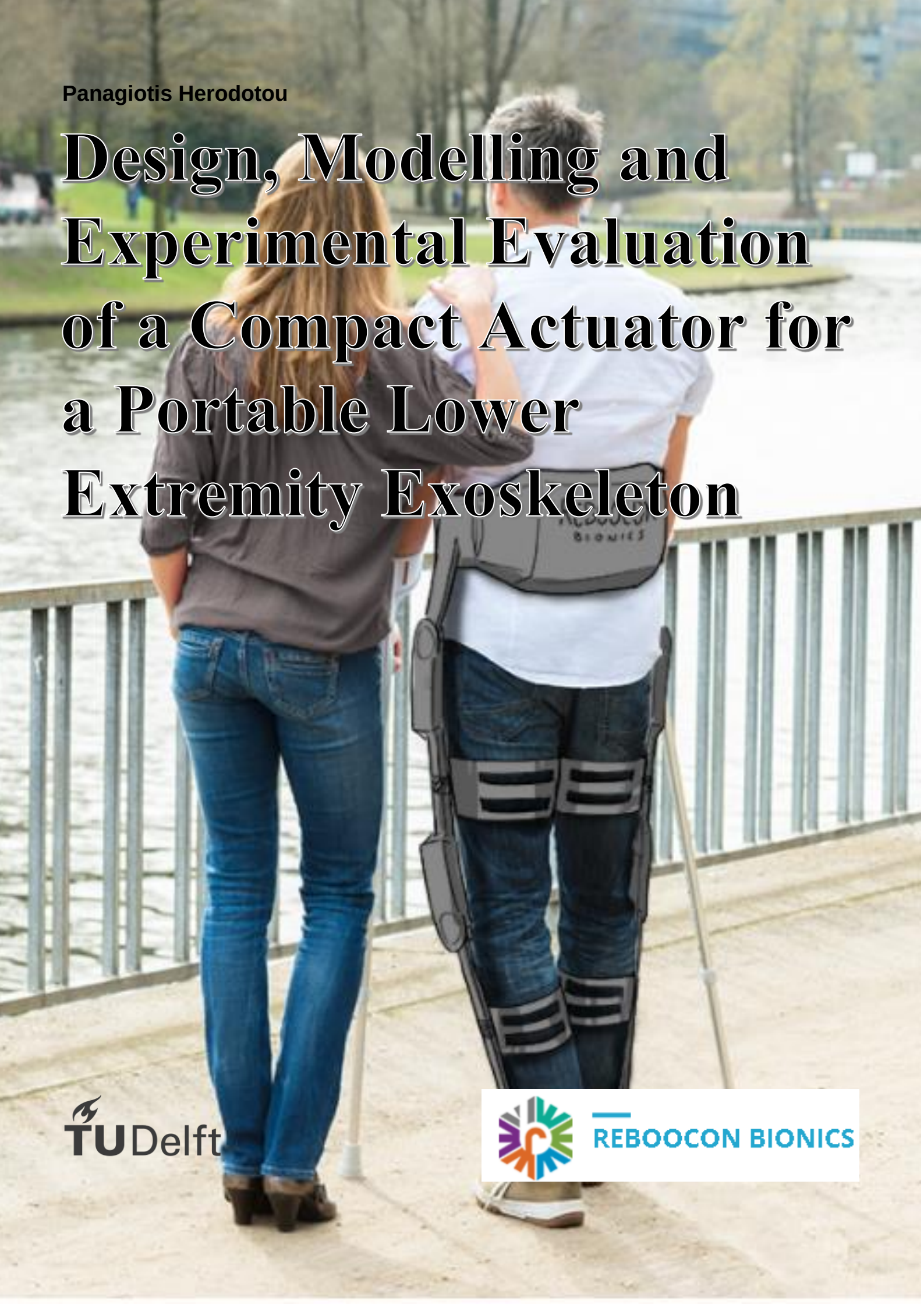

TU Delft

REBOOCON BIONICS

Design, Modelling and Experimental Evaluation of a Compact Actuator for a Portable Lower Extremity Exoskeleton

Thesis Report
By

Panagiotis Herodotou
Student ID: 4620445

in partial fulfilment of the requirements for the degree of

Master of Science
in Mechanical Engineering

at the Delft University of Technology,
to be defended on October 30, 2018 at 13:00 PM.

Supervisor:	Dr.ir. D.H. Plettenburg, TU Delft Ir. Shiqian Wang, Reboocon Bionics BV
Thesis committee:	Prof.dr. Frans C.T. van der Helm (Chair), TU Delft Dr.ir. D.H. Plettenburg, TU Delft Dr.ir. M. (Matthijs) Langelaar, TU Delft Ir. Shiqian Wang, Reboocon Bionics BV

Contents

Abstract

This paper presents the design and modelling of a Transmissive Force Sensing Elastic Actuator (TFSEA) for the hip and knee joints of a gait assisting exoskeleton. Powered Lower Extremity Exoskeletons (pLEE) can serve as rehabilitation devices or as orthotic devices enabling paraplegics to walk. Even though several exoskeletons have been commercialized, the existing exoskeletons' actuators are still not optimal, since they are facing significant challenges.

Some of these challenges are reducing the weight and size of the actuators, while still providing the required torque and power to produce desired joint trajectories. Also, they have limited performance and there are still torque sensing issues. Measuring output torque directly is quite difficult, thus it is measured indirectly, but often not so accurately.

Compliant actuators utilise springs for torque sensing and compliance with environment, but springs usually limits their torque bandwidth. Elastic elements increase safety by dampening impacts but can make control more difficult. Lastly, torque sensing usually has practical challenges, like determining the placement, attachment, and type of sensor.

The actuator's components can be configured in many different ways, producing designs with various trade-offs that affect power output, size, weight, efficiency and mechanical robustness. Considering these trade-offs, this project focuses on developing an optimal configuration which provides a compact, lightweight, high performance exoskeleton actuator, while attempting to solve practical challenges involving torque sensing.

Towards this direction, the following approach was followed:
After reviewing existing Series Elastic Actuator (SEA) technologies, a new spring configuration was proposed. This configuration places the spring between the gear and the housing and measures the transmitted torque to the load.

A dynamic model was developed for the proposed design and its frequency response was compared with other common SEA configurations. The simulation showed good torque transmissibility and sensitivity bandwidths. Detailed CAD designs were made for the concept and a prototype was produced.

A combination of structural simulations, along with a careful component selection resulted in a very compact and lightweight design. Tests were designed to measure and evaluate the performance of the actual system. The spring stiffness calibration test showed excellent linearity, and the desired stiffness was achieved. Lastly, a good torque resolution and high torque density were achieved.

Acknowledgements

This research took place in Reboocon Bionics BV and contains intellectual property of Reboocon Bionics. Deeply grateful to my company supervisor and CEO of Reboocon Bionics, Shiqian Wang for his valuable contribution and inspiration, as this project would never have been achieved without him. I would like to thank my supervisor Prof. Dick Plettenburg, my supervisor in TU Delft, for his valuable feedback and guidance. A word of thanks to Tengfei Sun for his assistance in the assembly and testing of the actuator. Acknowledgements to Arthur Ketels (Speciaal Machinefabriek Ketels v.o.f., the Netherlands) for providing custom-made PCB electronics for the encoders.

List of Tables

List of Figures

1 Introduction

1.1 Motivation and Objective

Portable exoskeletons are wearable robotic devices powered by active systems (actuators) that can produce predefined trajectories, based on the study of healthy person's movements, and assist or guide an impaired person execute a movement by providing assistance where needed.

In the recent years, exoskeletons have become quite useful in the field of medical rehabilitation and human augmentation. Many lower leg exoskeletons have been tested and have shown to improve the lives of paraplegics and patients with Spinal Cord Injury (SCI) by serving as orthotics to help with walking [1]–[3].

The exoskeleton can provide a certain level of autonomy to the paraplegics and SCI patients who currently use wheelchairs, by allowing them to walk independently [8]. Research showed that these systems can improve rehabilitation [1] [2]. Exoskeleton use requires only a little cognitive or energetic effort and decreases the risk of secondary injuries [3]. Such systems have already been commercialised with success such as Indego [2], ReWalk [5], and Ekso bionics [6].

A portable Lower Extremity Exoskeleton (pLEE) has to meet some criteria in order to be practical and successfully used by disabled people. It needs to be safe to use, have a comfortable interface, must be lightweight for convenience, must be easy to attach on the patient, and should be easily transportable. The practicality of the exoskeleton is greatly affected by its actuators, which are responsible for executing the motion of the robot. Since the energy provided in a pLEE is limited, the actuators must be compact, lightweight and efficient, such as to provide the required power for joint motion with minimal losses [4].

Given the significant interest in the development of exoskeletons, the demand for more powerful, safe and efficient actuators has emerged. When designing an exoskeleton to restore walking, actuators with a high power-to-weight ratio, high efficiency and compliance must be considered [4]. Also, the system should be designed in such a way to allow accurate control.

Metrics such as power-to-weight ratio and efficiency, are used to determine the performance of the actuator [5]. An actuator can be assessed using these metrics based on the system design specifications [6]. However, in a robotic system, overall system performance depends not only on the mechanical, but also in the electronics design, software and control algorithms.
Figure 1 by [6] provides a visual scheme of an actuator's performance, which presenting it in layers the layer affecting the system's overall performance.

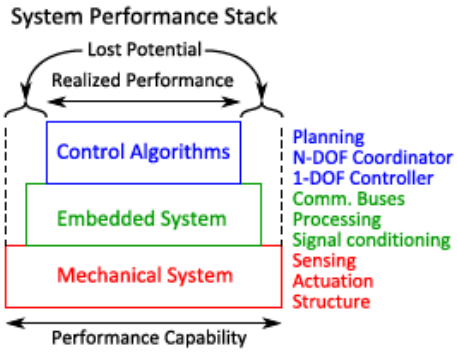

Figure 1 Actuator performance levels. This visual representation of system performance shows how each layer in a robotic system affects overall system performance [6]

Even though pLEE actuators have achieved decent performance over the last years, it seems that there are still important limitations yet to be addressed. Most pLEE actuators are too heavy and provide limited torque and power than the ones necessary for daily activities [3]. Higher power requirements also mean heavier

energy sources [3]. The torque and power output of the actuators depends highly on the mechanical design, which can be improved. The energy efficiency of the actuators can also be improved by minimizing losses. Also, there are still torque sensing issues, like accurately measuring output torque.

Therefore, the mechanical design of an actuator can be a determining factor to the performance/practicality of exoskeleton. This leads to the objective of this project, which is to attempt to increase the realized performance capability of the mechanical system by tackling some of these limitations. The embedded systems and control algorithms are a subject to be addressed in future work and is outside the scope of this project. This project confronts the limitations of the state-of-the-art pLEE actuator, by improving its mechanical design, in terms of optimizing the component configuration, reduce power consumption, minimizing mass and resolving practical design issues.

1.2 State-of-the-art robotic joints' Actuators

An actuator converts energy to mechanical force and motion. Lower extremity exoskeletons require actuators that are able to produce relatively high forces, while being light and compact. That means that usually they need high power-to-weight ratio [7]. Actuator performance is therefore very important if we want to reduce the weight while still fulfilling the joint requirements. The actuator performance can be defined by the following metrics:

Power to mass ratio (W/kg), which is the ratio of the maximum available mechanical output power, P_{out} to the mass of the actuator. This metric shows "how much power can the actuator output with respect to its mass" [8] Sometimes the term "power density" is used [9]:

$$r_{PW} = \frac{P_{out}}{M}$$

Force/Torque to mass ratio (N/kg), which is defined as the amount of force/torque that an actuator can deliver and is defined by the ratio of output torque to its mass. Also, the term "torque density" is used:

$$r_{WV} = \frac{F_{out}}{M}$$

Bandwidth. The force bandwidth shows the range of frequencies where the actuator can generate the input forces. The available bandwidth of the actuator is defined by the cut-off frequency, which is linked to the actuator's time constant. Actuators must be able to be controlled in a wide range of frequencies. These are related by the following expression:

$$f = \frac{1}{2\pi\tau}$$

Steady-state efficiency: Shows how much energy is converted to actual work. It is necessary to have a high efficiency to reduce energy losses. The efficiency, η, of an actuator is defined as the ratio of the output mechanical power,P_{out} to the input power P_{in}:

$$\eta = \frac{P_{out}}{P_{in}}$$

Other metrics that are important are:

- **Compliance:** is usually needed in exoskeleton actuators, to prevent damage from impacts and increase safety.
- **Mechanical Robustness**: the sensitivity of an actuation technology to the damaging effects of impact forces [10]
- **Torque resolution**: shows how much torque can the actuator measure in each increment.
- **Power consumption:** the system should not consume too much power, because in portable devices there is limited amount of energy available.
- **Backdrivability**: describes "whether the motion can be easily inverted" [10]. If an actuator is back-drivable, it means it allows motion in the opposite direction without locking. In pLEE, backdrivability of actuators makes it easier for the wearer to move their leg without resistance from the device.

Following, a literature survey reviewed the state-of the-art robotic actuators designed for exoskeletons and bipedal robots. There is a variety of actuators classified in different groups, according to their drivetrain, compliance and other categories. In this section, a brief overview of these actuators and mechanical attributes is presented.

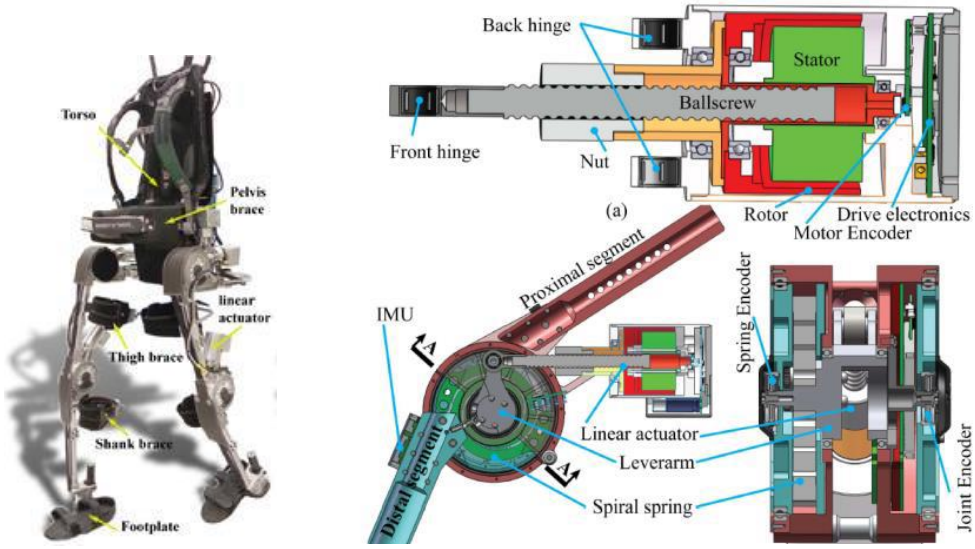

Figure 2 MINDWALKER [11] (left) MW actuator (Right) [13]

The MINDWALKER (Figure 2) is an exoskeleton developed at the Technical University of Delft and University of Twente. It has powered Hip and knee joints, which use series elastic actuators compromised of BLDC motors, ballscrew, lever arm and a spiral spring. The drives are backdrivable and the peak joint torque is 100 Nm and the motors have 960 W power [11]. The linear actuator comprises of a BLDC motor, and a ballscrew directly coupled to rotor and a torsion spring. Torque is measured by an encoder sensing the spring deflection [11]–[13]. The researchers used optimization methods to minimize weight and decrease power consumption. The joint prototype can deliver 100 Nm peak torque, with its large torque bandwidth at 100Nm is 4Hz. The joint weighs 2.9kg and has notable size, as the actuator protrudes to the side [11].

The authors of [14] designed an actuator for knee Exoskeleton to provide the torques and speeds required for sit-to-stand. A brushless dc motor of 200W drives a ball screw after an initial 2:1 timing belt. Linear guide runs parallel to the ball screw where there is four-bar linkage on the joint for increased range of motion. The link connecting to the joint is a fiberglass spring. Two encoders before and after the spring in the drivetrain measure the deflection to get torque measurements [14]. However, the fiberglass spring has variable stiffnesses at different loads, causing some control issues.

The actuator by [15] from the National University of Singapore uses two types of springs (torsional and translational) at different force ranges [15]. The actuator consists of: a lightweight (0.175 kg) servomotor Maxon BLDC motor with a rotary encoder, a torsional spring assembly with another rotary encoder, two rotary encoders measure deflection of the torsional spring, a pair of spur gears, a ball screw. Linear springs are attached to the ball screw. A linear position sensor installed in the carriage to measure the displacement of the linear spring. The two rotary encoders use differential measurements to estimate the angular deflection of the torsional spring [15].

Researchers in the University of Texas designed a Reactive Force Sensing Series Elastic Actuator RFSEA [6]. The SEA is comprised of a Maxon 200W BLDC motor, a 3:1 pulley speed reduction a timing belt, angular contact bearings, a piston style ball screw support, high compliance custom preloaded die springs, miniature ball bearing guides, and an absolute encoder. In this design (piston-style) the motor drives the ball nut instead of the ball screw, which reduced the size and weight of the UT-SEA. First, ball screw support is incorporated directly into the actuator housing using a piston-style guide. Secondly, the compliant element is placed concentrically around the piston-style ball screw support which gives series elasticity without adding to the length of the actuator.

The research by [16] provides details about the design of the electric motor actuation for BLEEX. In BLEEX they used ‘pancake’ style (relatively large diameter and small width) to minimize joint width. The motor was integrated into the mechanical structure of the joint. Harmonic drives were selected because of their large torque capacities, high gear ratios and small width [16].
Miniature rotary optical encoders are placed inside the harmonic drive to measure motor shaft angle.
To measure torque, they built a custom torque sensor placed between the torque link and the distal link. without increasing the overall joint width. To support the rotating components of the electric joint, they used angular contact bearings to provide the relative rotation between the joint’s proximal and distal links. Overall, the joint weighs an average of 4.1 kg [16].

The IHMC exoskeleton by the Florida Institute for Human and Machine Cognition robotics lab, later known as Mina (second version), is a pLEE for users who have walking gait problems. It has powered hip and knee joint. The power comes from a custom Series Elastic Actuator with a Brushless DC motor paired with a 1:100 gear ratio harmonic drive. Position and force sensors on the actuators foot switches to detect if the foot is on the ground [17], [18]. In the second version (Mina) they use a DC brushless motor and a 160:1 harmonic drive without the spring. The actuators are instrumented with two incremental encoders. Torque control was achieved with a simple proportional plus derivative controller.

CompAct-ARS is a Variable Stiffness Actuator which uses a lever arm mechanism with a variable pivot axis the location of the pivot the apparent stiffness at the output load can be reconfigured according the application [19]. CompAct-ARS is consisted by two subassemblies: the elastic module and the motor housing. The motor housing subassembly includes among others a Kollmorgen frameless brushless motor and a harmonic drive with gear ratio 100:1. The elastic module contains the compliance elements and the lever arm mechanism with the reconfigurable pivot point. The location of the pivot can be manually altered by tuning two set screws and so the apparent stiffness at the output load can be reconfigured according the application [19].

[20] designed a clutched rotary series elastic actuator with a two-modes, rigid and elastic. The SEA consists of a rigid rotary actuator using a harmonic gear and a drum brake designed to act as a clutch. The bimodal clutch was designed to switch between rigid actuation for performance and elastic actuation for human safety [20]. The motor is reduced using a timing belt with 3.33:1 speed reduction. Then, the output pulley is directly connected to the input of the harmonic gearhead, which provides a 120:1 reduction.
The output is then fed through an absolute inductive encoder and supported by a cross roller bearing. To measure the torque created by the actuator, the clutch hold, and the spring deflection, a load cell sensor was used [20]. The 200 W rotary actuator provides 54.7 Nm of torque with a maximum speed of 41.4 rpm. The measured efficiency was 0.797 due to a timing belt speed reduction that was then speed reduced with a harmonic gearhead [21].

The Exoskeleton Lower Extremity Gait System (eLEGS), is developed by Ekso bionics, to support patients with sitting-standing motions an walking [21]. Its hip and knee flexion/extension are actuated, while ankle dorsiflexion/plantarflexion is passively actuated with a spring [22]. Ekso is powered by electric actuators and battery integrated on a backpack. Ekso is suitable for user less than 100kg, and it is adjustable to fit different user heights. Walking is achieved with the assistance of crutches with maximum speed of 3.2 km/h. Battery life lasts 6 hours and its total weight is 20 kg [22].

REX is an exoskeleton by Rex Bionics Ltd of Auckland, New Zealand. It is controlled with a joystick and control pad by a network of 29 processors. The robot is always stable during walking(no crutches needed), as it has 10 DOFs, powered by 10 DC motors of 150 W power with efficiency over 90 %, (According to website) [23]. The exoskeleton allows full control of the gait cycle. The weight is 38 kg [21].

ReWalk, by Argo Medical Technologies, is a pLEE to assist patients in walking. It has DC motor actuated hip flexion/extension and knee flexion/extension and a passive ankle with a spring. [21] The device is customizable and adjustable for each patient. It has a remote-control interface placed in patients’ arm, like a watch. It incorporates a torso tilt sensor, the user can trigger step to step transition during walking [5], [24]. The total weight is around 25 kg.

Indego, formerly known as the Vanderbilt University exoskeleton, was developed to assist patients with SCI in walking. This device requires a crutch support to have balance, and has 4 DOFs in total, driven by DC motors at hip and knee [22]. Ankle and foot support are not present on the device and it has to be used with an ankle-foot orthosis. The exoskeleton approaches a modular-based design. It has two brushless DC motors through 24:1 speed reduction transmission that actuate the hip and knee joints, which achieve peak torques of 80 Nm. Additionally, the knee motors are equipped with electromechanical brakes that lock knee joints in an event of power failure. It has a lithium polymer battery with a mass of approximately 0.6kg.

Cyberdyne has commercialized the use of Hybrid Assistive Limb (HAL) for medical purposes. It has 4 actuated DOFs driven by DC servo motors with harmonic drive gears at both the side hip and knee joints while working passively at the ankles [25]. Hip and knee joints actuators are based on DC servo motors and Harmonic Drive gears, while the ankle joint is passively controlled.

1.3 Limitations of State of the Art Exoskeletons' actuators

The literature review from section 1.2 attempted to compare the state-of-the-art actuators with respect to the performance metrics, to identify possible limitations. Thus, some of their mechanical properties are summarized in Table 1. The table presents the actuated DOFs, the type of actuator, the maximum torque produced, the joint mass and the total exoskeleton mass. Other metrics such as power output and efficiency were not reported for the majority systems in the literature.

From Table 1, one can notice that the DOFs utilized to achieve walking motion are the knee and hip flexion extension, while some exoskeletons also utilize hip abduction/adduction. Regarding the actuation, some researchers prefer linear drives (Ballscrews), while others choose rotary drives. It is notable that most portable exoskeletons prefer DC motors for their power requirements. The control methods are mostly force control while some include position control or a combination of the two.

Observing the total exoskeleton weight, it is observed that most are relatively heavy, with the heaviest weighting 38 kg and the lightest being the Indego with 12 kg, which only has 4 degrees of freedom (DOFs). In this sector, it is obvious that there is room for improvement. Moreover, most portable exoskeletons provide limited torques. (Power outputs were not provided for most systems; hence not shown on the table). As a rule of thumb, it can be noticed that to produce high torques, the total mass of the exoskeletons increases. This reduces the practicality of the robot, as it becomes more difficult to transport, and adds inertia to the patient.

Since torque data and masses are available, Torque/Mass ratios (T/M) are comparable. The T/M ratios were calculated by dividing the output torque given with the given weight of their joint structure. As one may observe, the highest T/M ratio is from the UT-RFSEA actuator from North Carolina University [6]. In terms of output power to mass ratio (P/M), the UT-RFSEA reports 94W/kg, which is high for its application [6].

The torque/mass ratios for all the other actuators are in a close range between 35-48 Nm/kg.
However, one cannot say that they have reached a maximum limit as there are have been reported actuators that exceed these limits [8]. Since the actuators' performance depends on the complete joint assembly, one may attempt to increase these ratios by optimizing the design.

The conclusion is that despite the development of robotic actuators, there still are challenging problems. The review shows that size, weight and torque output currently limit portable exoskeletons. Other issues reported in the literature are backlash of gear reducer [25], achieving compliance and mechanical robustness while maintaining sufficient control and limited bandwidth range [2], [25]. Moreover, torque sensing provides several challenges, as torque is difficult to be measured directly, and thus is usually measured indirectly, but often inaccurately. Series Elastic Actuators use springs for torque sensing and compliance with environment, but the spring limits their torque bandwidth. Spring deflection is also difficult to measure, and many researchers use differential measurements by two encoders to measure it, often resulting to inaccurate measurements [17] [14]. These gaps arise the demand for more research in the field of pLEE actuators, as there is a necessity to improve the mechanical design to create more powerful, safe and efficient actuators.

Table 1 State of the Art exoskeleton/robotic actuators

Name	*Actuated DOF*	*Actuator*	*Actuator mass (kg)*	*Max torque output (Nm)*	*Torque density (Nm/Kg)*	*Exoskeleton Weight (kg)*	*Control Method*
ReWalk	HFE KFE	Electric motor	n/a	n/a	n/a	25	
Ekso GT (eLEGS)	HFE KFE	electric motors	n/a	n/a	n/a	20	Force, impedance control
Indego (Vanderbilt Exoskeleton)	HFE KFE	BL DC motor electromechanical brakes	n/a	80	n/a	12	Trajectory tracking control
Rex exo	HFE HAA KFE ADP	DC motors	n/a	n/a	n/a	38	
HAL	HFE KFE	DC motors& Harmonic Drive	n/a	n/a	n/a	15	Impedance control
MINDWALKER	HFE HAA KFE	Brushless DC motor, Linear ball-screw, torsion spring	2.9	100	34.5	29	impedance control
Mina (IHMC exoskeleton)	HFE KFE	DC motors& Harmonic Drive	n/a	80	n/a	21	position-force
TWIICE	HFE KFE	DC motors& Harmonic Drive	1.4	57	40.7	15	force control
Torque Controllable Knee	KFE	Brushless DC motor, Linear ball-screw, spring	1.8	80	44.4	n/a	force
UT-RFSEA	**N/a**	**Brushless DC motor, Linear ball-screw, spring**	**1.17**	**60**	**51.28**	**n/a**	**position-force**
BLEEX electric	HFE KFE	BL DC motor -Harmonic drive	4.1	200	48.78	n/a	force
UT Singapore SEA	n/a	BLDC motor with Ballscrew	0.85	40	47.05	n/a	Force
Clutched RSEA	n/a	BL DC motor -Harmonic drive	1.21	54.7	45.2	n/a	Force control
Compact_ARS	n/a	brushless motor and a harmonic drive	2.1	80	38.09	n/a	

**(HFE = hip flexion/extension, HAA = hip abduction/adduction, KFE = knee flexion/extension, ADP = ankle dorsi-flexion/plantar-flexion)*

1.4 Thesis Approach and Research Goal

1.4.1 Research Goal

The goal of this research is to design and fabricate an actuator which is lighter, more compact and more powerful compared to the state of the art, with ultimate purpose to use it in the new generation of more lightweight, more agile, more usable and human-friendly exoskeletons.

The research sub-questions that from the basis of this project are the following:

- How to influence the mechanical design to increase performance and decrease weight and size?
- How can we design a compliant actuator without limiting the torque bandwidth?
- How to overcome some practical problems concerning torque sensing issues?

1.4.2 Approach

The approach to resolve these questions was to examine and compare different actuation technologies, transmission technologies and design configurations, to end up in a design that can solve some of the critical design limitations.

First the requirements of the exoskeleton's joint were determined, and the actuator's components were chosen. Different concepts were analyzed, and simulations of the models were compared. Preliminary CAD models were made, identifying the design challenges, while solutions were proposed. Finally, the most optimal model is chosen for design and development.

A dynamic analysis of an exoskeleton model was made to estimate the forces acting on the actuator. Structural simulations are made to determine the resistance to failure of the components. To add compliance, a torsional spring is designed using a mass optimization approach, to meet the specifications of the actuator.

Moreover, factors which influence performance at the mechanical level were countered. These include minimizing frictions and minimizing the components' mass, while maintaining structural integrity and integrating the components into a compact design. The mechanical structure was optimized to reduce its weight and size.

Finally, this work resulted to prototype which was manufactured, and a number of tests were designed to evaluate its mechanical performance.

1.4.3 Thesis Outline

This thesis is divided in nine chapters. First an introduction has been given to the purpose of this project. In the second chapter, the design requirements for an exoskeleton joint are investigated, concluding to a list which quantifies them. In chapter three, the choices regarding the mechanical components is presented and justified based on comparisons. Moreover, different configurations are analyzed, modelled and compared in terms of design trade-offs. The chapter concludes with the choice of configuration. Chapter four describes the component selection while chapter six describes the design procedure of the actuator. Chapter six presents the experimental hardware and tests that were performed, while chapter seven presents the test results. The last two chapters include the discussion and conclusions of this project.

2 Design Requirements of Exoskeleton Joint

In this chapter, we introduce the requirements needed to design an exoskeleton joint. These include the range of motion, powered degrees of freedom, the forces acting on the joint and the sensory information needed to achieve proper control.

2.1 Range of Motion and Powered Degrees of Freedom

To design an actuator for a pLEE, the first step is to define the requirements of the robot. The critical biomechanical factors to consider in the design of an exoskeleton are the DOFs, range of motion (ROM), joint torque requirements, joint rotational velocity, and torque control bandwidth [4]. Other crucial factors concerning the type of actuation are the weight distribution/inertia of the exoskeletons, and physical interfacing with the user body.

The proposed exoskeleton has the requirements to enable paralyzed people to walk on level ground with a slow speed 0.8m/s. For the exoskeleton prototype, the actuated DOFs were chosen to be hip flexion-extension (HFE) and Knee flexion-extension (KFE). The Hip Abduction/Adduction (HAA) and ankle plantar/dorsiflexion (APD) will be passive, where springs can be used for these DOFs.
For more details about the procedure of determining the exoskeleton requirements, the reader is referred in Appendix A.

There is always a trade-off between weight and achieving a natural gait pattern. The reasoning behind this decision is the reduction of weight. According to literature, adequate gait can be reproduced by only actuating these two DOFs, and keeping the other two passive [2], [26], [27]. That means walking can be achieved, but with the support of crutches for balancing. If there is no active APD, balancing cannot be achieved otherwise [2], [26], [27].

Table 2 Exoskeleton's biomechanical requirements

#	**Exoskeleton Requirements**	***Desired Value***
1	Powered DOFs	2 per leg (Hip Flex/Extension & Knee Flex/Extension)
2	Passive DOFs	2 per leg (Hip Ab/Adduction & Ankle Plantar-Dorsi flexion)
3	Target maximum walking speed	0.8m/s
4	Exoskeleton desired weight	<12 kg
5	Range of motion – Hip Flex/Extension	110 º flexion/ 20 º extension
6	Range of motion – Knee Flex/Extension	120 º flexion/ 1.5 º extension
7	Range of motion – Hip Ab/Adduction	5º abduction/ 5º adduction
8	Range of motion – Ankle Flex/Extension	20 º dorsiflexion/ 20 º plantarflexion

Table 2 summarizes the kinematic and size requirements for the proposed exoskeleton. One can notice that the desired values considerd for the design are slightly higher than the ones in literature for safety margins. The joints can be mechanically constrained by using mechanical end stops.

2.2 Actuator Mechanical Requirements

To determine the torque and power requirements, normalized gait data was obtained from different studies [28] [29], [30].

Kinematic gait data were obtained from [31] to make a kinematic analysis of the exoskeleton. This data represents the average joint angles of humans walking with speed 0.8 Km/h, which is the desired gait motion from the exoskeleton. The angles are in the sagittal plane for the ankle, knee and hip and in the

frontal plane for Hip ab/adduction. For simplification, only the 3 DOFs of the foot, shank and thigh are taken into consideration, because these are of interest.

The angular velocities and accelerations were derived from the derivatives of the angles with respect to time. Because the data was noisy, they were filtered with a Butterworth filter with a sampling frequency of 1000Hz and cut-off frequency of 10Hz.
However, differentiating the data produces a differentiation error. Even after filtering, the velocities may not be exact to the real ones. The Error propagates even further when differentiating the velocities to get the accelerations. This error is taken into account and is expected to affect the results.

The time of a cycle is considered 2 Hz, which means a period of 2 seconds.
Data were processed in Matlab. The kinematic data are presented below.

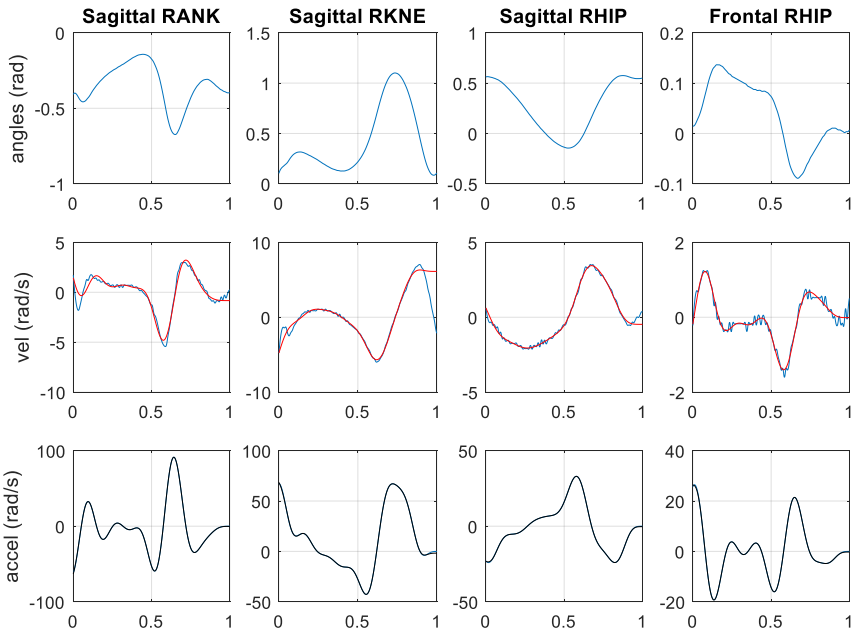

Figure 3 Anatomical position angles, velocities and accelerations and filtered data values (red,black)

The angles given are with respect to the anatomical positions (standard CGA angles) relative between each consecutive segment. Therefore, they must first be converted to the local coordinate systems of each segment (Absolute angles) as shown in figure 4.

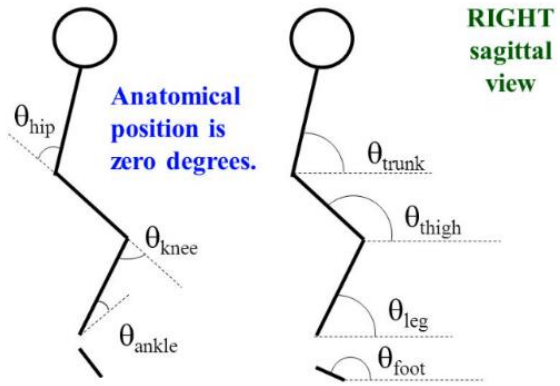

Figure 4 Anatomical and Absolute angles

From the data it was observed that θ_{trunk} during walking is always between 81-82 degrees, thus is assumed to be fixed at 81 degrees. The absolute angles are calculated as follows:

$$\theta_{thigh} = \theta_{trunk} + \theta_{hip}$$
$$\theta_{leg} = -\theta_{knee} + \theta_{thigh}$$
$$\theta_{foot} = \theta_{ankle} - \theta_{leg} + 90$$

The Equations of motion can be solved with respect to a global fixed coordinates frame.
To get the linear velocities and accelerations of the body a global fixed frame is defined.

The analysis is done only on one leg's model, which is divided into support model and swing model for simplification.
The human gait has three phases, the stance phase, double support and swing phase. The swing phase starts at about 60% of the gait cycle. Therefore, for the 0-60 percent the exoskeleton is modelled as a 3-link pendulum, while from 60-100% it is modelled as an inverted pendulum with the hip fixed, as shown in figure 5.

From 0-60% of the gait cycle, the modelled leg of the exoskeleton suit, is considered in the support model, then the foot-supporting point of exoskeleton suit is regarded as the base coordinate, while the trunk's CG is considered the End effector.
From 60-100% of the gait cycle, the modelled leg of the exoskeleton suit, is considered in the swing model, then the hip joint of the leg is regarded as the base coordinate, and the ankle of exoskeleton suit is regarded as the end effector.
This assumption however, is not true as there is mutual influence between the two legs. For example, from 50-60% of the gait cycle, there is the double support phase, which is not taken into account here. Also, in the swing phase, the hip frame (global frame) is considered fixed, while in reality it is moving. These simplifications are taken into account and expected to affect the results of the simulation.

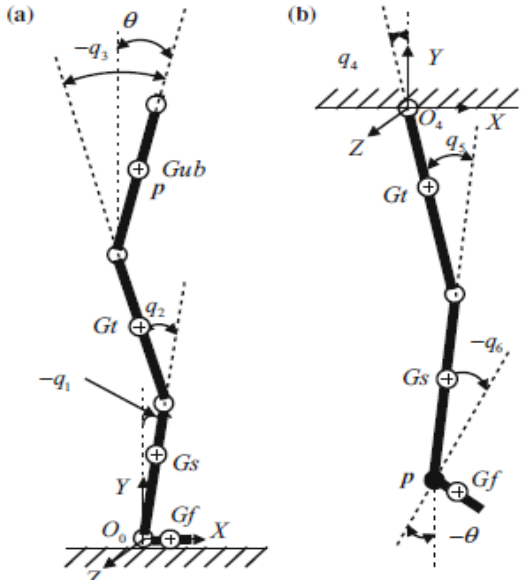

Figure 5 a) the supporting leg b) swing leg [32]

Inertial properties
Before starting the inverse dynamic analysis, the inertial properties of the links are be estimated.

The exoskeleton mass is assumed to be 11 kilograms and the human mass 111 kg. The height of the human is assumed to be 1.90 m.
The moment of inertia of the exoskeleton's links are assumed to be

$$I_z = \frac{mL^2}{12}$$

Where m the mass of each segment and L the length.

The inertial properties of the model are presents in table 3.

Table 3 Inertial Properties of each segment

	Mass [kg]	*Limb Lengths [m]*	*Mass moment of Inertias [kgm2]*			*Center of gravity*		
			Ix	**Iy**	**Iz**	**x**	**y**	**z**
Exo foot	$0.2*m_{exo}$	$0.158*L_{tot}$	$ml^2/12$	$ml^2/12$	0	-0.3*Lf	0.2*Lf	0
ExoShank	$0.5*m_{exo}$	$0.247*L_{tot}$	$ml^2/12$	$ml^2/12$	0	0	0.5*Lsh	0
Exo thigh	$0.5*m_{exo}$	$0.226*L_{tot}$	$ml^2/12$	$ml^2/12$	0	0	0.5*Lth	0
Human foot	$0.014*M_{tot}$	$0.158*L_{tot}$	0.0080	0.0073	0.0018	-0.3*Lf	0.2*Lf	0
Human Shank	$0.\ 7*M_{tot}$	$0.247*L_{tot}$	0.0600	0.0575	0.0098	0	0.5*Lsh	0
Human Thigh	$0.13*M_{tot}$	$0.226*L_{tot}$	0.5250	0.5250	0.1077	0	0.5*Lth	0
Human Trunk CG	$0.58*\ M_{tot}$	$0.407*L_{tot}$	1.5159	1.5159	0.1077	0	0.4*Ltr	0

**(Data in Table 3 were obtained from Biomechanics and Motor Control of Human Movement* [33]*)*

2.2.1 Forces Acting on the Joint

To determine the reaction forces on the joints, the inverse dynamics method is considered.
Inverse dynamics is the method used to determine the joint reaction loads by computing forces/moments (kinetics) needed to produce the recorded motions (kinematics) with inertial properties.

In this study, the Newton-Euler solution method is used, where the Newton's second law is applied, which implies that the summation of all forces and torques are equal to the bodies' inertias multiplied by their accelerations.

Modelling assumptions

The model considers the following **assumptions**

- Inertial mass and force often approximated by modelling leg as assembly of rigid body segments
- Inertial properties for each rigid body segment situated at centre of mass (CM)
- Each segment is symmetric about its principal axis
- Angular velocity and longitudinal acceleration of segment are neglected
- Frictionless, no stiffness or damping
- Center of Pressure fixed at one point
- Only two gait phases considered, the swing and single support phase, double support neglected
- external reaction forces are only ground reaction force, which is known
- No interaction forces between robot and human limbs, they are considered coupled together

Free body diagrams of the segments determined the forces acting on the links. These are forces/moments at joint articulations and forces/moments/gravitational force at CM.

The only interaction force acted on the exoskeleton limbs is assumed to be the mass of the human limbs, which is assumed to act on the center of mass of the exoskeleton limbs.

The external force is the Ground Reaction Force (GRF), which is known from measurements [32]. The unknown forces are on the joints, calculated from the dynamic equations. Knowing only the GRF, we can calculate all the way up to find the forces acting on the shank, thigh and pelvis.
The GRF is exerted on the point called Center of Pressure (CoP) on the foot link. The location CoP is changing throughout the gait cycle and affects the reaction forces. However, in this analysis it is assumed fixed, for simplification.

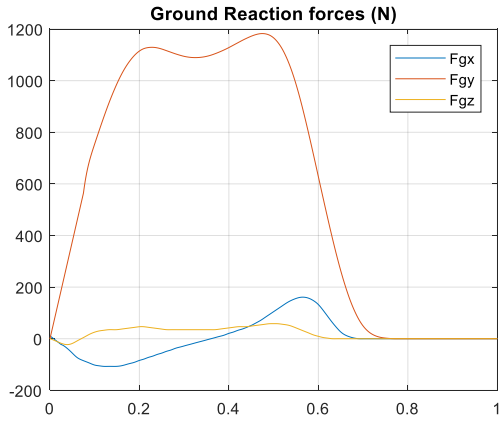

Figure 6 ground reaction forces (data from [33])

The recursive Newton-Euler approach is applied to form the equations of motion of each link:

$$\Sigma\vec{F} = \vec{F}_p + \vec{F}_d + m\vec{g} = m\vec{a}_G$$
$$\Sigma\vec{M}_G = \vec{M}_p + \vec{r}_p \times \vec{F}_p + \vec{M}_d + \vec{r}_d \times \vec{F}_d = \vec{J_G} \cdot \vec{a} + \vec{\omega} \times \vec{J_G} \cdot \vec{\omega}$$

F_p, M_p is the force and moment vectors from the proximal link
F_d, M_d is the force and moment vectors from the distal link
r_d, r_p the vectors from the Centers of Gravity (CoG) to the joints.
$J_G * a$ the inertial force
$\omega \times J_G \cdot \omega$ the gyroscopic forces from 3axes rotations

Assuming F_p, M_p are known the equations can be rewritten as

$$\vec{F}_p = m(\vec{a}_G - \vec{g}) + \vec{F}_d$$
$$\vec{M}_p = \vec{J_G} \cdot \vec{a} + \vec{\omega} \times \vec{J_G} \cdot \vec{\omega} - \vec{r}_p \times \vec{F}_p - \vec{M}_d - \vec{r}_d \times \vec{F}_d$$

Since the Inertial and kinematic quantities are known, the equations can be solved
Vector forms of the equations of motion are given as:

$$\vec{F}_p = m\left((1-c)\vec{\ddot{p}} + c\vec{\ddot{p}} - \vec{g}\right) + \vec{F}_d$$
$$\vec{M}_p = \hat{R}\hat{J}_G\hat{R}^T\vec{a} + \tilde{\omega}\hat{R}\hat{J}_G\hat{R}^T\vec{\omega} - \tilde{r}_p\vec{F}_p - \vec{M}_d - \tilde{r}_d\vec{F}_d$$

Where c center of gravity
$\ddot{p}$ is the acceleration vector of the proximal link
$\ddot{d}$ the acceleration vector of the distal link
$\bar{g} = [0\ g\ 0]^T$ the gravity vector
$\hat{C}$ the rotation matrix from the global to the link frame
$\tilde{\omega}$ the rotational velocity skew matrix (same as the cross product)
$\bar{\omega}$ the rotational velocity vector
$\tilde{r}_p, \tilde{r}_d$ the scew matrix of the vectors from the CoG to the joints

The equations of motion yield a three-element force and torque acting on the distal joint. The elements are all expressed in the global frame.

Results and discussion
The reaction forces and moments were calculated as follows. The joint reaction forces are calculated with respect to the global frame. To express them in local coordinates, they are transformed by the rotation matrices of their links.

$$\begin{matrix}{}^i_iF_i = R_i * {}^0_iF_i \\ {}^i_iM_i = R_i * {}^0_iM_i\end{matrix}$$

The local forces and moments are presented in the figure 7.
As shown in figure, the forces acting on the longitudinal axis (Fy) are the highest. They have a profile that looks like the GRF. The maximum values of the forces are around 1000-1200 N.
In this model, the exoskeleton is assumed to bear 100% of the load.
This implies that the exoskeleton joint, and thus the actuators should be able to withstand these forces and higher.
The forces in the sagittal axis Fx are around 500 N for the knee. The fact that there are forces in the axial plane means there will be a need for bearings that can take axial load.

The Torques presented are the necessary to achieve the desired motion. For the ankle the moment on the sagittal plane is up to 160 Nm, which is reasonable. The maximum torques for the hip and knee are close to the ones found in literature, around 65-75Nm. The profile is different, but this is due to the assumptions explained above.
Comparing to the literature, it was observed that these maximum values are reasonable [28], [30].
However, since many assumptions were made, the force calculation may not be very accurate. Thus, a safety factor of 1.5 is considered for the design.

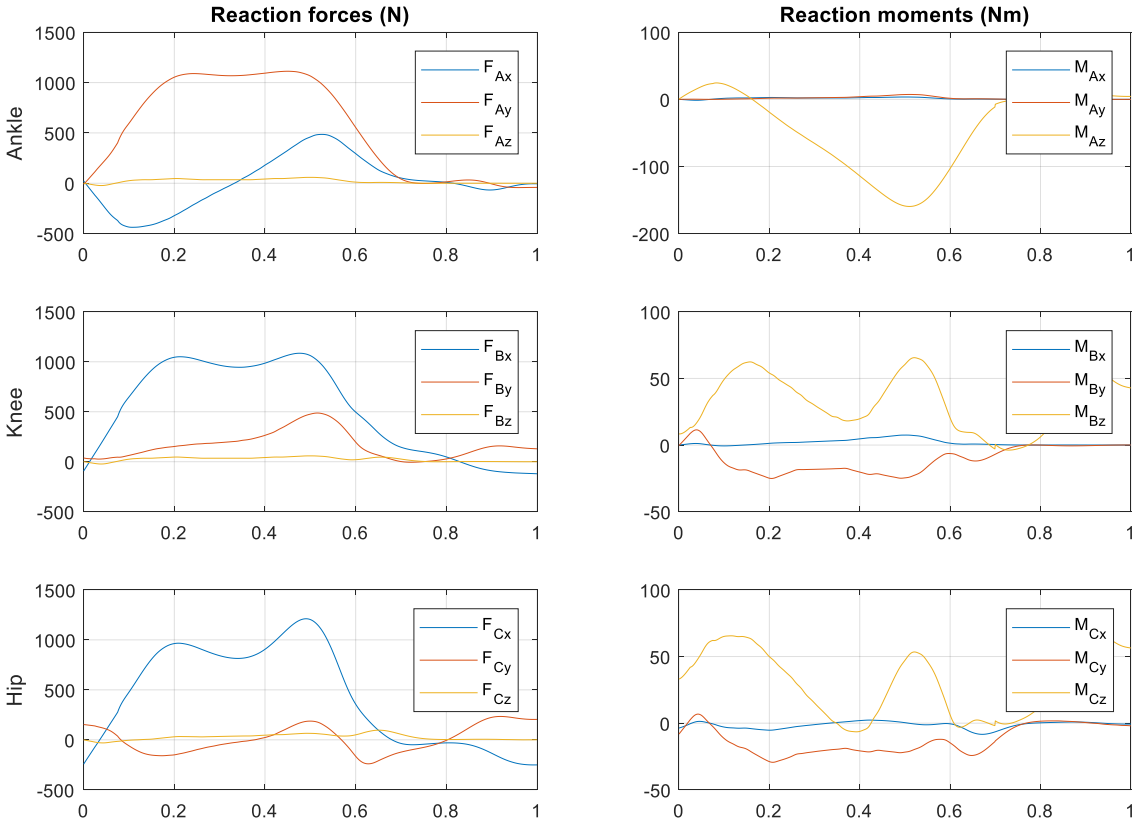

Figure 7 Reaction Forces and moments acting on joints

Figure 8 Power requirements for the joints

The power of each joint was calculated by $P = T.\omega$. The results show higher power requirements from the ones found in the literature. This however may be due to the differentiating error, the velocities are a then higher than the ones found in literature, which resulted in overestimated power.

2.3 Sensing Requirements

2.3.1 Position/Velocity Sensing Requirements:

Based on the information gathered from literature, the basic requirements for sensory information is the following: Position angles are necessary to be measured to know what the angles of the joints are at any instant. It is important for control purposes to track the trajectories of the angles, to be able to adjust the gait pattern. It is desired to measure joint angle, and motor angle. Therefore, more than one encoder is needed.

Many exoskeletons in the literature use absolute or incremental encoders for angle measurements. Mind walker uses miniature absolute rotary encoder for motor velocity and position control [11]. The UT-SEA actuator uses absolute encoder [34]. The IHMC exoskeleton actuator uses two incremental encoders [35], Sheperd et al. also used incremental encoders for their knee exoskeleton [14] and so did the TWIICE exoskeleton from [36] .

A comparison of position sensors is shown in table 4 by [60]. For the position feedback, the absolute rotational encoders have a good bandwidth, good noise to signal ratio and are easily available. As we can see they have high resolution and precision. Absolute encoders, in contrast to incremental, have the advantage to keep position when switched off, while incremental don't. Optical encoders, however are very expensive. Magnetic encoders are cost effective and have multiple mounting options. Therefore, absolute magnetic encoders are selected, as they are cheaper but still have a high resolution.

Table 4 Comparison of position sensors [37]

	Potentiometer	LVDT	Hall effect transducer	Encoder
Linearity(%)	0.2–2	0.1–0.25	1–2	0.01
Resolution(μm)	5	0.25	0.1	0.25
Cost	Low	Medium	Low	High
Life	Low	Medium	High	High
Robustness	Medium\low	Medium	Medium	High

2.3.2 Torque Sensing Requirements

Torque measurements are necessary to be able to control the amount of torque produced by the actuators. Typical load cells have the following advantages. They are very accurate, readily available and calibrated by manufacturer. However, the disadvantages are that they are quite bulky in size and have rigid construction and also are expensive.

The authors of [38] developed a novel way to measure torque on the joint of BLEEX. They connected the output of the HD gear to a third link. This small link is connected to the distal link and has a force sensor on it. The force sensor rigidly connects the torque link and distal link together. The force sensor measures the joint torque without increasing the overall joint width[38].

Another common method of force sensing is by using strain gauges. In a paper by [39], the authors created a custom type of a disk shaped load cell using strain gages. They used an aluminium disk with four cross shaped beams. They attached four strain gages on each beam to form a Wheatstone bridge and measured the torque through the strain measurements [39]. However, load cell measurements may be noisy if not placed correctly, and may be sensitive to temperature changes, or influences by forces acting on other axis.

Many researchers use elastic elements for torque sensing [12], [34], [40]–[42]. Torque is measured by sensing the spring deflection and multiplying it with the spring constant. The deformation is measured by using an encoder or a potentiometer.

Figure 9 Torque sensor using strain gauges by Zhang et al. (2018) [39].

2.3.3 Control

The design of the exoskeleton's actuators will have a strong influence on how well controlled state can be achieved. The position control scheme is commonly utilized to make sure the exoskeleton joints turn in a desired angle. Torque control is also desirable in exoskeleton, to produce the desired torques and trajectories of the joints. These are applied in the low level controllers [43]. At high level control, the interaction force between human and the exoskeleton are considered in the exoskeleton robot. It can be controlled by an impedance controller, which accepts position and produces force. Its main goal to eliminate the force of human- exoskeleton interaction [43].

Even though the controller design is beyond the scope of this project, force/torque control methods are considered for future implementation. To actually measure the performance of the actuator, we need to know how well it responds to a torque input. Eventually, to test it, we must perform experiments to push the actuator torque to the limits of its mechanical and control capability.

The low-level controller processes trajectories in joint coordinates to the necessary torque in the joints. Independent joint control is used to control the torque output based on the voltage/current input. It uses a model of the motor in the joints and does not take the manipulator dynamics into account. A commonly chosen control method for independent joint control is the PID controller [32].

Conventional technologies for force control include current control or by using load cells [40]. The variable being manipulated in practice however is current in a DC motor because it is approximately proportional to the motor torque. However, in practice, current torque with brushless motors is quite complicated.

Force control using load cells is accomplished in the following way.
The gear reduction introduces friction and increasing inertia at the output of the gearbox. To eliminate the effects of friction and inertia introduced by the gears, a torque sensor and a feedback control algorithm can be used. The torque sensor measures the force imparted on the load by the actuator. The feedback controller calculates the error between the measured force and the desired force and applies the appropriate current to the motor to correct any discrepancies. In this way a lower impedance and higher force fidelity (smoothness) can be achieved, than controlling only using the current control.

A limitation of the load cell feedback is that it can have stability issues. If there is an impact introduced in the system, the load cell will generate large signals. A high-gain feedback controller would quickly produce large torque, causing chatter. To maintain stability, the closed loop control gains must be kept very low. This can result is a slow control system that is unable to respond to small forces. Thus, the effects of friction and inertia cannot be completely masked with the closed loop control system [40].

Elastic elements can be implemented for force sensing; by measuring the compression of the compliant element, the force on the load can be calculated using Hooke's Law. Series Elasticity introduces compliance between the actuator's output and the load. Thus, closed loop control gains can be higher while there is less of chatter [40].

2.4 Conclusion

Thus, requirements for output torques and power for the actuated pLEE joints are defined in Table 5.
The conclusion is that the actuator should be capable of producing 83 Nm continuous torque at the output and 111 W. Because the demands for the HFE are close, the same actuator can be used for both joints. By

assuming the desired weight of the actuator should be around 1.5 kg, the power/mass and torque/mass ratio desired from the actuator are 74W/kg and 55Nm/kg respectively

The torque bandwidth shows the maximum frequency to which the human joints can generate the desired torques. More than 95% of the hip and knee joint torque signals are in the frequency range between 0 and 5Hz [33], thus a minimum bandwidth of 5Hz is defined as a requirement to torque control for the full torque range. A good output torque resolution is desired, which according to [13], a resolution of 1 Nm is considered sufficient for this application.

Table 5 Maximum torque, power velocity and bandwidth requirements

	Joint Max Torque output	***Joint Max Power output***	***Max Velocity***	***Torque Bandwidth***	***Torque resolution***	***Weight***
Active HFE	83 Nm	55 W	2 rad/s	>5 Hz	1 Nm	<1.5 kg
Active KFE	66 Nm	111 W	4.8 rad/s	>5 Hz	1 Nm	<1.5 kg
Passive HAA	83 Nm	33 W	0.87 rad/s			< 0.5 kg
Passive ADP	167 Nm	189 W	2.7 rad/s			< 0.5 kg

3 Design Considerations and Configuration Selection

In this chapter, all the design choices for the actuator are explained in detail. First it is explained how the fundamental actuation technology is chosen, then there is a comparison between stiff and elastic actuation, and then the transmission technologies are investigated. Furthermore, we investigate and compare the configurations in which the selected components could be assembled, as each configuration has different trade-offs. Moreover, the models of the proposed embodiments are derived and analysed by simulating the frequency responses of torque transmissibility and sensitivity. Lastly, the configurations are compared with respect to their torque sensing capability and design trade-offs and then one is chosen for development.

3.1 Actuation Technologies Review

3.1.1 Choice of Fundamental Actuation Technology

This section presents a brief overview of actuation technologies. After reviewing the actuation technologies, the design choice had to be made. A comparison is made with respect to the requirements above. The metrics compared are the P/M, T/M ratios, Efficiency and auxiliary equipment. The required P/M ratio was defined as 74 W/kg and the required T/M ratio as 55Nm/kg.

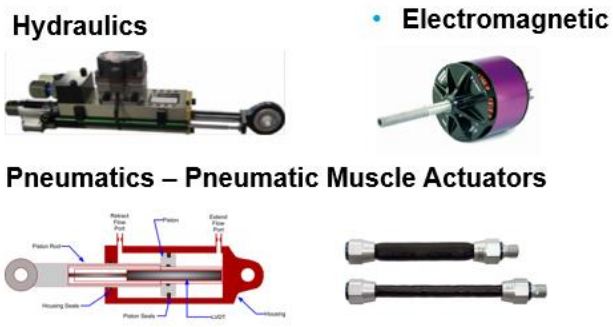

Figure 10 Different types of actuators

A comparison of actuation technologies for robotics has been made in the past by [8] which showed that hydraulics had the highest P/M and T/M ratios. However, in this comparison, the auxiliary systems were not counted. Also, technologies have changed over the last three decades, since the study was made.

In this text, only the main actuation technologies (electric motors, hydraulics and pneumatics) are compared. Other technologies were reviewed but are excluded since they are not suitable yet for use in exoskeleton applications [44], [45], [46], [47]. The comparison is shown in Table 6. The P/M ratio and T/M were taken as the ratio of the continuous power or force a given actuator with respect to the total mass of it and its auxiliary components but excluding the mass of the energy source. Efficiencies were calculated from the ratio of the power output with rated power input of actuators.

From the table, we can observe that the electric motors have highest P/M and Efficiency. But they require high speed reduction to achieve high torque. Hydraulics also are close to the requirements. They have high power and torque outputs, but due to the auxiliary components, like fluid reservoir or circulation pump, their ratios a become lower.

Regarding the P/M ratio, electric motors have the highest and then the hydraulics and pneumatics. That is because BLDC motors can achieve high rotational velocities. A significant limitation of hydraulic and pneumatic actuators is that they usually depend on pumps or air compressors to regulate the fluids. The overall mass of these auxiliary components is significant, reducing the achievable P/M and T/M ratios. The disadvantage of motors is the need of transmission to provide high torque, while fluid systems can do this directly. These transmission elements may negatively affect the backdrivability efficiency, size and mass [48]. Pneumatics can have reduced P/M ratio by utilizing pressurized gas tanks, with a pressure regulator (if necessary). Pneumatics can output high forces, and are lightweight, but need to carry a compressed air storage. Compressed Air storage tanks have less storage capacity than current li-ion

batteries (compressed air:17 Wh/L)(li-ion: 250–693 Wh/L) [49]. This is not necessary a drawback, as it depends on the required usage time.

In terms of efficiency, the electric motors also have the lead, with 80%. In the fluid systems the efficiency decreases with the number of components installed. In pneumatics, air compressibility decreases efficiency. A hydraulic system requires a battery to power a motor, which will make the pump work to circulate the fluid, and there are also losses in the pistons. The efficiency of the system is a multiplication of each component's efficiency, which concludes to a reduced total efficiency. Power consumption is also a criterion, and we can see that with motors we can modulate the power consumption. In pneumatics and hydraulics, seal friction can reduce the ability to produce small forces. Hydraulic systems generally have high impedance due to seal friction and large fluidic inertia.

Concluding, all three main actuation technologies individually have advantages and trade-offs, and all can be used in pLEE design, depending on the requirements. Hence, in the end, the actuator for the exoskeleton was chosen to be an electric motor because of their efficiency high power-to-weight ratio. The torque-mass ratio is also a significant criterion for actuator, as we need high torques and low rotational velocities. This however can be achieved with a high gear reduction.

Table 6 Comparison of different types of actuators

	Desired	***Electric motors***	***Pneumatic/PMA actuators***	***Hydraulics***
Power/Mass ratio	>74 W/kg	140 W/kg [48]	73.5 W/kg [50]	90 W/kg [48]
Torque/Mass ratio	>55 Nm/kg	3.8 Nm/kg (without transmission) [48]	30.6 Nm/kg [50]	40.8 Nm/kg [48]*
Efficiency	Highest	80% [48]	30% [48]	40% [48]
Auxiliary systems	Least	transmission needed	wiring needed	wiring needed
Auxiliary power supply	Least	Batteries	Storage tank& regulator	Compressor& accumulator

** The data in [89] was given in F/M ratio in N/kg. Here they were converted to Nm/kg by assuming an average moment arm from the actuator to the joint of 0.06m. In this table, the mass of the auxiliary parts (except the battery) is included.*

3.1.2 Choice of Elastic or Stiff Actuator

Many researchers suggest that the addition of spring in series with actuator could have several benefits [34], [51]–[53]. In fact, the most widely used actuators in robotics are Series Elastic Actuators. A Series Elastic Actuator (SEA) is a motor-powered/ hydraulic/pneumatic actuator fitted with a spring that attaches to the load. The first series elastic actuators developed at the MIT Leg Lab by Gill Pratt and Matt Williamson in 1995 [52]. They are since used in robotics to control force and increase compliance with environment [52].

Most electric motors need gear reduction to support heavy loads. Unfortunately, gears introduce friction, backlash, torque ripple, and noise. One effect of the series elasticity is to low-pass filter shock loads, thereby greatly reducing peak gear forces [40]. Series elasticity also turns the force control into position control, removing the need for force sensors. In a series elastic actuator, output force is proportional to the position difference across the series elasticity multiplied by its spring constant. Position is easier to control accurately. A spring placed between the gear train and driven load. A position sensor measures the deflection, and the force output is calculated using Hooke's law ($F = Kx$).

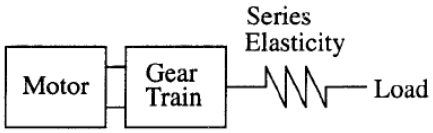

Figure 11 Simple Model Of SEA

Variable impedance actuators (VIAs) use an elastic element in series with the actuator, but with the difference that the stiffness of the spring can be adjusted. This is useful for applications where stiffness needs to be changed, like walking on inclined surface. However, most VIAs need two motors, one to position the actuator and another to change the elasticity.

Trade-offs of Elastic Actuators over stiff:
Elasticity reduces the effects of a gearbox's backlash and friction reflects less inertia back to motors decouple motor inertias from the robotic limb if the robot hits something [52]. The spring increases compliance with environment and tolerance to impact loads. Thus it has low mechanical output impedance and passive mechanical energy storage [40]. The actuators achieve back-driveability and the force transmission fidelity (or smoothness) of the gear reduction is no longer critical.

A study by [44] investigated Serial and Parallel spring in actuator design for an exoskeleton. Their results showed that at the HFE joint, the parallel spring can reduce the torque and power demand on motor and gears. At the knee (KFE), "no spring is suggested, as there are no benefits". At the hip in frontal plane and at the ankle, both SEA and PEA can achieve large power reduction, but parallel springs can reduce the torque, while series springs cannot [44].

The main advantage of SEA with respect to the stiff joint case is the increased force control robustness. Benefit of series elasticity also included, safety, shock tolerance, lower reflected inertia, and low-cost force measurement by spring displacement. To achieve these capabilities, based on the energy storage property of the spring, the spring design must be tailored to the specific task. Unfortunately when energy is stored in the spring, the safety characteristics may be dramatically reduced because the energy can be suddenly released during impact [54].

The disadvantage of the Spring is that it adds mass and complexity to the system. Generally, we try to lower complexity as much as possible. Moreover, studies showed that low stiffness limits the torque control bandwidth [52], [40].

Elastic actuators tend to have more stable force control because the spring filters out the high-frequency motion of the mechanism, acting as a low pass filter on impacts. A low frequency in the system dynamics means that we can have more time to measure the force and for the controller to react to it.

In gait motion, we have impacts at each heel strike. The impact takes place in a very short time period and thus has high frequency dynamics. The SEA is advantageous to the Rigid actuator when there are impacts involved. This impact can damage the actuators if there is no spring, as the reflected impact goes directly on the gears and motor.
Under these considerations, it was concluded that the spring is a very valuable component for the actuation concept thus will be included in this actuator design as a Torque sensor.

3.1.3 Choice of Rotary or Linear Transmission

The best performance for force-controlled actuators can be achieved with BLDC servomotor connected rigidly to a link [7]. However, servomotors are inefficient at the low rpm and the large size makes them unsuitable for wearable robotics [9]. The solution to this problem is using smaller, lighter motors combined with gear reduction, to reduce the speed and increase the torque of the motor output. The reduction allows the motor to operate in its sweet spot (high speed/low torque), while providing the low speed/high torque output characteristics desirable in the pLEE exoskeleton [40].

Electric robotic actuators can utilize categorized to linear transmission and Rotary transmission. Linear actuators have linear speed reducers that convert rotary motion of the motor to linear and then back again

to rotary by connecting to the joint through a lever arm. Rotary actuators have a rotary transmission, so they output directly to the joint. This section argues which is more suitable for our design.

Several Gears including rotary and linear drives were investigated [37]. A detailed comparison between linear and rotary drives is shown in Appendix B.

To choose the best transmission for the actuator, the requirements set were

- Torque density, which shows how much torque a gear can handle with respect to its mass
- Speed reduction ratio, which shows how much the torque can increase
- Efficiency, which represents how much power is lost in the transmission
- Backlash, a phenomenon caused by gear teeth that introduces friction
- Compactness in size, which represents how small the gear size can be

In torque density, the harmonic drive has quite high, as it is very compact. Also it has the highest reduction ratios up to 320 at single stage [37]. Screws can also achieve high ratios [11]. The ratio depends on the angle of the joint ($N = 2\pi d(\theta)/L$). In terms of efficiency, the ballscrew has the highest (95%). In single stage the planetary also has high efficiency, but low reduction ratio. In terms of backlash, the harmonic drive has negligible, because of small gear teeth and low gear module.
Even though ballscrews provide excellent transmission choice, they were dismissed due to their long size and less mounting options. The long screw makes it difficult to integrate into a dense mechanical design. Some designs based on ball screws achieved compact size [55], but the levels of compactness seen in rotary actuator design is higher and more easily achievable.

The Archimedes Drive is a promising new transmission technology developed by IM Systems [56] which is similar to a planetary gearbox, but uses hollow cylinders to transmit torque through friction instead of gear teeth. This drive can achieve high reduction ratios without lubrication. However, this technology is immature, and more tests need to be made to validate the efficiency of the drive and determine its lifespan.

In the end, the HD transmission was chosen as the most suitable for the design because a very compact design can be achieved. The harmonic drives have the highest reduction ratio, which is very important in the exoskeleton joints. Harmonic drives are preferred, since we want to implement a small motor. Gear efficiency, however, depends on reduction ratio, with higher ratios reducing the efficiency.
Moreover, the harmonic drives have several options that could be customized for almost any motor. For these reasons, harmonic drives are preferred in the exoskeleton market [4], [24], [27], [35], [36]. A decision matrix that helped made this decision is shown in table 7

Strain wave gear working principle
A strain wave gearbox (harmonic drive) provides a very high gear ratio with minimal backlash.
A harmonic drive is made up of three main parts, the circular spline, the wave generator, and the flexible flexspline. The arrangement of these components depends on the type of gearbox. It can be a cup design or silk-hat design [37]. Their advantage is that single stage ratios are possible up to 320:1, in the same space that a planetary gear can only achieve a 10:1 ratio. Also, it maintains a compact size, low weight, zero backlash, and less components. Despite the advantages, harmonic drives have moderate efficiency 60~80% and poor backdrivability.

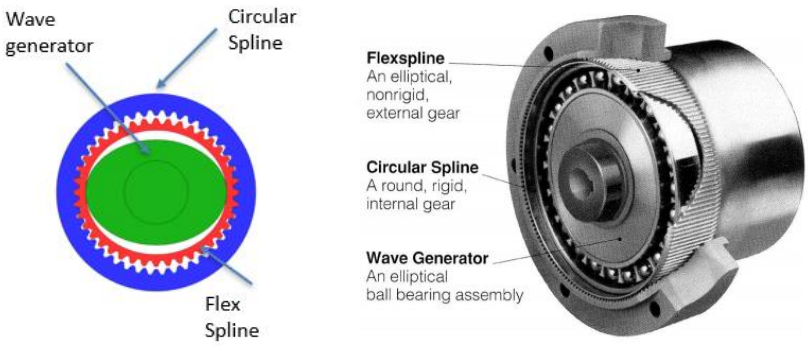

Figure 12 Harmonic gearbox (cup shaped) components [37]

Table 7 Comparison of Transmission types

	torque density	reduction ratio	efficiency	backlash	Size	total
planetary	+	+	++	+	+++	+++++++++
Harmonic drive	+++	+++	++	+++	+++	+++++++++++++
Cycloidal	++	+++	+	++	+	+++++++++
lead screw	++	++	+	+	++	++++++++
roller screw	+++	++	++	+++	++	++++++++++++
ball screw	+++	++	+++	+++	++	++++++++++++

3.1.4 Conclusion

The design choices defined in this chapter, based on the requirements, are:

- an electric motor as the torque source
- a torsional spring as a torque sensor
- rotary type of transmission
- a Harmonic Drive as the reducer

Thus, the actuator is defined as an Electric motor-powered rotary elastic actuator.

3.2 Configuration Selection of Rotary Elastic Actuator

The proposed actuator consists of a motor to generate mechanical power, a 3-component speed reducer (harmonic drive) to increase torque output, the output link (load) and a torsional spring to measure torque. These components (six in total) can be configured in many ways, producing designs with various trade-offs that affect power output, volumetric size, weight, efficiency, etc (see figure 13).

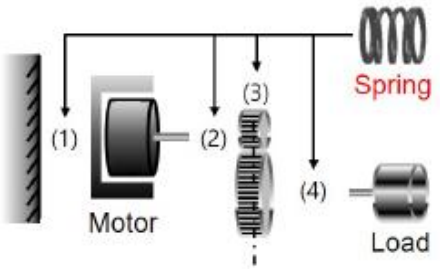

Figure 13 Possible SEA configurations emerging from the spring position [34]. (1) Spring placed between the motor and housing, (2) between motor and transmission, (3) between the gears, (4) between gear and the load.

3.2.1 Proposed SEA Configurations

Many different custom SEAs have been developed over the last decades [12], [57], [14], [52]. A study by [41] categorizes general SEAs based on the relative position of the spring with regard to the gear, and also in terms of the types of transmission and the types of motion. According to [41] there are three generic categories of SEA with respect to spring position. For our proposed actuator design, there are three main configurations, where each has two possible embodiments (total of six embodiments).

- Force-sensing Series Elastic Actuator (FSEA), is the standard SEA configuration, as proposed from Pratt and Williamson [52], which combines a motor, a reduction gear, a spring and a load in this serial order. Several SEA designs in the literature adopted this configuration [12], [57], [14], [52], because it allows the spring to directly measure the force from the load. In the FSEA design, the motor is fixed on the ground and provides torque to the Harmonic drive. The harmonic drive amplifies the torque and deforms the spring, which then generates the output torque. The spring torque can be controlled by the motor torque. The measurement of output torque can be obtained from two encoders measuring the difference of the motor angle and the joint angle multiplied by the spring constant (differential

measurement). Another way is using a separate encoder that measures spring deflection directly (direct measurement).

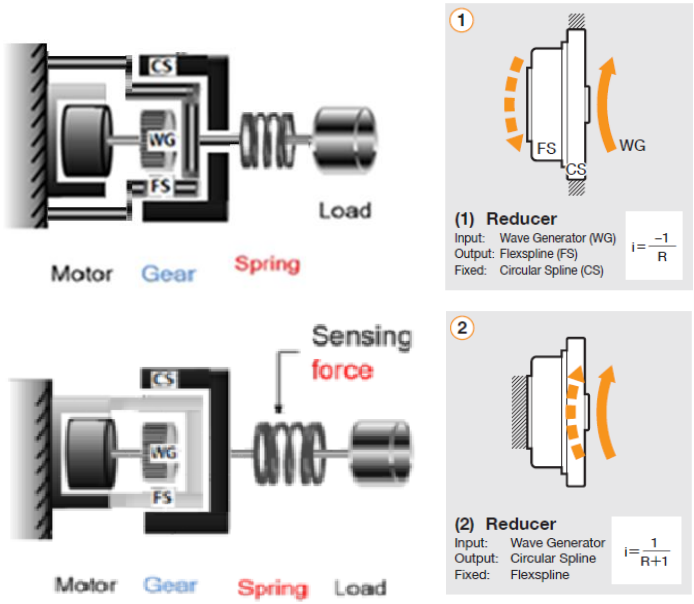

Figure 14 Force Sensing SEA embodiments which place the spring after the transmission gear CS =Circular Spline, FS = FlexSpline, WG = Wave Generator

Either of the two embodiments in figure 14 can be used for the actuator. In both embodiments, the Wave generator is the input. In the left, the spring is attached on the Circular Spline and the FlexSpline is connected to the output. In the right figure, the spring is attached on the FlexSpline, and the output is on the Circular Spline. In the right case, the FS and CS exchange roles.

- Transmitted Force-sensing Elastic Actuator (TFSEA). In TFSEA the one end of the spring is connected on the transmission and the other end is fixed on the ground and it measures the transmitted torque through the gears. This configuration employs a differential gear to achieve torque transmission to the spring. The motor delivers torque to the differential gear which is amplified and transmitted to the spring, which generates the output torque. The differential use in Compliant actuators was proposed by [58]. A hollow motor delivers the torque to the wave generator of Harmonic Drive, which if felt as transmitting torque by the spring connected between the flex spline and the ground. [59] employed a planetary gear as the differential transmission.

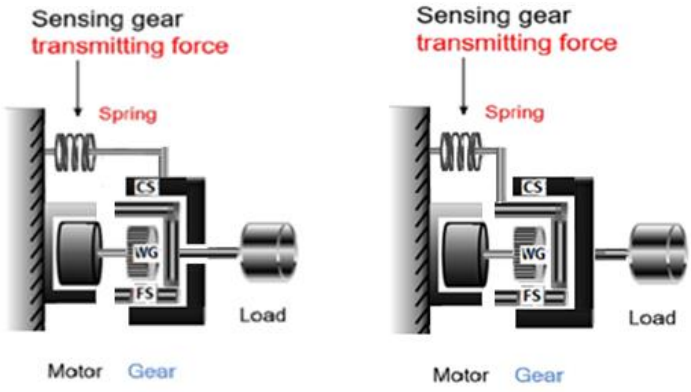

Figure 15 Possible TFSEA embodiments which place the spring inside the transmission gear

The working principle of the actuator is the following (fig 11-right):
The actuator assembly comprises of a proximal link (also may be referred as housing or ground), a motor, a harmonic drive, encoders, bearings, a torsional spring and a distal link (also referred as output link). All components are connected coaxially. The stator is fixed to the proximal link and the rotor is coupled to the WG. The FS is coupled to the torsional spring, which has the other end fixed on the ground. The output motion comes from the CS which is coupled to the distal link.

The motor transfers torque to the Wave Generator, which deforms the FS. The FS deformation causes the CS to rotate with reduced speed, rotating load. The FS is not fixed but connected to the spring. When the motor rotates, the torque transmits to the flexspline which then allows the spring to deform and measure the output torque, and then magnified towards CS.

The assembly exploits the differential function of the harmonic drive to achieve torque measurement through spring deflection. The harmonic eventually works like a differential, as it allows all three parts to rotate at different speeds. During the application of load, the Harmonic gear acts as a differential, allowing the spring to measure it.

An encoder placed on the housing measures the rotor angle of rotation. An encoder placed on the housing measures the joint angle between the proximal and distal link. A third sensor is placed between the housing and the spring, to measure accurately the spring deflection. Joint bearings allow the relative motion between proximal and distal link. Spring bearings allow the rotation of the spring coupling parts. Motor bearings allow rotor rotation.

- Reaction Force-sensing Series Elastic Actuator (RFSEA). In RFSEA the spring is located before the transmission. That is, the spring can be placed in front of the motor, or before the motor and fix to the ground. This configuration was proposed by [34] implemented in the UT-SEA. In his design the spring is placed between the ground and the motor stator. The motor generates a relative torque between the stator and the rotor, and the motor torque is amplified by the transmission and directly transferred to the load. The spring deformation is proportional to the reaction force of the motor with respect to the ground. Position sensors can be implemented in the motor and the spring. Even though the original design is a linear actuator, the principle is the same for a rotary actuator.

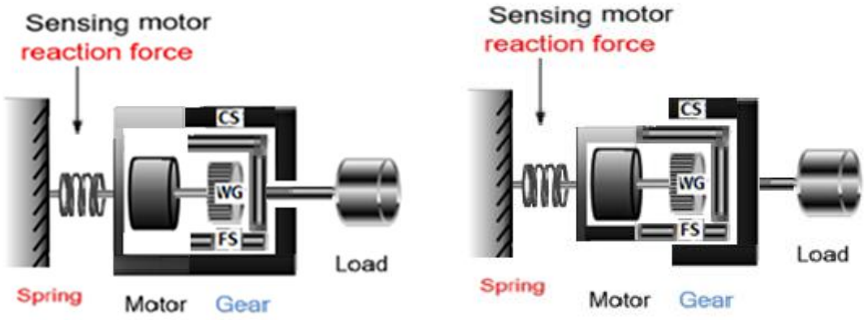

Figure 16 Possible RFSEA embodiments, which place the spring before the transmission gear [34]

The other configuration is a Reactive-Force sensing SEA (figure 16). The working principle is the same as the TFSEA above, the only difference is that in this configuration, the stator is fixed on the spring, instead of being fixed on the ground. In his design the spring is placed between the ground and the motor stator. The motor generates a relative torque between the stator and the rotor, and the motor torque is amplified by the transmission and directly transferred to the load. The spring deformation is proportional to the reaction torque. In the following sections a comparison is made to determine the trade-offs of these configurations.

3.2.1.1 Design Trade-offs

In many designs, the spring deflection is measured using the difference of the motor encoder and joint encoder [17] [14]. Thus, there is noise sourced from two encoders which reduces accuracy. In a rotary FSEA, placing an encoder to measure spring deflection is a hard task, as the readhead may be placed on the output link, which when rotating causes the twist on the cables, then a slipring or a slack of cable is necessary to avoid this. The cables of the encoder are then stationary, in contrast to a standard SEA, where they would twist. This allows accurate measurements without increasing complexity of the design by adding slipring, and also reduces potential damage on the cables.
An important advantage of the TFSEA is the sensor placement for torque measurement. In this configuration, the spring is attached between the Housing and the HD. Therefore, it allows to place a high-resolution encoder coaxially to the spring allowing accurate deflection measurement.

Moreover, the TFSEA and RFSEA embodiments proposed offer a compact actuator with reduced mass, as the components may be integrated in an optimal way, minimizing the space between them. Last but not least, the spring provides compliance, which means it can filter some shocks.

A possible disadvantage of the TFSEA would be that friction and component inertias may affect the relationship of the spring torque to the output torque. In contrast, the FSEA has no such problem, as it lies outside the harmonic drive.

The advantage of the FSEA and RFSEA is that when the output torque is acted on the load, it is felt directly by the spring, therefore it measures it directly. However, the sensor placement is proven to be difficult, as the ends of the spring are connected to the ground and stator. If the sensor is placed on the stator, this means it will rotate to a small angle, which may cause twisting the cables.

3.2.2 Modelling and Simulations of SEAs

There are several trade-offs among the configurations. The goal of modelling and simulation is to figure out their torque sensing capabilities and bandwidth limitations.

This section describes the dynamic models of rotary FSEA, RFSEA and TFSEA, using a Harmonic drive as a transmission. The dynamics of the actuator needs to be derived for the design and analysis of the controller. The Open Loop transfer functions are obtained and the Frequency responses of the three systems are compared to determine the trade-offs between them.

In the following models the CS is chosen as the output. The reason is because in the design phase, it was observed that the spring was easier to connect to the FS, thus in all models presented the CS is the output**.** From modelling prospective, it does not matter if FS or CS is the output, as the models are the same for both cases. (The only difference is for CS output the ratio is N+1, instead of N, because of the extra tooth).

3.2.2.1 Dynamic FSEA Model

The FSEA model is straightforward, as there are three components that are taken in to account. The motor-gear system, the spring and the load. In FSEA, the governing equation of each can be expressed as follows. Since the system has two masses, it is analysed as using multibody dynamics using the Newton-Euler approach. This approach is used because it allows to calculate the internal forces required to generate a desired output force, which they may reveal some trade-offs.

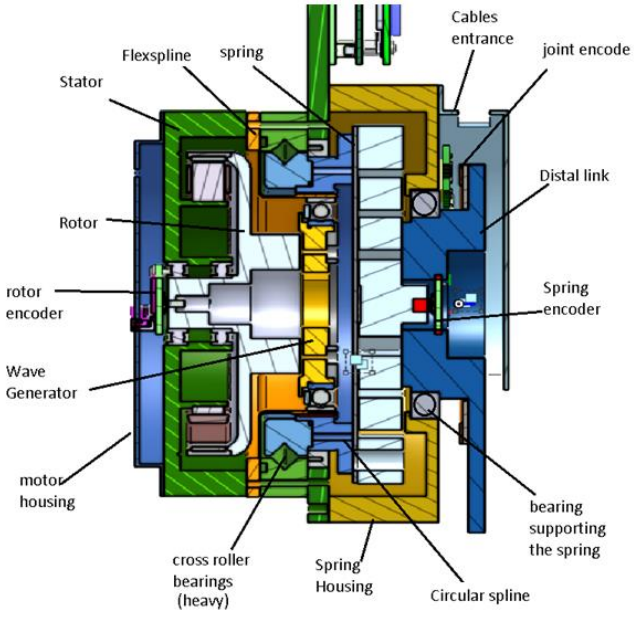

Figure 17 FSEA scheme

Coordinates
The Proximal Link (Ground) is chosen as the global fixed frame of reference. All components are coaxial thus all coordinates are expressed with respect to these. The Spring, motor and Load, the angles can be measured with encoders with respect to the fixed frame.
The free body diagrams are the following:

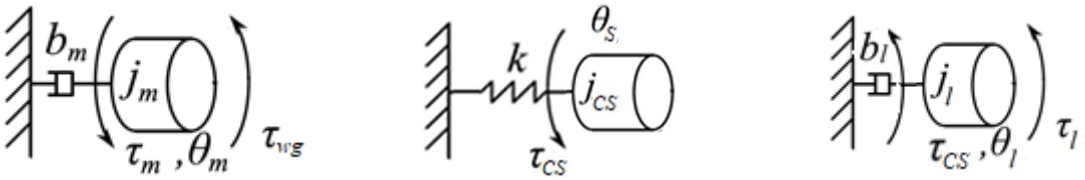

Motor-WG | CS-Spring | Load

The gear ratio of Harmonic gear unit is given as N, but since the output ratio is on the CS, the ratio is given as N+1. Thus, kinematic constraint equation is expressed as:

$$\theta_s + \theta_l = \frac{\theta_m}{N+1}$$

The Newton-Euler Equations of motion are:
On the motor side:

$$J_{rw}\ddot{\theta}_m + B_{rw}\dot{\theta}_m = \tau_m - \tau_{fs-wg} - f_m$$

FlexSpline side:

$$\tau_{fs-wg} = \tau_{cs-fs} + f_g$$

Spring equation

$$J_{cs}\ddot{\theta}_s + B_{cs}\dot{\theta}_s - \tau_s = \tau_{cs-fs} - f_g + f_{cs}$$

On the Load side:

$$J_l\ddot{\theta}_l + B_l\dot{\theta}_l + \tau_s = \tau_l - f_{cs}$$

$\tau_m = K_t i_a$ is the generated torque from the motor
$J_{rw} = J_r + J_{WG}$ the inertia of motor and Wave Generator combined,
$B_{rw} = B_r + B_{WG}$ the viscous damping of motor bearings and WG bearings,
$J_l = J_{cs} + J_{OL}$ the inertia of the spring and the Output link,
B_l the viscous damping of the joint bearings
f_{cs} non-linear friction moment caused from the joint bearings
f_m non-linear moment caused from the motor bearings
τ_{fs-wg} the reaction torque from flex-spline to wave generator
τ_{cs-fs} the reaction torque from Circular-spline to flex-spline
$\tau_s = K_s\theta_s$ the spring torque
τ_l is applied to the Load (human segment) from the actuator (or interaction torque).
$f_g$non-linear frictional moment from the gear meshing
By adding together the three EOM the internal forces cancel out, thus the output torque is expressed as:

$$\tau_l = \tau_s + \tau_m - J_l\ddot{\theta}_l - B_l\dot{\theta}_l - f_{cs}$$

3.2.2.2 Dynamic TFSEA Model

In the TFSEA model, as shown in figure 18, we can consider a lumped model, which takes in to account the following sub-systems

- Motor & WG
- Spring & FS
- CS and Load

That is because the Motor & WG move with the same angle θm, the Spring & FS rotate with angle θs and CS and Load θ_l. This simplifies the system to 3 inertias with one Constraint equation, which relates the corresponding bodies' angles with the reduction ratio. Thus, the equations describing the system are shown below.

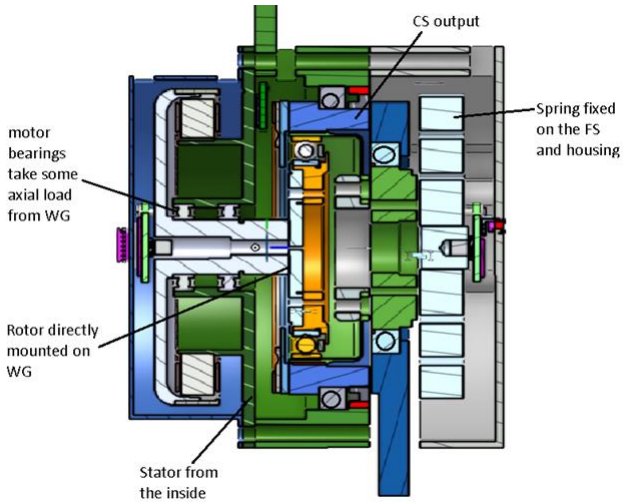

Figure 18 TFSEA scheme

Coordinates

The Proximal Link (Ground) is chosen as the global fixed frame of reference. Thus, all coordinates are expressed with respect to these. Notice that the other end of the spring is connected to the ground to which the stator of the motor is also connected. The Spring, motor and Load, the angles can be measured with encoders with respect to the fixed frame, which is an advantage of this configuration.

The Free Body Diagrams are

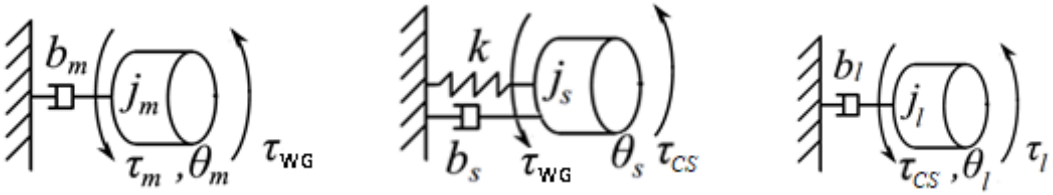

Motor-WG | Spring-FS | CS - Load

When the gear ratio of Harmonic gear unit is given as N, the kinematic constraint equation is expressed as:

$$\theta_m = (N+1)\theta_l - N\theta_s$$

The Equations of motion representing the lumped TFSEA model are:

Motor equation

$$J_{rw}\ddot{\theta}_m + B_{rw}\dot{\theta}_m = \tau_m - \tau_{fs-wg} - f_m$$

FS-Spring equation

$$J_{fs}\ddot{\theta}_s + B_{fs}\dot{\theta}_s - \tau_s = \tau_{wg-fs} - \tau_{cs-fs} - f_{cs-s} - f_g$$

Distal side equation

$$J_l\ddot{\theta}_l + B_l\dot{\theta}_l = \tau_{fs-cs} - \tau_l - f_{s-cs} + f_g - f_{cs}$$

$J_{fs} = J_{fs} + J_S$ the inertia of FS and Spring
B_{fs} the viscous damping of the Spring bearings,
$J_l = J_{cs} + J_{OL}$ the inertia of CS, output link
$\tau_s = K_s\theta_s$ the spring torque
τ_l is applied to the Load (human segment) from the actuator (or interaction torque).
$\tau_{fs-wg} = -\tau_{wg-fs}$ the reaction torques from WG to FS
$\tau_{fs-cs} = -\tau_{cs-fs}$ the reaction torques from CS to FS
f_{cs-s} the friction from the output link to the spring

By adding together the three EOM the internal forces cancel out, thus the output torque is expressed as:

$$\tau_l = \tau_s + \tau_m - J_{rw}\ddot{\theta}_m - B_{rw}\dot{\theta}_m - J_{fs}\ddot{\theta}_s - B_{fs}\dot{\theta}_s - J_l\ddot{\theta}_l - B_l\dot{\theta}_l - f_m - f_{cs}$$

3.2.2.3 Dynamic RFSEA Model

The RFSEA model is similar to the TFSEA, but the difference is that the stator is connected to the FlexSpline. The lumped model takes in to account the following sub-systems

- Rotor & WG
- Spring & FS & Stator
- CS and Load

The Motor & WG move with the same angle θm, the Spring & FS rotate with angle θs and CS and Load θload. This simplifies the system to 3 subsystems, with 2 Constraint equations, which relate the corresponding torques and the bodies' angles with the reduction ratio.

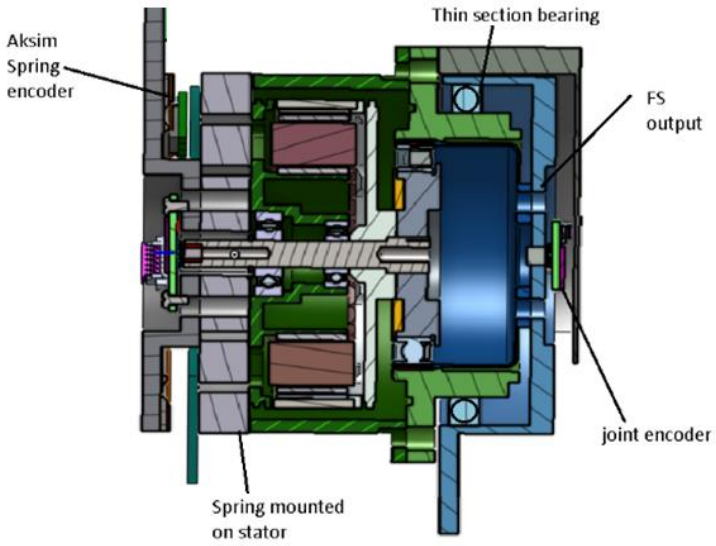

Figure 19 RFSEA scheme

Global Coordinates

The Proximal Link (Ground) is chosen as the global fixed frame of reference. All coordinates are expressed with respect to these. For the Spring and Load, the angles can be measured with encoders with respect to the fixed frame. However, the rotor encoder is placed on the stator, thus angle of the motor is measured with respect to the rotating frame of the spring.

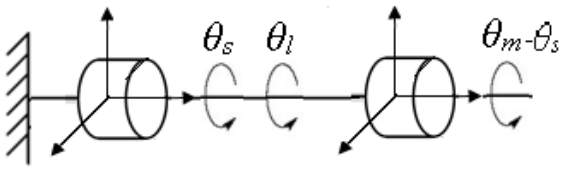

Figure 20 Coordinate systems of the RFSEA bodies

Kinematics

Therefore, the angles in the fixed frame are expressed as:

$$\theta_m^G = \theta_s + \theta_m$$
$$\theta_s^G = \theta_s$$
$$\theta_l^G = \theta_l$$

Where the θ_s^G are the angles with respect to the fixed frame and θ_s the angles measured on the encoders. Thus, kinematic constraint equation is expressed as:

$$\theta_m^G = (N+1)\theta_l - N\theta_s$$
$$\theta_m + \theta_s = (N+1)\theta_l - N\theta_s$$
$$\theta_m = (N+1)\theta_l - (N+1)\theta_s$$

And the derivatives are

$$\dot{\theta}_m = (N+1)\dot{\theta}_l - (N+1)\dot{\theta}_s$$
$$\ddot{\theta}_m = (N+1)\ddot{\theta}_l - (N+1)\ddot{\theta}_s$$

That is because the load angle also depends on the spring angle.
The Free Body Diagrams are

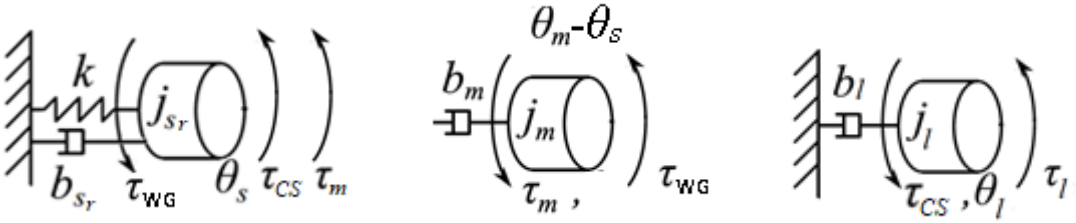

Spring-stator-FS | Rotor-WG | CS - Load

Since the system has three bodies, it is analysed as using multibody dynamics using the Newton-Euler approach. The reason we use the Newton-Euler is to analyse the reaction forces.

Equations of Motion Expressed in the Fixed frame:

$$J_{rw}(\ddot{\theta}_m + \ddot{\theta}_s) + B_{rw}(\dot{\theta}_m + \dot{\theta}_s) = \tau_m - \tau_{fs-wg} - f_m$$

Spring Equation

$$J_{fs}\ddot{\theta}_s + B_{fs}\dot{\theta}_s - \tau_s = \tau_{wg-fs} - \tau_{cs-fs} - f_{cs-s} - f_g - \tau_m$$

Load side equation

$$J_l\ddot{\theta}_l + B_l\dot{\theta}_l = \tau_{fs-cs} - \tau_l - f_{s-cs} - f_g - f_{cs}$$

By adding together the three EOM the internal forces cancel out, thus the output torque is expressed as:

$$\tau_l = \tau_s - J_{rw}(\ddot{\theta}_m + \ddot{\theta}_s) - B_{rw}(\dot{\theta}_m + \dot{\theta}_s) - J_{fs}\ddot{\theta}_s - B_{fs}\dot{\theta}_s - J_l\ddot{\theta}_l - B_l\dot{\theta}_l - f_m - f_{cs}$$

3.2.2.4 Torque Sensing Capabilities of SEAs

By rearranging the equations, we can detect the force sensing capabilities of the three configurations. The FSEA has the highest sensitivity since in the FSEA the acts directly on the load, therefore the $\tau_s = \tau_l$

Regarding the TFSEA, rearranging the spring equation from section 3.3 we notice that:
In the TFSEA the external force is transmitted through the gear, to the spring, thus the spring actually measures the Tout, plus the inertia and friction dynamics of the spring-FS system. In real application, these terms are small compared to the output torque, but may distort the spring measurement. The question is how much.

How much do these terms affect the spring measurement?
By inserting the constraint equation, the spring torque for the TFSEA is actually calculated as:

$$\theta_s = \left(\frac{(N+1)}{N}\theta_l - \frac{\theta_m}{N}\right)$$

$$\tau_l = \tau_s + \tau_m - J_{rw}\ddot{\theta}_m - B_{rw}\dot{\theta}_m - J_{fs}\left(\frac{(N+1)}{N}\ddot{\theta}_l - \frac{\ddot{\theta}_m}{N}\right) - B_{fs}\left(\frac{(N+1)}{N}\dot{\theta}_l - \frac{\dot{\theta}_m}{N}\right) - J_l\ddot{\theta}_l - B_l\dot{\theta}_l - f_m - f_{cs}$$

Rearranging we have

$$\tau_s = \tau_l - \tau_m + \left(\frac{J_{fs}(N+1)}{N} + J_l\right)\ddot{\theta}_l + \left(\frac{B_{fs}(N+1)}{N} + B_l\right)\dot{\theta}_l + \left(\frac{J_{fs}}{N} + J_{rw}\right)\ddot{\theta}_m + \left(\frac{B_{fs}}{N} + B_{rw}\right)\dot{\theta}_m + f_m + f_{cs}$$

Or by substituting

$$\tau_s = \tau_l + C1 + C2 + C3 + C4 + C5 + C6 + C7$$

Where C the terms affecting the torque measurement

$$C1 = \left(\frac{J_{fs}(N+1)}{N} + J_l\right)\ddot{\theta}_l$$
$$C2 = \left(\frac{B_{fs}(N+1)}{N} + B_l\right)\dot{\theta}_l$$
$$C3 = \left(\frac{J_{fs}}{N} + J_{rw}\right)\ddot{\theta}_m$$
$$C4 = \left(\frac{B_{fs}}{N} + B_{rw}\right)\dot{\theta}_m$$
$$C5 = f_m$$
$$C6 = f_{cs}$$
$$C7 = -\tau_m$$

To determine how much the spring measurement is affected by these terms, we would need to insert some realistic data in this equation and solve it.
The joint torque profiles T_l and output joint angle $\theta_l, \dot{\theta}_l, \ddot{\theta}_l$ profiles of the knee and hip are known from CGA data (see Appendix A).
The motor kinematics $\theta_m, \dot{\theta}_m, \ddot{\theta}_m$ the motor torque τ_m and the frictions f_m, f_{cs} are unknown terms.
Since equation has many terms unknowns, we need to make some assumptions to be able to solve it.

Estimation of unknown terms
By assuming that there is a reduction ratio of N=99, the motor angle and its derivatives can be estimated

$$\theta_m = \eta(N+1)\theta_l$$

Where η is the efficiency of the harmonic drive, since there are non-conservative forces draining energy. Since it is known that the output angle is reduced by the gear, it is a fair assumption to make, as the important thing here is to estimate its order magnitude.

Gear efficiency η incorporates losses that are difficult to model such as friction of the gears, and Structural stiffness and damping from the FlexSpline. Harmonic Drive efficiency is not a fixed value, but actually depends on many factors such as varying output torque, velocity, lubricant and temperature. According to a study by [60] the efficiency at increasing velocities, with a fixed output torque was almost constant. In our case, the torque is varying. In our case the efficiency would change in a non-linear fashion with respect to the output torque. However [60] showed that for higher torques, the efficiency is and almost constant.

Assuming a reduction ratio of 100 and a mean gear efficiency of $\bar{\eta}$ = 80% then

$$\theta_m \approx 80\theta_l$$

By using the power conservation law, the following assumption is made:

$$\eta P_{in} = P_{out}$$

Where η, the mean efficiency of the system, since there are non-conservative forces draining energy.
The power is calculated as:

$$\eta\tau_m\dot{\theta}_m = \tau_l\dot{\theta}_l$$

Therefore, input torque is estimated as:

$$\tau_m = \frac{\tau_l}{\eta(N+1)} \approx \tau_l/80$$

Friction torques estimation
The friction terms $C5$ and $C6$ have non-linear terms. These include Stribeck friction at low velocities, and Coulomb friction. An analytical friction model which calculated these terms is presented in appendix E.

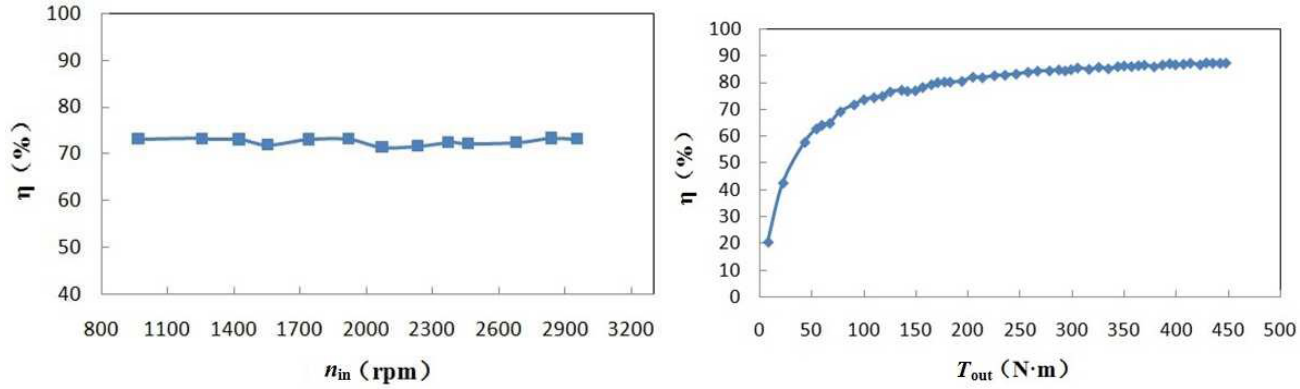

Figure 21 (left) Harmonic Efficiency vs input velocity, with fixed torque output by [60]. (right) Harmonic Efficiency vs torque output, with fixed input velocity by [60]

Simulations Results

After all the terms were estimated, the results are presented below.

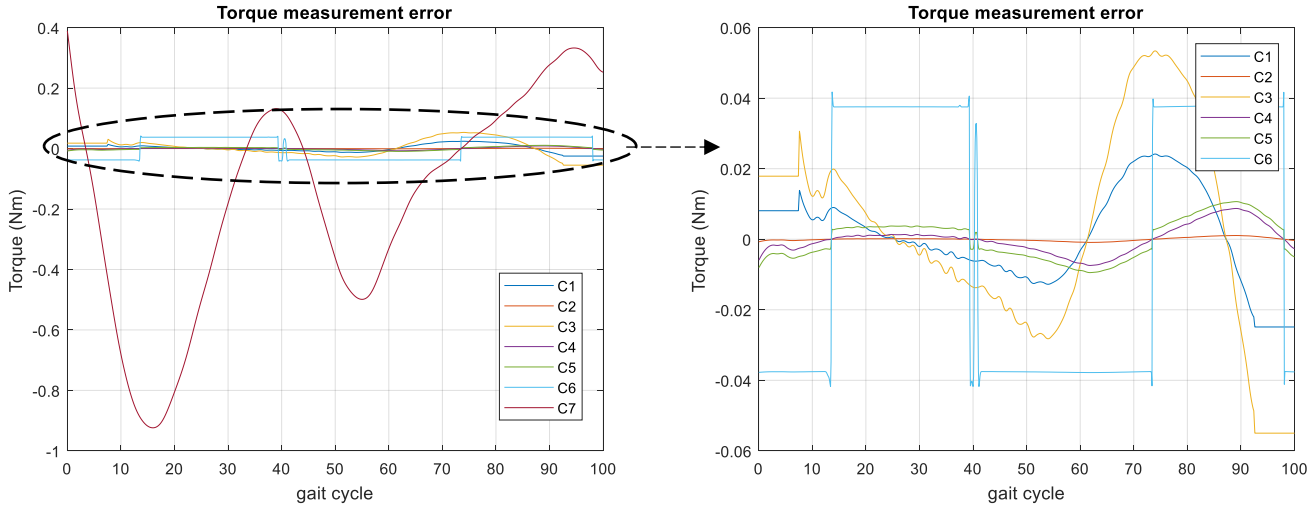

Figure 22 Parameters effecting the torque measurement of TFSEA

The right plot shows the torque caused by the frictions, inertias and damping.
The summed root mean squared error from the extra terms was estimated as

$$T_{err_{rms}} = 0.0919\ Nm$$

While the root mean squared torque for the knee joint is

$$T_{l_{rms}} = 31.51\ Nm$$

The parameters used to calculate this are shown in table 7, estimated from preliminary CAD models and obtained from literature. The summed root mean squared “error” caused by the inertias and friction terms was observed to be small (order of magnitude is 10^-1 Nm) compared to the joint torque (order of magnitude is 10^1 Nm). Thus, the terms $C2, C4, C5$ are very small compared to Ts and thus are negligible (the order of magnitude is 10^-3 Nm). The terms C1 and C3 from the inertias, are more significant, as they are magnified by the ratio to magnitudes of 10^-2 and 10^-3 Nm respectively.
The term C6 incorporates coulomb friction and Stribeck effects and, according to the model it reaches up to a magnitude of 10^-2. One can notice the rapid change when the velocity changes sign.
Since these frictions are difficult to model, identification is necessary for accurate modelling.

Nevertheless, the rms of the summed error is only 0.29% the magnitude of the rms value of the torque. Therefore, all of these terms may be neglected.

The plot on the left shows the Motor torque compared to the other terms. As observed, it is much more significant (order of 10^0), thus cannot be neglected. Thus, the spring torque for TFSEA then is calculated as:

$$\boldsymbol{\tau_s = \tau_l - \tau_m}$$

And for the FSEA & RFSEA actuators

$$\boldsymbol{\tau_s = \tau_l}$$

How to measure τ_m?
The motor torque $\boldsymbol{\tau_m = K_t i}$ can be calculated by measuring the current in the motor. The torque constant is known, and the current can be measured by the servo drive, which regulates the amount of current the motor receives. In real application, however, the motor current may have ripples which may distort the measurements, but these can be avoided with proper filtering.

Torque resolution
By ignoring the motor torque, the *maximum* error in the measurement would be 0.902 Nm. Even though it looks slightly high, it is still sufficient for our application, as the requirement set was 1 Nm. A small concern would be controlling low torques. However, if the motor torque is estimated, or measured, the torque resolution reduces to 0.125 Nm. One can suggest that the FSEA and RFSEA have inherently better torque resolution, as it is not affected by the motor torque, only by the other terms.

Discussion
As it turns out, the major frictional losses which come from the gear meshing, do not affect the TFSEA torque measurement, because they are internal forces and they cancel out. Concluding, this analysis has shown that a good approximation of the output torque can be achieved in the TFSEA configuration by using the spring measurements and the motor current. Now, to get the most accurate measurement, one could design a Kalman filter, using the model to estimate the states required to calculate these terms.

For maximum accuracy, the $\boldsymbol{\tau_l}$ can be estimated precisely using an observer or a Kalman filter, by estimating the $\ddot{\theta}_s$, $\dot{\theta}_s$. Moreover, the τ_m must be accurately known.

By neglecting the spring dynamics, we can estimate the $\boldsymbol{\tau_l}$ with some acceptable inaccuracy, therefore there is no need to estimate the $\ddot{\theta}_m$, $\dot{\theta}_m$ or $\ddot{\theta}_l$, $\dot{\theta}_l$ and even ignore the τ_m. This suggest that torque control in the TFSEA is definitely applicable by controlling the spring torque.

3.2.3 Comparison of SEA Open Loop Dynamics on Frequency Domain

After examining different configurations, the question arises; which configuration is the best for the actuator? In a paper by [41] Researchers have proposed three criteria to compare the system dynamics of different SEAs**.** These criteria presented define the ability of the SEA to generate accurate torques and respond safely to output torque.

Transmissibility
Expresses the range of frequencies the motor can transmit torque to the load [41]. It is the transfer function between the motor torque $T_m(s)$ and the output torque transmitted to the spring $T_{cs-fs}(s)$. The output is assumed fixed at $\ddot{\theta}_l, \dot{\theta}_l = 0$ or when J_l approaches infinity ($\tau_l = \infty$). Then the transfer function describing transmissibility is:

$$T(s) = \frac{T_{cs-fs}(s)}{T_m(s)}$$

Torque sensitivity
Shows the amount of deformation that occurs on the spring with respect to the load torque. In this application, the control of the load torque is desired. It shows up to which frequency the Spring can sense output torques.

$$S_o(s) = \frac{\Theta_s(s)}{T_l(s)}$$

Impedance
The transfer function between the motion of the output shaft θ_l and the load torque T_l is called the impedance (also can be defined as the torque/velocity T_l/ω_l). SEA is considered to present better safety than rigid actuators because it has lower impedance, meaning allows compliant motion when receiving output torque. Therefore, the mechanical impedance of SEA is expected to be small

$$Z(s) = \frac{T_l(s)}{\Theta_l(s)}$$

Impedance can be used to determine the stability of a system when coming in contact with the environment if Z(s) has no poles in the right half plane and the imaginary part of Z(jω) is negative for all frequencies [61].

The SEAs transfer functions were derived from the linearized ideal SEA models, which are shown in the Appendix D and are given in table 8. Note that the transmissibility and external torque sensitivity have the same denominator, which means they have the same poles.

Model Parameters
The parameters of the models were estimated in the following way:
The motor and spring inertias were estimated from preliminary CAD models.
The load inertia was assumed calculated using a mass and length as $ml^2/3$ [33]. The assumption is that the output link is a rod of length L and mass m, rotating about the joint.
Values from viscous frictions were obtained from sources [41] about the modelling of the Harmonic Drives friction [62].
The reduction ratio was selected according to requirements from section 2.2.
These parameters can be later readjusted using system identification and parameter estimation techniques.

Assumptions
- The lumped SEA models (shown in Appendix D) considers only linear viscous friction ($\tau_{fr} = B_i\dot{\theta}_i$). In the actual system, the frictions between the gears and seals, which include coulomb friction and Stribeck effects are non-linear, thus are neglected in this simulation. By assuming that the f_m and f_{cs} are very small, then these terms can be neglected. The linearized models are shown in the Appendix D.
- The flexspline is treated as rigid in the rotating direction (the Torsional stiffness is much higher high compared to the spring's stiffness [60]).
- In the model the motor torque is considered to be known, ($\tau_m = k_\tau i$). However, in some cases the motor current is noisy and the motor constant kT is changing depending on the internal resistance, which changes with the heat.

Frequency domain
From the Laplace transforms of the Equations of Motion, the three free-body dynamics of TFSEA can be expressed in the frequency domain as:

$$P_m(s) = \frac{1}{J_{rw}s^2 + B_{rw}s}$$

Expressing the motor system dynamics

$$P_s(s) = \frac{1}{J_{fs}s^2 + B_{fs}s + K}$$

Expressing the spring dynamics

$$P_l(s) = \frac{1}{J_l s^2 + B_l s}$$

For the CS dynamics, which contains the end-link

Table 8 Parameters obtained from the CAD models and literature:

DESCRIPTION	PARAMETER	VALUE
STATOR INERTIA	Jst	**0.00010536 kgm^2**
ROTOR INERTIA	Jr	0.00003070 kgm^2
WG INERIA	Jwg	0.00001290 kgm^2
SPRING ADAPTOR INERTA	Jsa	**0.00010368 kgm^2**
FS INERTIA	Jfs	0.00001791 **kgm^2**
OUTPUT LINK INERTIA	Jl	**0.0015 kgm^2**
ROTOR-WG DAMPING	Brw	0.000029 Nms/rad
SPRING-FS DAMPING	Bsf	**0.0002 Nms/rad**
LOAD-CS DAMPING	Bl	0.0001 Nms/rad
SPRING RATING	Ks	**2000 Nm/rad**
REDUCTION RATIO	N	**100**

Table 9 SEA Transfer Functions

		FSEA	TFSEA	RFSEA
TRANSMISSIBILITY $T(s)$	$\frac{T_{cs}(s)}{T_m(s)}$	$\frac{P_m(s)}{(N+1)D(s)}$	$\frac{(N+1)P_m(s)}{D(s)}$	$\frac{(N+1)(P_m(s)-NP_s(s))}{D(s)}$
EXTERNAL TORQUE SENSITIVITY $S_E(s)$	$\frac{\Theta_s(s)}{T_l(s)}$	$\frac{P_l(s)P_s(s)}{(N+1)D(s)}$	$\frac{N(N+1)P_l(s)P_s(s)}{D(s)}$	$\frac{N(N+1)P_l(s)P_s(s)}{D(s)}$
IMPEDANCE $Z(s)$	$\frac{T_l(s)}{\Theta_l(s)}$	$\frac{D(s)}{P_l(s)(P_m(s)N^{-2}+P_s)}$	$\frac{D(s)}{P_l(s)(P_m(s)+P_s(N)^2)}$	$\frac{D(s)}{P_l(s)(P_m(s)+P_s(N)^2)}$
DENOMINATOR D(S)		$(P_l(s)+(N+1)^{-2}P_m(s)+P_s(s))$	$N^2P_s(s)+(N+1)^2P_l(s)+P_m$	$N^2P_s(s)+(N+1)^2P_l(s)+P_m$

* *Details about the SEA models and their transfer functions can be found in Appendix C.*

3.2.3.1 Simulation Results

The results of the FRF simulations are presented below:

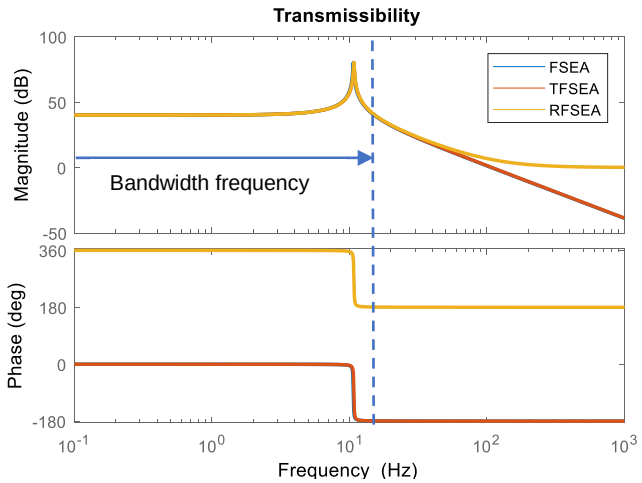

Figure 23 Transmissibility FRF

Figure 23 shows the FRF of the Transmissibility of the three actuators. In this plot the Load Inertia is set to Infinity (the actuator is fixed). The three configurations show no differences at the low frequencies, as all have the same magnitude. The DC gain is 40 dB (=100, same as the gear ratio).
At a frequency of 11Hz, we can observe resonance happening, which means that the torque output is greatly increased. This means the transmissibility bandwidth is limited up to slightly above this frequency

(17Hz), where the magnitude drops 3dB below the initial magnitude. Any input above this frequency will attenuate by the system dynamics, and thus will not be seen in the output.

This frequency is because the characteristic polynomial has a root at $\omega_r = \sqrt{\frac{K}{N^2 J_{rw} + J_s}}$ which equals to 69 rad (11 Hz). Therefore, one can see how the resonant frequency depends on the motor-WG inertia magnified by the reduction ratio, the spring inertia and the spring stiffness.

Above the bandwidth frequency the magnitude of the FSEA and TFSEA drops, which means the input torque cannot be transmitted to the output anymore as the input is attenuated by the system dynamics. A magnitude smaller than 0 dB indicates that the motor torque is greater than transmitted torque. On the other hand, the RFSEA is able to produce high frequency torques without an increased burden to the motor force. However, after resonance, the RFSEA is unstable, as we can see in the phase plot. This can be observed also from the plot in figure 24, where the spring deflection attenuates above the resonant frequency.

The essence of the transmissibility plot is that it shows similar bandwidth to all three configurations at low frequencies. The behaviour at higher frequencies is not of our interest as the actuator will receive input at low frequencies.

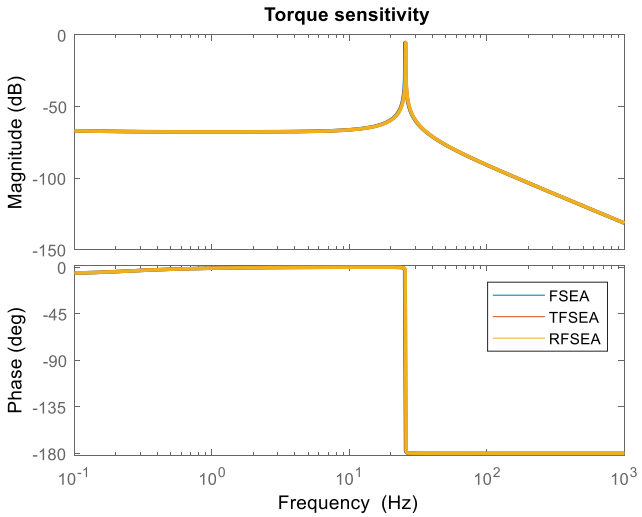

Figure 24 Torque sensitivity FRF

This figure shows the FRF of the spring Sensitivity of the spring sensing the torque acting on the load side. We can notice that all three configurations have similar behaviour across the frequency spectrum.

The sensitivity range stops at a frequency where resonance occurs. All three actuators have almost the same resonance frequency. The resonance frequency depends on the load, the motor inertia, gear ratio and the spring stiffness $\omega_r = \sqrt{\frac{K(J_l + (N+1)^2 J_{rw})}{N^2 J_{rw} J_l + (N+1)^2 J_{rw} J_s + J_l J_s}}$. In this case the load inertia is finite that is why the resonance occurs at different frequency.

At resonance, the magnitude of the spring angle becomes very high. That means for even very low torques, the spring will have high deformations, thus the sensor will give very high readings, which will provide faulty feedback. Therefore, the input torque frequencies must be kept under the resonant frequency.
Above the resonant frequency, the magnitude drops, which means the spring deflection is too small, therefore torque control is not possible.

In this graph, the higher magnitude means larger spring deformation. Therefore, one can notice that for a high spring constant the spring deformation is lower, thus the magnitude is low. For the low frequencies both actuators have the same magnitude (around -66 dB which means around a gain of 1/2000), where k=2000 Nm/rad. This means for example that for 1Nm input torque, the spring is deformed by 1/2000 radians. Nevertheless, this plot shows that the sensitivity bandwidth of the spring is sufficient and does not limit the transmissibility bandwidth

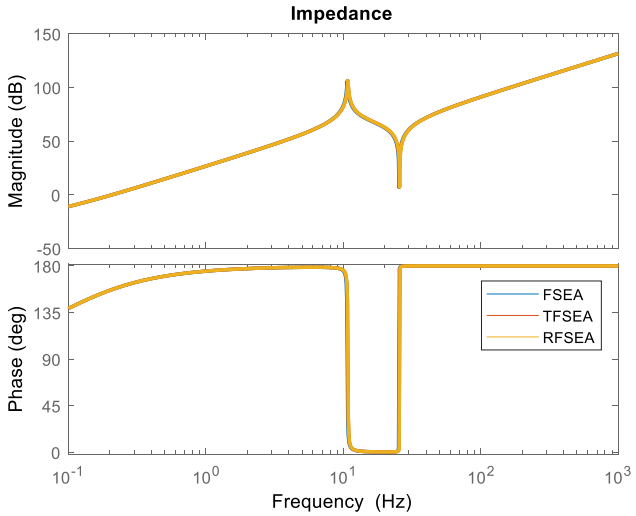

Figure 25 Outout Impedance FRF

The last figure shows the SEAs mechanical impedance. As shown in figure 25, the Impedance of all three actuators is the similar across the frequency spectrum. As observed, the Impedance increases as the frequency increase. Impedance depends on the gear ratio, thus higher gear ratio results to higher impedance. At certain frequencies, there are Resonant and anti-resonant characteristics appearing. These phenomena are determined by the spring constant and load inertia. In this simulation there is finite load inertia.

The resonance frequency of 11Hz in the impedance function represents that the SEA becomes stiff at that frequency and the motion of the distal-link is impeded. On the other hand, at the antiresonance (25 Hz), the motions of the distal-link become very high, as the SEAs behave more compliant. This can cause instability. The same frequency was shown to cause instability in figure 24, where the angle of the spring becomes very high.

Effects of Spring Constant K_s

A parametric analysis of the SEA was made, to examine how the system's behaviour changes by varying different parameters. The analysis is shown in Appendix F. Here only the effects of the spring's stiffness are presented, as they are the most important results. The FRFs examined are torque transmissibility, torque sensitivity and impedance.

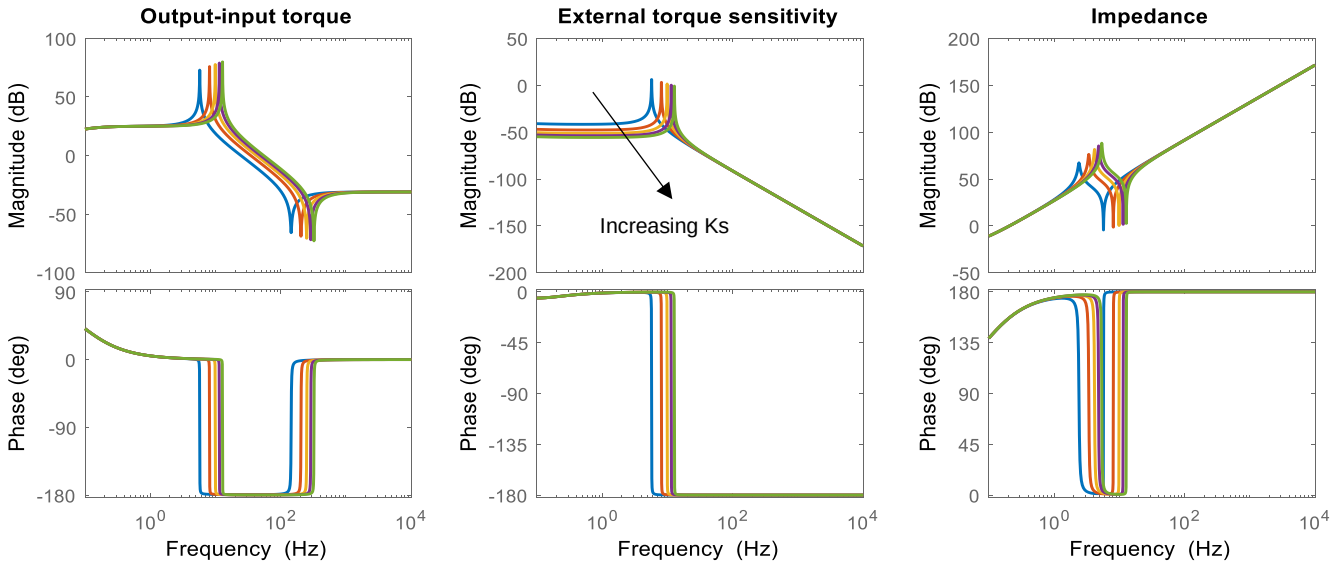

Figure 26 Effects of varying Spring constant

It is well known that spring with high stiffness allows for higher bandwidth of torque control [52]. Thus, the effect of stiffness on the open loop frequency response were examined. By plotting the FRF with varying spring stiffness, we can observe how the system behaves at different stiffness.
It is noticeable that increasing the Stiffness, increases the range of Transmissibility and Sensitivity bandwidths. That means we can measure and transmit torques at higher frequencies.
Moreover, the motion becomes impeded at higher frequency.
These observations conclude that, to increase the performance a high stiffness is needed.

However, the spring constant is a trade-off between SEAs. As seen in the sensitivity plot, the torque sensitivity magnitude becomes lower with a higher spring constant, the magnitude decreases, which means the spring deformation becomes smaller with respect to external force.
For using a stiffer spring, we can measure at higher frequencies, but it also means that a high-resolution encoder might be needed to measure this deflection. The conclusion is that higher stiffness is better, as it increases all ranges, but a high-resolution encoder is needed.

3.2.4 Conclusions

The configurations show no significant differences in transmissibility or sensitivity or impedance at low frequencies and minor differences above. The conclusion is that they are equally good in terms of performance in the frequency domain.
An advantage of the FSEA is that it may be superior in terms of force sensing accuracy. The issue of the RFSEA and TFSEA is that the spring deflection is not exactly proportional to the output torque, and there are other dynamic components in the spring dynamics such as Js and Bs. These designs need models of sprung mass and viscous damping and should be able to calculate both θ’ and θ’’ for accurate force sensing. However, it has been shown that these terms are negligible in our application.

Pros and Cons of SEAs from design prospective:
The general conclusion is that any of the three configurations can be used in this application, the decision depends on the designer. From a design prospective, in the RFSEA and TFSEA configurations offer more versatility in the design, as the spring is not confined next to the output but may be placed in different positions. An RFSEA has the disadvantage that the motor stator moves when a torque is produced.

Due to the configurations’ structural differences, a practical challenge in the actuator design is determining the placement, attachment, and type of the encoder to measure the deformation of the spring. The encoder needs to be placed on the housing, while having its sensor (magnet) on the spring.

Placing a spring encoder in the conventional FSEA is challenging, because the spring has no end connected to the housing. Thus, the spring deflection encoder readhead is difficult to place on the housing and may be placed on the output link. As consequence the cables may rotate or twist and thus slip rings may be necessary. The only option was to place the readhead on the distal link, but doing so, a slipring would be necessary, as the distal link rotates with respect to the housing (proximal link), thus the encoder readhead also rotates. Usually spring deflection is measured using the difference of the angle motor encoder and joint. This noise from two encoders and it is not so accurate due to the kinematic error of the harmonic drive.

The TFSEA offer a solution to sensor placement issues, in a simple design because the spring encoder readhead is attached to the proximal link, eliminating the need for slip rings. It is much easier to place the sensors, as there will be no twist in the cables.

In the RFSEA, a minor disadvantage is that the rotor encoder readhead can only be placed on the stator. Since the spring is the only part fixed on the housing, the motor “floats”, thus as the spring rotates the motor wires also rotate. This angle, however is small, so a slack of wire length solves the issue.

A disadvantage of the TFSEA’s measured torque is affected by the motor torque, which sometimes can be noisy due to current ripples. This however can be solved by estimating the current.

Based on the aforementioned observations, FSEA is acknowledged as better suited for force control, but has the practical spring encoder issue. Also, FSEA acts as a mechanical low-pass filter between the output and the gearbox, making them more tolerant to impact forces. The RFSEA is less tolerant to impact forces as the spring is in the back.

The RFSEA even though it's good torque transmissibility and torque sensing, it was proven to be more challenging to design. After creating preliminary CAD designs, it was observed that the FSEA and TFSEA configurations offer less design effort, while the RFSEA proved to be more challenging. The reason is because the spring's bearings placement was challenging, as it would result in an increase in the width.

On the other hand, TFSEA offers similar bandwidths while resolving the sensor placement issues and the design is achievable with reasonably low design effort. These reasons further justify the choice of the TFSEA for the exoskeleton actuator. A decision table comparing the configurations is shown in table 10.

Summarizing, the advantages of TFSEA with respect to the other SEA is:

- It has sufficient torque sensing capability
- Similar transmissibility and sensitivity bandwidths as other SEAs
- It allows the spring encoder to be placed in a strategic position, allowing for excellent cable management
- The design is feasible with reasonable design effort
- More compact and simpler design

Disadvantages:

- More control effort than RFSEA and FSEA, since motor torque affects the torque measurement

The conclusion is that TFSEA configuration offers similar performance and control options to FSEA, but can offer some design advantages, like placing the spring sensor without sliprings. Figure 27 shows a proposed CAD model to realise the TFSEA configuration.

Table 10 Comparison of the three configurations

	Force Sensing accuracy	Transmissibility & Sensitivity	Mechanical Impedance	Sensor placement Advantages	Design Effort	Compactness	Total
FSEA	+++	++	++	+	+++	++	++++++++++++++
TFSEA	+	++	++	+++	+++	+++	++++++++++++++++
RFSEA	++	++	++	++	++	++	++++++++++++

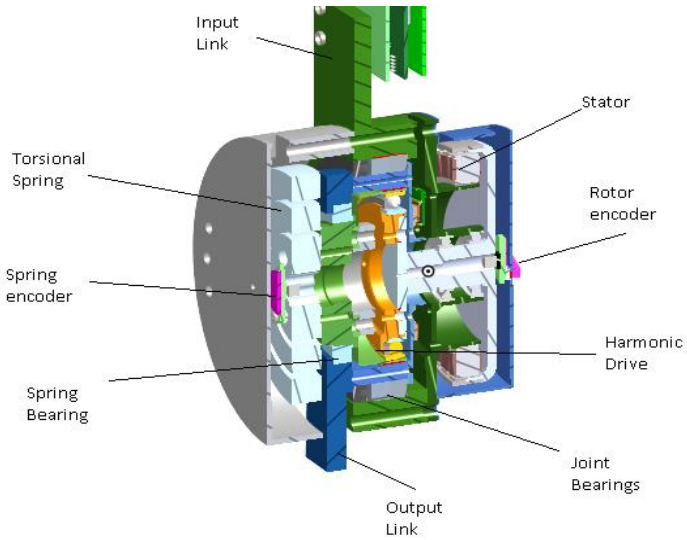

Figure 27 Proposed TFSEA design

4 Component Selections

This chapter covers the selection process of the mechanical elements. Here we analyse and compare different components based on the knowledge gathered from the previous chapters. The components defined in chapter 2 based on the requirements, were an electric motor, a Harmonic Drive transmission, a torsional spring as a torque sensor, two position encoders to measure motor and joint position.
The motor torque and power requirements are identified. The requirements in chapter 2 are used to choose the harmonic drive and the position encoders. The simulation in chapter 3 provided some insight about the stiffness needed for the torsion spring, whilst here the complete design procedure of the spring is described.

4.1 Motor Requirements

In this simulation, the motor dynamics are considered to determine the motor Torque and Power required for the motor selection. The model will determine the motor torque required for the motor, in order to select the motor with the best performance that meets these requirements.
The motor torque as shown in part 3.3 was estimated as:

$$\tau_m = \frac{1}{\bar{\eta}\,(N+1)}\tau_l \quad , \quad if\ P_R \geq 0$$

$$\tau_m = \frac{\bar{\eta}}{(N+1)}\tau_l \quad , \quad if\ P_R < 0$$

$N+1$ is the reduction ratio of the gear
Where $\bar{\eta}$ is the gear's efficiency, which here was considered 60% (conservative estimate). This way the motor is overdesigned to ensure to match the requirements.

To solve the equation, τ_l is replaced from the torques and rotational velocities profiles required to execute gait motion. The torque and velocity profiles of the Knee joint and Hip joint were obtained from Clinical Gait Analysis Data by [28]. These plots can be found in Appendix A.
Thus, the Motor torque profile is shown in figure 28.

As seen, the maximum torque requirements are 1.0 Nm and around 0.5 continuous torque (average) for the knee. For the hip the required torque is almost 1.4 Nm. Therefore, the maximum torque requirement for the motor is 1.4 Nm.

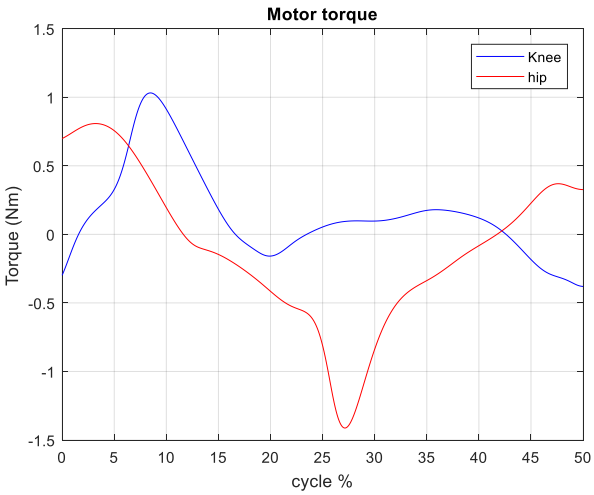

Figure 28 Motor torque requirements fir the hip and knee

Motor Power
Similar procedure is followed to calculate the motor power.
The motor power is defined as the motor torque multiplied to the rotational velocity of the joint. Also, the power losses due to frictions must be taken into account. These can be estimated by using the Motor constant Km. The power is calculated as:

$$P_m = \bar{\eta}\,\tau_l\dot{\theta}_l + \frac{\tau_m^2}{\bar{\eta}K_m^2} \quad , \quad if\ P_R \geq 0$$

$$P_m = \frac{\tau_l}{\bar{\eta}}\dot{\theta}_l + \frac{\tau_m^2\bar{\eta}}{K_m^2} \quad , \quad if\ P_R < 0$$

The results for the required motor power for the knee and the hip are shown in figure 29. It can be seen that the peak power requirement is almost 100W for the knee.

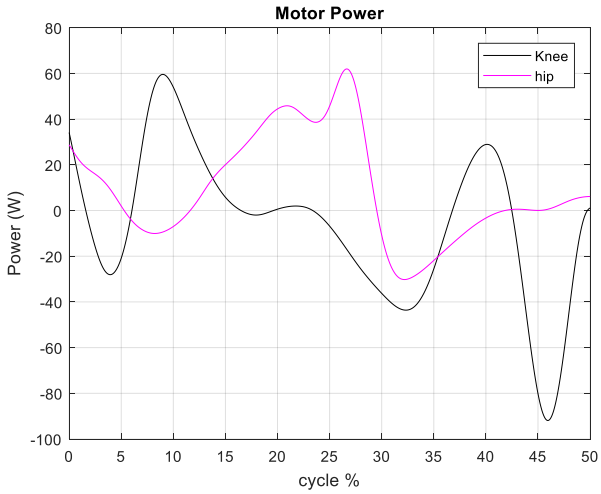

Figure 29 Motor power requirements fir the hip and knee

4.1.1 Motor Selection

Motor and gear selection are very important design choice for the actuator. The torque and speed were critical in the design to ensure that at a given speed reduction, it would produce enough torque. Weight also had to be accounted.

Brushless DC (BLDC) motors were considered as the best choice for this application. They have a rotor with permanent magnets and a stator with windings. The only moving part is the rotor, which contains the magnets. There are no brushes and commutator and the windings are connected to the control electronics. Compared to brushed motors, BLDC motors are more efficient 85~90%, more reliable, require less maintenance, they have high speeds, more current usage and produce higher torque. Brushless DC motors have higher power-to-weight ratio [37].

Figure 30 Commercial BLDC motor

However, the BLDC motor requires electronic control. For precise position/speed control most BLDC motors usually use Hall Effect Sensors [37]. There are two types of Brushless DC motors, inrunners and outrunners. The permanent magnets of inrunner brushless motors are positioned on the inside of the electromagnets while for the outrunner the magnets are on the outside. Outrunners can achieved relatively higher efficiency than inrunners because they have more winding turns, therefore higher torque density.

The objective was to find the smallest motor that can successfully provide the motor torques given by the previous equation. The desired maximum torque for motor was over 1.4 Nm.

The motor constant Km was used to compare the relative efficiencies and output power of different motors, as Km defines the ability of the motor to transform electrical power to mechanical power.

$$K_m = \frac{K_t}{\sqrt{R_m}} = \frac{T_m}{\sqrt{P_{loss}}}$$

Thus, the lower the motor's resistance the higher the K_m will be, which means we can achieve higher torque with less power losses. Then the K_m is divided by weight such as to be able to consider the weight also. Then the metric becomes Motor constant per weight $\frac{K_m}{m}$ ratio. Measuring this ratio, we consider both the motor's efficiency and weight.

Motors from different suppliers, such as Maxon, Moog, Emoteq and model airplane motor suppliers such as Dualsky, E-flite, and Hacker, and drone motor suppliers like T-Motor and Sunnysky are selected according to the torque and power requirements

Commercial all-in-one units were investigated. An example of options investigated were preassembled motor and gearhead options like the FHA-C Rotary Actuator from Harmonic Drive, with a brushless motor with a 100:1 planetary gear reduction. These were heavy, the lightest was 2.5 kg, which meant design would be difficult to include.

Thus, the criteria for choosing the motor are the following:

- Max torque between >1.4 Nm
- Motor constant as high as possible
- Weight as low as possible
- Max power >100 W

Several motors were compared, of which some are summarized in the table 11. From the table 11 we can see that the best option are the drone motors Sunnysky M8 Pro and T-motor P60. They have the highest motor constant/weight ratio. These are also very lightweight motors. They have good motor constants and they can produce high torques. Finally, a Sunnysky M8 was chosen as it is lighter and flatter and has many customizable options.

Table 11 BLDC motors comparison

Motor Type	*Max torque (Nm)*	*Power (W)*	*Torque Const Kt (Nm/A)*	*Resistance*	*Motor Const*	*Weight (kg)*	*Motor Constant/Weight (Nm/√(W)kg)*
Moog DB-2180-A-1S	1.62	274	0.0932	0.974	0.098	0.227	0.433
Hacker Q80-13S 28 pole	**3.19**	**3000**	**0.0546**	**0.029**	**0.321**	**0.610**	**0.526**
T-MOTOR P60 KV170 48V	**2.45**	**1800**	**0.0720**	**0.080**	**0.255**	**0.380**	**0.670**
Dualsky XM6360EA-12	3.53	3022	0.0519	0.034	0.281	0.617	0.456
E-lite Power 160 BL	2.34	2700	0.0390	0.030	0.225	0.652	0.345
M8 Pro KV170	**2.30**	**875**	**0.0562**	**0.079**	**0.200**	**0.230**	**0.869**
M8 Pro KV200 25V	2.86	1000	0.0477	0.055	0.203	0.247	0.823

4.2 Harmonic Drive Selection

The gear was thoroughly explored to ensure that the best possible torque to weight ratio was achieved. The harmonic gears have several options that could be customized for almost any motor. **A Transmission selection was also made for ballscrew selection as an alternative transmission for the actuator. This can be found in appendix.*

Harmonic drives are very lightweight transmissions with a wide range of available torques that can be purchased. To reduce weight further, component sets can be purchased which are just the bare components needed to operate the harmonic gearhead. This saves weight while at the same time allowing for custom housing and bearing configurations. However, implementing these sets successfully requires high precision and careful alignment.

Harmonic drive requirements
For the harmonic drive, the desired reduction ratios around 80:1 to 120:1, since the motor is quite powerful, and the weight. The focus was on customized gears so that custom servo motor can be easily integrated into the design. The inertias can be compared also.

- Reduction ratio 80-120
- Max Repeated output torque >100Nm
- High Max Momentary torque >130 Nm
- Max speed >6000 rpm
- Weight <0.5 kg

The strain wave gearboxes are summarized in the table below
In the end, the Leaderdrive LCSG-20-80 was chosen for their light weight and low cost. Also, it can be purchased in components and has customizable mounting options. The ratio chosen was 80 which gives output torques 130 Nm which are sufficient. The lower ratio was chosen to reduce the output inertia.

Lubrication
Harmonic Drive products achieve the specified ratings and characteristics in the standard ambient temperature range (0° C to 40° C) when they are used with the lubricants named in the catalogue.

Harmonic grease SK-1A was chosen as it features good durability and efficiency. Grease lubrication must have proper sealing.

Table 12 List of Harmonic Drives

	Name	*HD Type*	*reducti on ratio*	*Max input speed*	*Repeated peak torque(Nm)*	*Max momentary torque (Nm)*	*Weight (kg)*	*Torque/Weight (Nm/kg)*	*Backlash arc/min*
Harmonic Drive	CSG-20-120-2UH-LW	Cup	120	6500	113	191.00	0.640	176.563	1.5
Harmonic Drive:	CSG-25-80-2A-GR	Cup	80	6500	178	242.00	0.420	423.810	1.5
HD AG	CPL -25 - 2A	Silk hat	80	7500	137	255	0.240	570.833	10
HD AG	CPL -25- 2A	Silk hat	100	7500	157	284	0.240	654.167	10
Leaderdrive	LCSG - 20 - 160 - C -II	Cup	160	6000	113	182	0.280	403.571	10
Leaderdrive	**LCSG - 20 - 100 - C -I**	**Cup**	**100**	**6000**	**102**	**182**	**0.320**	**318.750**	**10**

Efficiency
Typical HD efficiency also depends on temperature and rotating speed. As shown in figure 31, by assuming that the temperature of the actuator will be at about 25-35 C, the efficiency ranges between 60-80%.

The efficiency depends on the conditions shown below. Efficiency depends on gear ratio, input speed, load torque, temperature, quantity of lubricant and type of lubricant. The efficiency provided by the manufacturer varies with load torque and is shown in figure 31.

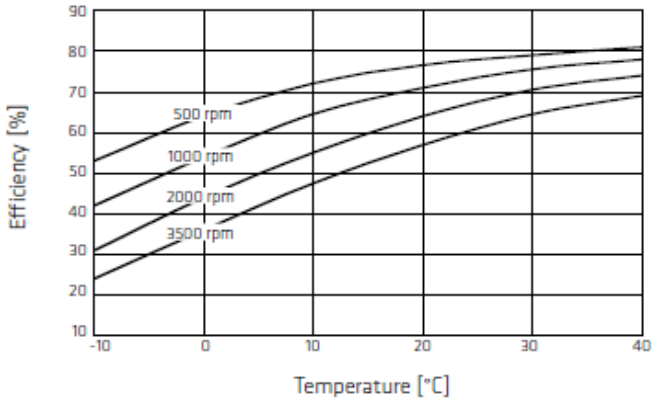

Figure 31 Typical Harmonic Drive efficiency at different temperatures and speeds[63]

Axial Forces

When a Harmonic Drive Gear is used as a speed reducer (torque input via Wave Generator), the deflection of the Flexspline leads to an axial force acting on the Wave Generator. This axial force acts in the direction of the Flexspline diaphragm. The Wave Generator thus needs to be fixed on the input shaft in the axial direction. In closed Harmonic Drive Units and gearboxes, the axial force is absorbed internally.

WG axial force approximation [63]:

$$F_{th} = 2 * \frac{T_{out}}{D} * 0.07 * \tan(20) + F_b, \quad (for\ ratio\ 100\ and\ above)$$

F_{th} the thrust force
T_{out} output torque
D HD Size x 0.00254
F_b thrust by bearing from the harmonic drive catalogue
For the LCSG size 20, T=100, ratio 100, $F_b = 9.8$

$$F_{th} = 90\ N$$

Torsional Stiffness

Torsional stiffness is provided by the manufacture of the harmonic drive gear. The typical stiffness curve is non-linear and is known to present hysteresis behaviour [63]. The stiffness is determined by the slope of this curve. For simplicity, the curve is approximated by 3 straight lines having stiffness of K1, K2, and K3. Stiffness K1 applies for output torque of 0 to T1, K2 for output torque between T1 and T2. And K3 applies for output torque greater than T2.

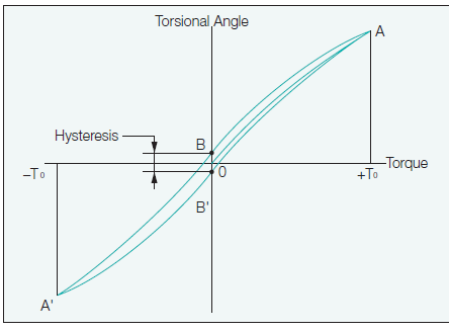

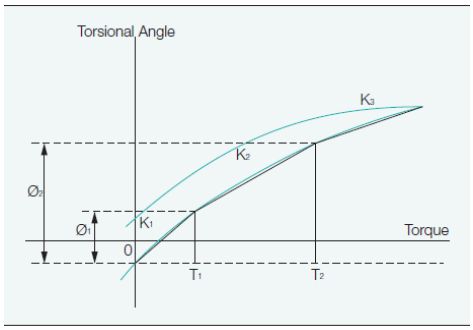

Size		20
T_1	Nm	7.0
K_1	X10⁴ Nm/rad	1.3
$Ø_1$	X10⁻⁴ rad	5.4
	arc min	1.8
T_2	Nm	25
K_2	X10⁴ Nm/rad	1.7
$Ø_2$	X10⁻⁴ rad	15
	arc min	5.0
K_3	X10⁴ Nm/rad	2.5

Figure 32 Torsional stiffness values of harmonic drive [63]

4.3 Torque Sensor

Load cells were investigated for use as torque sensors. Commercial of the shelf torque sensors are very accurate, readily available and calibrated by manufacturer. However, the disadvantages are that they are quite bulky in size, heavy and have rigid construction. Stiff load cells do not satisfy our design requirement

of compliance. Moreover, commercial load cell would increase the output impedance of joint. Thus, it was decided to develop a spring which can achieve both goals.

For torque sensing, a torsion spring is chosen to take the measurements. [12] SEA is subject to limitations in the force control bandwidth due to the drop-in force transfer performance beyond certain frequencies due to the use of spring. In order to overcome this problem, a spring with a high stiffness was considered, which requires a high-resolution encoder, resulting in a trade-off from a design point of view.

To select the torsional spring, different previous designs were examined. In the SEA of Mindwalker [11] the spring was having a double-spiral disc shape and is made of titanium. It weighs 220g, has medium stiffness of 820 Nm/rad and allows 100 Nm bidirectional torque loading. It exhibits 99.99 percent linearity in terms of load vs. deflection. Thus, it was decided to design a spring with a similar spiral design, while still focusing on reducing the weight. The spring design as a torque sensor is discussed in chapter 5.

4.4 Position Encoders

There were multiple sensor options to investigate in terms of absolute positioning. Several magnetic rotary encoders from different manufacturers were considered, of which some are shown in the table below. Absolute magnetic encoders offer high resolutions and are cheaper than optical.

Table 13 magnetic encoders

	Name	*diameter (m)*	*Resolution (bits)*	*Weight (kg)*	*Accuracy (arcsec)*
Netzer	DS-25	0.025	17	0.004	90
RLS	**AKSIM MRA7**	**0.049**	**16**	**0.077**	**180**
Avago	AEAT-6012-A06	0.023	12	0.023	317
Zettlex	INC - 37	0.037	17	0.025	2.47
ic Haus	**iC-MU**	**0.029**	**16**	**0.010**	**5**
Renishaw	RESA	0.052	23	0.100	5.5

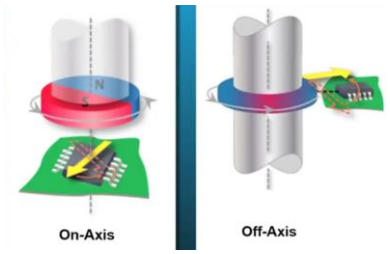

Figure 33 on and off axis magnetic encoders

As we can see all sensors have good resolution. For the motor encoder, high resolution is necessary, as it rotates in high rpm. IC Huis has small PCB options, and it offers on-axis and off-axis options. Therefore, IC Huis absolute, on-axis magnetic encoder was selected as a rotor encoder.

For the joint angle, the encoder choice is different, as during design, it was necessary to be off-axis. Also, a hollow ring is needed for this application. For the joint, the encoder chosen was the Aksim MRA8 rotary encoder, as it has very small width, and has a ring option that matches the joint's diameter dimension. Moreover, a custom readhead board was purchased.
The spring angle was decided to be measured with a separate third encoder. The differential measurement of the input-output encoders is prone to kinematic transmission error of the harmonic drive [62].
For the spring deflection, a high-resolution encoder is needed. Thus, a 16-bit IC Huis on-axis magnetic encoder was selected to measure spring deformation. The resolution is estimated as $2^{16}/2\pi$ increments/rad. Thus, the torque resolution is estimated as $K * \frac{2\pi}{2^{16}} = 0{,}1917\ Nm$

4.5 Sealing

Sealing is very important for keeping the oil or grease from spilling. The Harmonic drive chosen is recommended to be used with grease, therefore standard seals were examined. Radial oil lip seals generally offer excellent sealing, prevent spills, reduce risk of corrosion of the metal components and protect from contamination. However, they introduce friction due to contact with the rotating parts.
Grease seals can prevent grease spills, but are less efficient than oil seals, thus cannot seal oil. They have smaller width and lower friction. Thus, grease seals were considered as the best option.

Table 14 Dynamic Seals

	ID-OD	WIDTH	NUMBER		
PARKER ROTARY SEALS	76.2-88.9	6.35	19126 H1L7	SS	NBR
	76.2-85.75	2.7686	17302 ALLL7	H	NBR
TRELLEBORG TRG000770	**77-85.5**	**4.8**	**TRG000770**		
	70-85	**7**	**TRA000700**		

Static Seals:
The static seals are used to prevent the lubricant from passing through the parts where the parts are mated. They are fixed in place, thus are called static. The seals used in these applications are O-rings.
The O-Rings are double-acting elastomeric sealing elements, which squeeze in between parts acting as in a radial or axial direction. They are cheap and effective sealing options and have a large variety of sizes.
Loctite was also used for sealing the mated parts and the screws.
The O-rings chosen are shown in the table below

Table 15 Static Seals

STATIC SEALS			
	ID-OD	**Width**	**number**
TRELLEBORG	**63-66**	**1.5**	OR1506300
	74-76	**1**	OR1007400
	52-55	1.5	OR1505200

4.6 Bearings Selection

Bearing selection is crucial in mechanical design as they do not only allow the relative rotation between the rotating parts, but also bear the loads acting on the joint.
For this design, three sets of bearings were considered:

- motor bearings, which support the rotor
- Joint Bearings, which allow the output Link to rotate
- Bearing(s) supporting the spring

The selection of each bearing was regarding the loads acting on it.
Bearings are manufactured to take radial loads, thrust loads and tilting moment loads, or a combination of the three. The loads calculated in Chapter 5 are used in this section for bearing selection.
A detailed selection procedure is explained below.

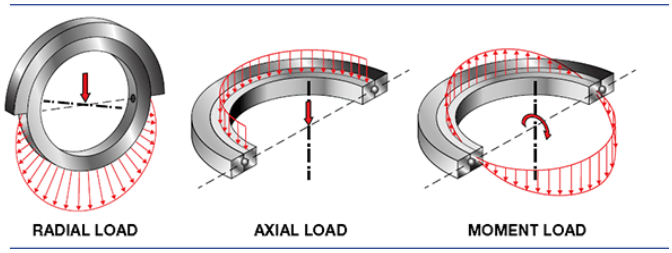

Figure 34 Different types of bearing loading

The permissible dynamic and static radial load is given from the manufacturer. However, the axial and moment load have to be calculated.
Allowable axial load according to SKF catalogue:

$$C_{thr} = 0.25C_0$$

Allowable tilting moment load according to SKF

$$M_{tilt} = 0.23 * d_1 * (\frac{C_0}{S_0} - F_{ax})$$

Safety Factor calculation:

$$n_{sf} = max\left(\frac{C_0}{F_{rad}}, \frac{C_{thr}}{F_{ax}}, \frac{M_{tilt}}{M}\right)$$

Where F_{rad}, F_{ax} and M_{tilt} are the radial, axial forces and tilting moment acted on the component

4.6.1 Motor Bearings

The motor bearings do not bear any significant load in the radial direction, but they do bear a small axial force created from the Harmonic drive, discussed in section 6.2. That is because the rotor is directly connected to the Wave Generator.

Two SKF 61802-2RZ are used on the rotor. They are sealed, thus can protect from the grease of the Harmonic drive entering inside the motor components. It is better not to mix the lubricants, thus there is a need for sealed bearings. Moreover, even though they are radial bearings, they are able to withstand the axial load. The Safety Factor $n_{sf} = 2$ which means they can withstand twice the predicted load. Furthermore, there are two bearings, which means the rotor is safe from failure.

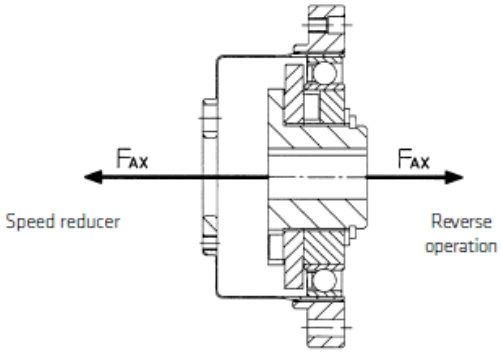

Figure 35 Axial forces produced by the Harmonic drive

Table 16 motor bearings

				RADIAL		THRUST (AXIAL)		
BEARING	Bearing number	**Bore -Outer diameter(mm)**	**Width (mm)**	**Static (N)**	**Dynamic (N)**	**Static (N)**	**Dynamic (N)**	**weight (kg)**
CRTICAL LOADS					**0**	**100**		
BUILT IN U8	61802-2Z	15-24	5	800	1560	200	390	0.0074
SKF (SEALED)	**61803-2RZ**	**17-26**	**5**	**930**	**1680**	**232.5**	**420**	**0.0082**

4.6.2 Joint Bearings

In the case of the joint, the bearing selection was a bit more complex. Also, as shown from the force analysis, there are redial, axial loads and tilt moment acting on the joint, which need to be compensated on the bearings.

Table 17 Forces acting on Actuator (referring to Ch 5)

	F_{AX}	F_{RAD}	M_{TILT}
KNEE	500	1200	25
HIP	200	800	60

The forces acting on the joints were calculated in Chapter 2.
The types of bearings that can withstand a combination of these loads are the following:

- *Radial Contact bearings*

Radial contact bearings can withstand a small amount of axial and moment load.

- *Angular Contact bearings*

Due to angular contact of the wall, it has high load carrying capacity gives excellent performance, especially in high speed application able to withstand also small axial forces

- *Cross-Roller Bearings*

Cross-Roller bearings can support moment loads, radial forces and tilting moments and are commonly used in closed harmonic drive units

- *Tapered Rollers*

For heavy loads and low speeds Taper Roller Bearings are well suited for taking axial and radial loads.

The requirements for the bearings were the following:

- Able to withstand the combined load
- Small width. A large width would increase the total width of the joint and increase the weight
- Low weight
- Diameter larger than the Harmonic drive's diameter
- Sealed. Sealing is important to separate the bearings lubricant from the gear's lubricant

The issue with the cross-roller bearings were heavy and wide. For high speeds and better accuracy Angular Contact Ball Bearings are well suited. Thin Section bearings were suited with the best dimensions and low weight, while strong enough to withstand the forces. The only problem was that, angular contact ball bearings are not sealed, which could cause problems in the design. Also, they were not easily available. Therefore, the next option was to use Thin section radial contact bearings, as they are sealed, can still provide the radial and axial support and weigh much less. The RBC bearings GA025CP0 *RBC were considered the best option.

Table 18 Joint bearings options

				RADIAL		THRUST (AXIAL)		TILTING	MOMENT	
BEARING	Bearing number	**Bore -Outer diameter(mm)**	**Width (mm)**	**Static (N)**	**Dynamic (N)**	**Static (N)**	**Dynamic (N)**	**Static M_tilt (Nm)**	**Dynamic M_tilt (Nm)**	**weight (kg)**
CRTICAL LOADS				**1500**	**1500**	**500**	**500**	**60**	**60**	
BUILT IN SHD-25		66-110	11.3	10900	17900				129	0.280
THK CROSS ROLLER	RB7013	70-100	13	27700	19400					0.350
RBC C-BEARINGS	GA020CP0 *RBC	50.8-63.5	6.35	3020	2490	4800	7300	55	80	0.045
RBC C-BEARINGS	**GA025CP0 *RBC**	**63.5-76.2**	**6.35**	**3690**	**2710**	**5830**	**7870**	**80**	**110**	**0.059**
RBC C-BEARINGS (SEALED)	GA030CP0 *RBC	76.2-88.9	6.35	4400	2890	9810	8360	110		0.068
RBC A-BEARINGS	KA030AR0*RBC	76.2-88.9	7.35	5070	3020	14630	8810			**0.068**

The Safety Factor was calculated as $n_{sf} = 2.67$ which means they can withstand over twice the predicted loads. Furthermore, there are two bearings, which means the joint is safe from plastic deformation

4.6.3 Spring Bearings

The spring also needs a bearing to be supported. By adding a bearing, it constraints all possible movements, except rotation. The loads that the spring bearing is radial and bending.
To determine the radial force acting on the support of the spring, first it is necessary to calculate the reaction force on the spring support from the moment acting on the spring. By assuming a maximum moment of 100 Nm the force is

$$F_r = \frac{\tau_s}{R} = 3300\ N$$

Where Ts Is the Spring torque and R the distance from the center to the support.
Thus, the bearing should be able to withstand this load.

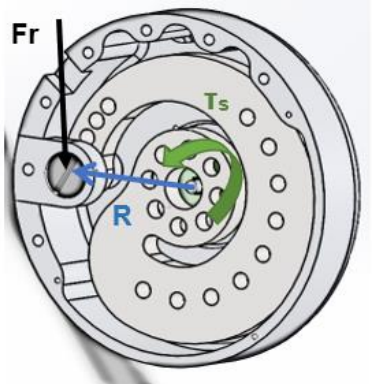

Figure 36 Reaction force felt on the spring connction to the housing

The Bending moment acting on the bearing is caused from the distance of the spring relative to the bearing location. This is calculated as

$$M = F_r * d = 67\ Nm$$

Which is quite large. It was desired to eliminate this bending moment. One solution was to use angular contact bearing, or cross-roller. The problem with the cross-roller bearings were too heavy to use. The issue with the angular contact was that the manufacturer does not produce sealed angular contact bearing, and the one provided were not easily available. Therefore, the last resort was to add a second bearing, cancelling the bending moment.

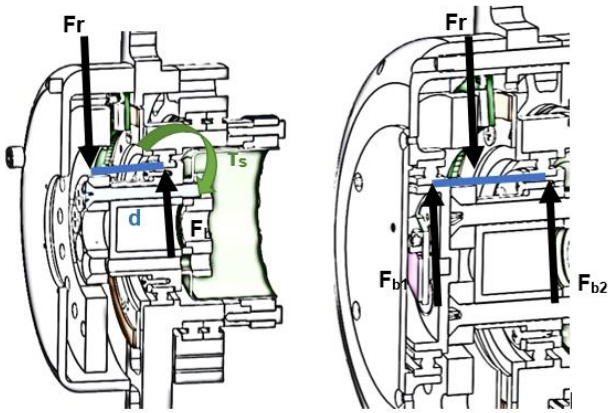

Figure 37 addition of 2nd bearing to compensate for bending moment

The configuration can be modelled as a simply supported beam. It can be observed that after inserting the second bearing, the loads are distributed to each bearing and bending moment is eliminated.

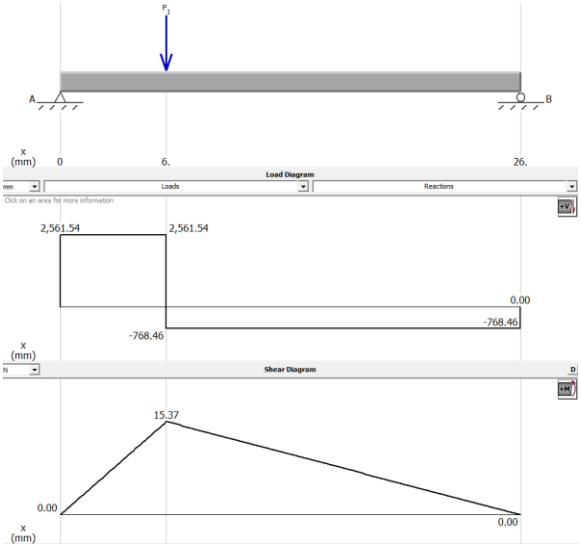

Figure 38 Shear forces and bending moments on the shaft

SKF radial ball bearings were then selected to take the radial load.

The Safety Factor was calculated as $n_{sf} = 1.93$ which means they can withstand the predicted loads. Furthermore, there are two bearings, which means the structure is safe from plastic deformation.

Table 19 Options for Spring bearings

SPRING BEARINGS										
				Radial		Thrust (Axial)		Tilting moment		
BEARING	Bearing number	**Bore -Outer diameter(mm)**	**Width (mm)**	**Static (N)**	**Dynamic (N)**	**Static (N)**	**Dynamic (N)**	**Static M_tilt (Nm)**	**Dynamic M_tilt (Nm)**	**weight (kg)**
CRTICAL LOADS					**2500**		**200**		**0**	
SKF DEEP GROOVE	61810-2RZ	50-65	7	6760	6800	1690	1700	42.11	42.36	0.052
SKF DEEP GROOVE	61809-2RZ	45-58	7	6100	6300	1525	1575	33.91	39.24	0.04
SKF (SEALED)	**61808-2RZ**	**40-52**	**7**	**3450**	**4940**	**862.5**	**1235**	**17.19**	30.77	**0.04**

4.6.4 Conclusion

After the Component selection was complete, the mechanical design was made. The components discussed were considered as the most optimal commercial of-the-shelf components that can be utilized for the construction of a high-performance actuator. These are summarized in table 20.

Table 20 Final of-the shelf Components

Motor	Sunnysky M8 Pro KV170 BLDC motor
Transmission	Leaderdrive Strain wave gear LCSG-20-80-C-I
Torque sensor	Custom torsion Spring
Motor encoder	iC Haus iC-MU
Joint Encoder	Aksim-2 off-axis rotary absolute encoder
Spring Encoder	iC Haus iC-MU
Motor bearings	SKF 61803-2RZ
Joint Bearings	RBC C-bearings GA025CP0 *RBC
Spring Bearings	SKF 61808-2RZ
Seals	Trelleborg TRG000770

5 Actuator Mechanical Design

The actuator design is illustrated in Fig. 61 with labels. The cross-section below shows the main components in the actuator. It contains the following features:

- Brushless DC motor
- Harmonic Drive with zero backlash
- High resolution IC huis encoders
- High resolution RLS Aksim off-axis joint encoder
- Input and motor housing components
- Output link assembly
- Precision bearings for the output shaft, gearing and spring

The stator is attached on the housing (ground), while the rotor is connected to the harmonic drive with 80:1 speed reduction. The WG rotates with high speed. The FS is attached to the spring which is fixed on the housing, hence also fixed. The flexibility of the FS allows relative motion of the CS. The CS is connected to the Output link, which rotates with reduced speed. When there is a load on the output link, the torque required to achieve motion is transmitted through the CS, FS to the spring, which deforms. The high-resolution spring encoder can measure this deformation. By multiplying the measurement, we can measure the output torque. The Joint angle/velocity can be measured by the joint encoder, while the rotor speed from the motor encoder attached at the motor cover.

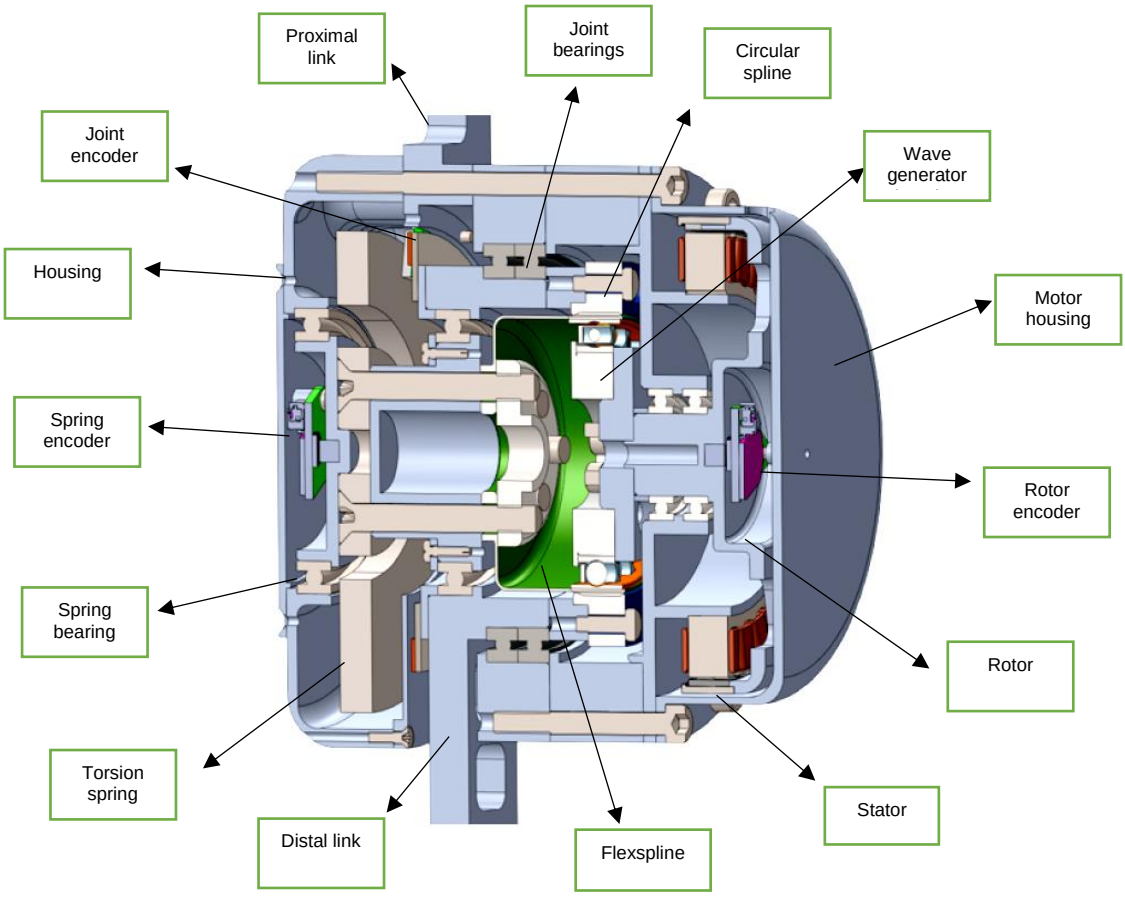

Figure 39 Actuator cross section view with components labeled

Figure 39 illustrates a frontal cross-section of the housing of preferred embodiment of the actuator assembly. Motor assembly is connected to the housing (proximal link). The Motor cover may cover the motor and houses a high-resolution on-axis IC Huis rotary magnetic encoder (the motor encoder may be an on-axis or off axis). The encoder has a magnet attached on the rotor and the readhead on the motor cover. The housing (proximal link) also holds a joint encoder whose readhead is attached on the housing and the

magnet is attached on the distal link. The joint encoder may be a magnetic encoder with a circular magnetic ring, and it measure the relative angle between proximal-distal link.
The motor assembly is coupled to the Wave generator of the Strain gear. The Strain wave consists of the WG, FS and CS and is gear is enclosed in the housing. The FS is attached on a torsion spring. The CS is attached on the distal link producing the output motion. The distal link is supported by joint bearings allowing relative motion proximal-distal link. The joint bearings may be radial, angular contact or cross-roller in order to support axial load.
The WG rotates with high speed. Since the FS is restrained to the spring which is fixed on the housing, it deforms and causes the Circular Spline to rotate. Because of the flexibility of the FS, it allows relative motion of the CS. The CS is connected to the Output link, which rotates with reduced speed and increased torque.
Figure 39 illustrates a sagittal cross-section of the housing, where the torsion spring is located. In this embodiment the torsion spring is coupled to the FS on the one side and attached on the housing on the other side. The spring has attachment points on is center and its edge to connect to the housing. When there is a load on the output link, the torque required to achieve motion is transmitted from the CS through the FS to the spring, which deforms. A high-resolution spring encoder can measure this deformation allowing for torque estimation. The spring encoder is an on-axis IC Huis magnetic encoder with the readhead fixed on the housing and the magnet attached on the spring.

5.1 Mechanical Synthesis

In this section, a more detailed view of the components is discussed. The main parts are shown in exploded view and the assembly sequence is shown.

5.1.1 Motor Assembly

In figure 40 we can see the exploded view of the motor assembly. This consists of the custom U8 BLDC motor, the WG of the Harmonic drive and the IC Huis on axis encoder. On the left there is the WG (1) which connects to an adaptor (2) which then connects to the rotor (5) via M3 bolts. The stator (4) is connected to the housing (3) which is part of the housing. This part also holds the joint bearings (12) together. The motor cover (6) has holes for the power cable of the motor and the encoder cables to pass through. The encoder's magnet is attached on the rotor and the reader (7) on the cover (6), which reads the velocity when the rotor rotates.

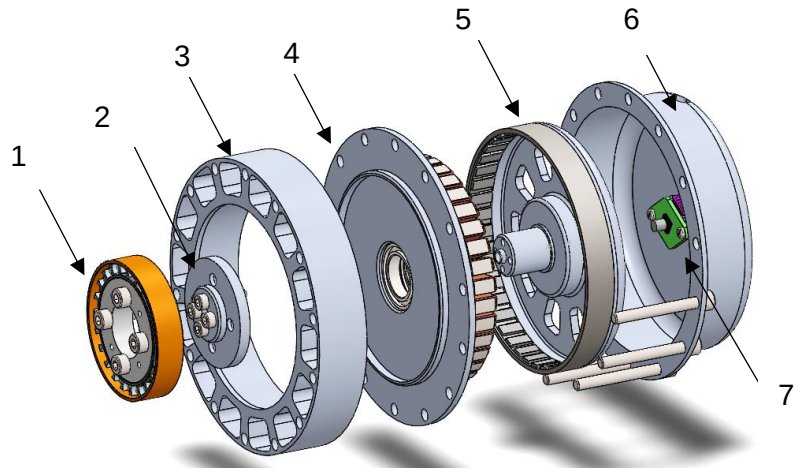

Figure 40 Exploded motor assembly view

5.1.2 Output Link assembly

In figure 41 we can see the Output link assembly. The encoder magnet (8) is screwed on the output link (9). The Spring bearings (11) along with the spring adaptor (10) fit in the inside surface of output link (9), while the joint bearings (12) fit on the outer surface of output link. A spacer (14) connects the output link with the CS (15). The reason the spacer is needed, is because of the threaded holes arrangement from the manufacturer of the Harmonic drive. The FS (16) is inserted inside the CS and is connected via M5 screws to the Spring adaptor (10). The housing (13) holds the bearings in place. The output link has threaded holes for attaching on the exoskeleton links.

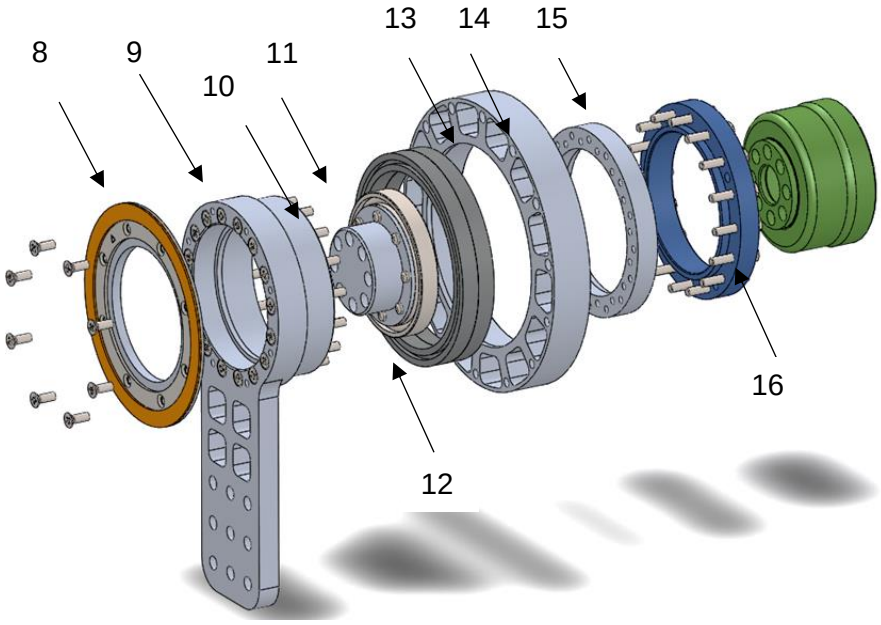

Figure 41 Exploded Output link assembly view

5.1.3 Input Link Assembly

Figure 42 shows the input link assembly. The torsion spring (20) is attached to the spring housing (19) using one M6 shoulder screw. Note that there is a bushing in the spring hole, which allows the spring rotation. That is because if it stays fixed, there is large stress concentration on the bolt. The input link (21) connects to the housing using long M4 bolts. This linked is part of the housing and is fixed via M4 bolts to the Spring cover (19). Attached on the input link is the reader of the RLS Aksim encoder (22), which reads the joint angles. On the other side, the spring encoder (18) is attached on a door (17). This door exists, to allow access to the screws connecting the spring to the FS at a later assembly stage.

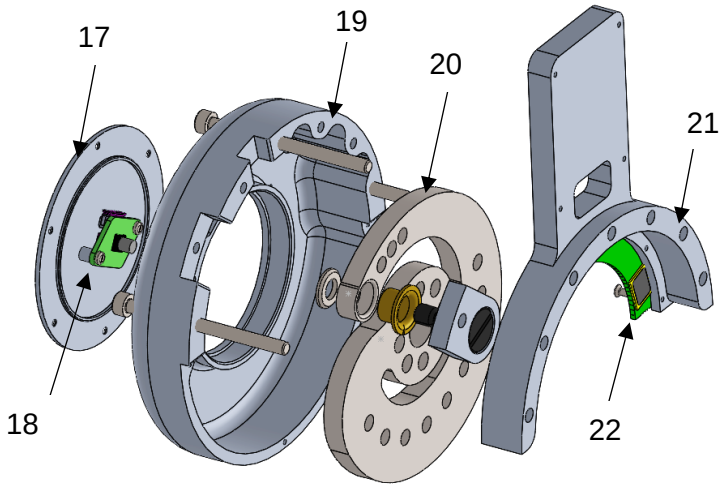

Figure 42 Exploded Input link view

5.1.4 Completed Assembly

For the assembly to be complete, the three main assemblies are connected via bolts. First the input link assembly and the output link assembly are joined via Screws as shown in figure 43. The spring must be screwed on the Spring Adaptor-FS.
The next step is to attach the motor assembly. However, first grease is applied inside the rotating parts of the HD, specifically the WG, FS and CS. Then the Motor-WG assembly is carefully aligned and screwed on the main assembly using M4 bolts. This process is shown in figure 44.

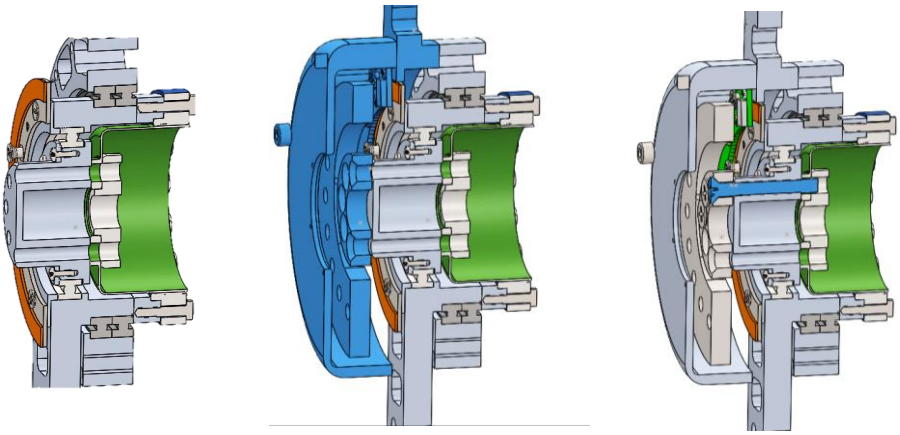

Figure 43 Assembling main components

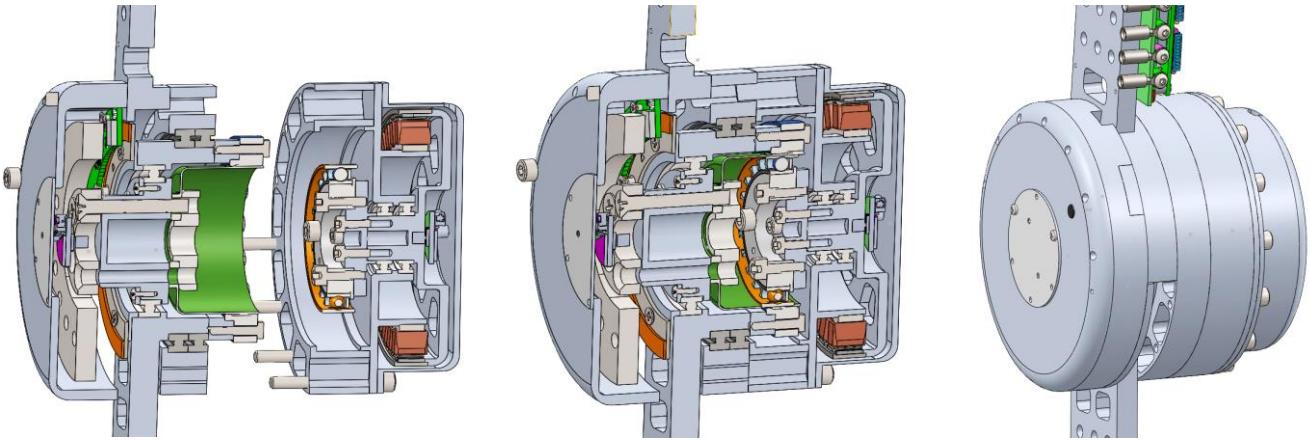

Figure 44 Assembling motor assembly

5.2 Housing

The housing for each actuator was designed to provide easy mounting to structure and a rigid output to protect the encoder for reliable movement. To reduce cost and weight, all machined components are made of grade 7 aluminium. Aluminium 7075 is considered a good option as it is tempered.
The housing covers all critical parts and seal the lubricated parts.
In the housing design, tolerances were a major design concern. If the parts were not properly centered, there would be radial loads which could damage the actuator. Thus, to ensure concentricity, alignment features were designed on the parts.

Figure 45 shows the housing parts. Structural optimization was attempted to reduce the weight. The extruded cuts were made to remove excess material, resulting in lighter design.

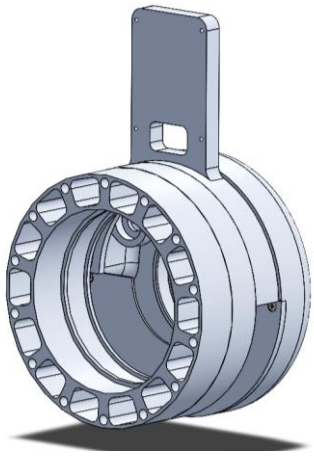

Figure 45 Housing after weight reduction

The mechanism's housing components were designed and manufactured using computer-aided design and computer aided manufacturing (CAD/CAM). The manufacturing processes used to create the prototype were end-milling and turning. Also, the anodizing process was used to increases resistance to corrosion and wear. First, the Solidworks program was used to create the 3D models of the components, and to define their dimensions. Then, the models were sent to manufacturers which used CNC milling and lathe tools to machine the workpieces.

5.3 Torsion Spring Design

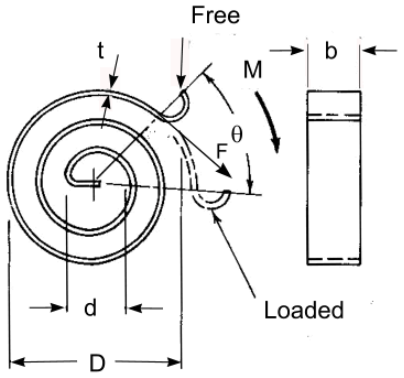

Figure 46 Spiral spring design parameters

A spiral spring consists of a strip or wire wound in a flat spiral. This is subject to a torque to produce an angular deflection.
The spring rate k is defined on this webpage as the torque (Nm)per unit angular deflection (θ).

$$k = \frac{M}{\theta}$$

Length of strip

$$L = \frac{\pi n(D + d)}{2}$$

Spring Rate

$$k = \frac{Ebt^3}{12L}$$

Where E is the material's young modulus
b the spring width, t the strip thickness
Spring surface stress

$$\sigma = \frac{6M}{bt^2}$$

Where M is the Moment acting on the spring
A simplified version of the spiral was designed, however there were difficulties to design attachment parts of the spring. Therefore, a different approach was considered.

Helical Torsion Spring with rectangular cross section:

For a straight torsion end spring, end corrections such as Eq. (10–46) must be added to the body-coil deflection [64]. The strain energy in bending is, from

$$U = \int \frac{M^2 dx}{2EI}$$

For a torsion spring, $M = Fl = Fr$, and integration must be accomplished over the length of the body-coil wire. The force F will deflect through a distance $r\theta$ where θ is the angular deflection of the coil body, in radians. Applying Castigliano's theorem gives

$$r\theta = \frac{\partial U}{\partial F} = \int_0^{\pi DN_b} \frac{\partial}{\partial F}\left(\frac{F^2 r^2 dx}{2EI}\right) = \int_0^{\pi DN_b} \frac{Fr^2\, dx}{EI}$$

Substituting

$$I = \frac{bh^3}{12}$$

For a rectangular cross section, we get

$$\theta = \frac{12\,\pi\,DMn}{Ebh^3}$$

The spring rate *k* in torque per radian is

$$k = \frac{Fr}{\theta_t} = \frac{M}{\theta_t} = \frac{Ebh^3}{12 * \pi DN}$$

The bending stresses on the surface are calculated as

$$\sigma = K_i \frac{Mc}{I} = K_i \frac{6M}{bh^2}$$

Where M is the maximum torque set to 100 Nm.
By tuning the parameters, the desired stiffnes was k=2000 Nm/rad, that is because sensitivity analysis in chapter 3 showed that this spring constant is sufficient to provide sufficient transmissibility bandwidth. Also it is not too stiff and a good encoder can capture its deflection. A rough stiffness estimation can be obtained by the displacement

$$\theta = \frac{\delta}{r} \qquad k = \frac{M}{\theta}$$

CAD models in Solidworks software were created and simulations on determining the spring rate and the stresses. However, there are three design parameters that make the spring rate. The material was chosen to be titanium Ti-6Al-4V, for its excellent strength and low mass, thus the E is fixed. The diameter D, b and h and E. The spring diameter is limited by the diameter of the actuator; therefore, it was set fixed. The parameters determining k, then is h and b.
The requirements set for the spring were:

- K = 2000
- σ < 450 MPa
- D <= 88 mm due to design constraints
- m = minimum

An optimization approach was used to optimize the Spring design to get the desired Spring rate, while maintaining under the critical stresses. The fatigue limit for titanium is Sy=0.61Sut = 500 MPa and with a safety factor 1.15 the limit is set to 470MPa

The optimization function has the purpose to minimize the mass while the constraints are:
k_d = 2000 and σ less than 470MPa
The optimization function works as follows:

$$\underset{h,b}{\text{minimize}}\ m = \rho LA = \rho * \frac{\pi n(D+d)}{2} * bh$$

$$Subject\ to\ constraints: \quad \frac{Ebh^3}{12 * \pi Dn} \leq k_d$$

$$\frac{6M}{bh^2} \leq Sy$$

$$D \leq 0.1$$

Where the constraints are non-linear. The function describes the mass and tries to minimize their sum. The parameters set to change are the spring's thickness *h* and the width of spring strip *b***.** These parameters determine the total size of the spring and cross-section. The diameter is set fixed.
The boundaries were set to:

- b < 8 mm for the b
- h < 25 mm for the h
- D < 89 mm for the Diameter D

The optimization is performed using MATLAB and the ‘fmincon’ function because the design variables are constrained.
The results were h = 23 mm and b = 7 mm, D = 89mm
Which means that b needs to be maximum to reduce stresses, while maintaining the k. this makes sense as the k depends on h^3 while σ depends on h^2 while both depend on b^1. Thus, by changing h, it influences k more.
The first prototype was designed, and simulations were carried on in Solidworks:

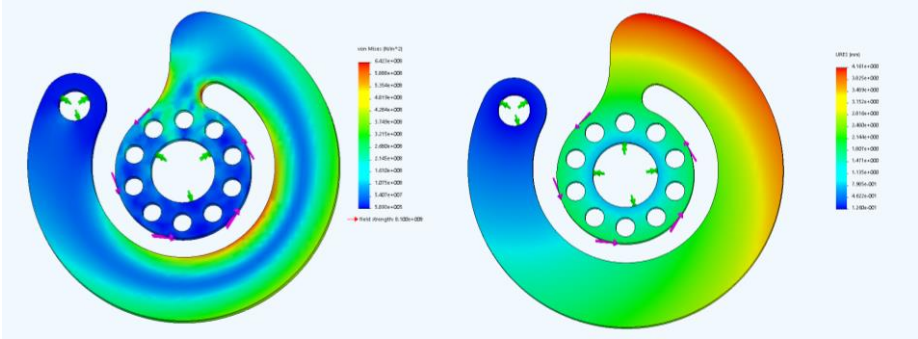

Figure 47 Initial Spring design

Initially there were high stress concentrations in the parts shown in the figure. That is because the force acting on the hinge on the left, exerts high bending stress on these parts, as the moment arm increases. Therefore, the strip width was increased. The stresses were still high on the left, but very low on the right. Thus, it was decided to make the strip width variable. One way to do this is by using the equation:

$$r_i = r_{i_0} + \lambda \sqrt{\theta - \frac{\theta}{2\pi n \theta}}$$

in polar coordinates.
However, the spring strip had to be modified manually at some parts because of the stress concentrations. The resulting strip width increases up to 180 degrees, and then it is reduced.
It was observed that the stress concentrates the bottom of the inside radius of the spiral, the reason is because the bending stresses are higher there, as the moment arm from the fixture is high.

After some manual iterations the following spiral shape occurred shown in figure 48. To minimize the weight even further, material was removed from the middle radii, where the stresses are low. This resulted in weight reduction and also made stress distribution more uniform.
This greatly reduced the stresses, and also the mass. The final weight of the spring is 110 grams and the stiffness is 1910 Nm/rad, while it can handle 100 Nm without reaching its yield.

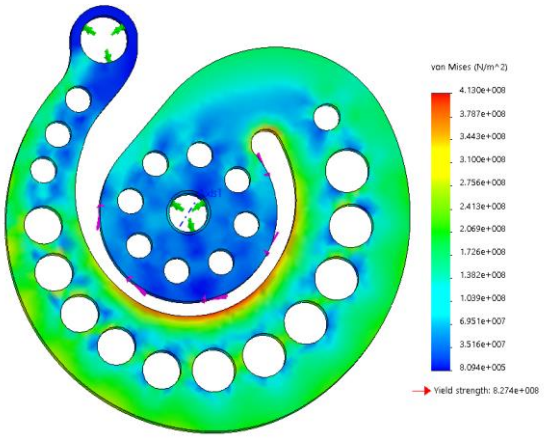

Figure 48 final spring design and stress distribution

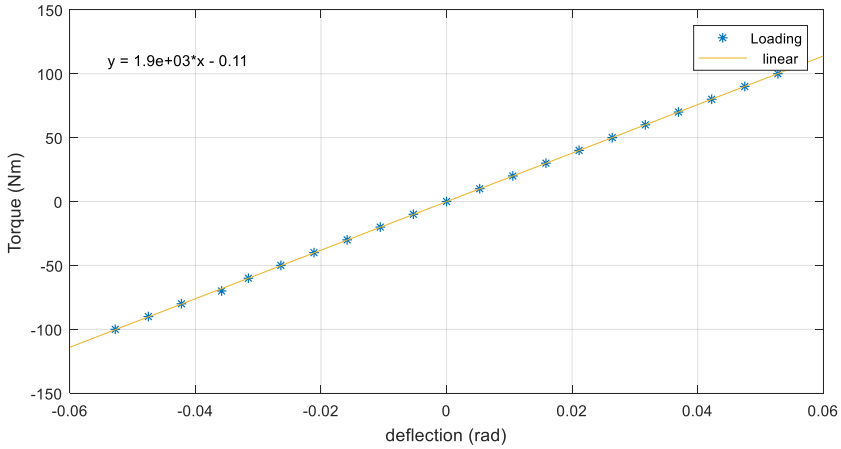

Figure 49 Spring Constant Linearity test

The spring linearity was tested in Solidworks simulation. It can be observed that the spring exhibits highly linear behaviour. The linearity is estimated to be 99.9%

5.4 Structural Simulations

This section deals with the structural integrity of the critical components of the actuator. Some parts receive large forces thus a structural analysis was necessary to ensure their integrity. The loads acting on the parts have been found from the dynamic analysis discussed in chapter 5. The analysis was made in Solidworks simulation.

5.4.1 Spring Stress Analysis with Bolt Preload

A simulation with the spring was made using preload of the bolts. The parts connected are the spring, the bolts and the spring adaptor. There are 8 countersunk bolts holding the spring in place.
The upper attachment point of the spring is modelled as a hinge. The spring connector is also modelled as a hinge. The preload torque was defined as 8 Nm for each bolt.

As shown in the figure, the maximum stresses are 417 MPa and the maximum deformation is 2.4 mm.
As expected most stresses are located on the spring.
Specifically, on the inside curve and the small curve where the spline starts.
The spring is made of titanium with fatigue strength (at 10^7 cycles) 500 MPa and yield 800 MPa.
These results indicate that no failure will occur to the spring. The safety factor is 1.2 which is enough for this kind of application.
The maximum deformation is 2.44 mm, which is acceptable, as the space between the spring and the Cover is 3.5 mm.

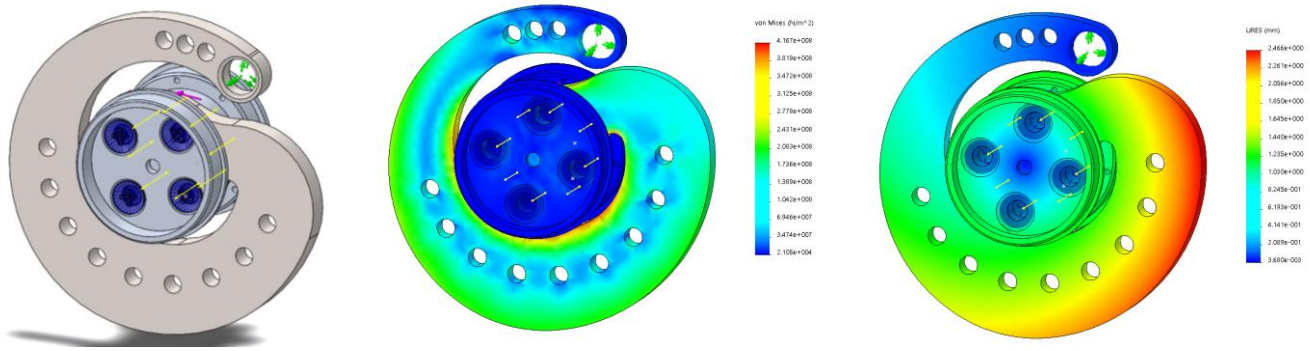

Figure 50 Spring assembly Simulation

5.4.2 Spring Cover Simulation

A simulation was made to determine the stresses on the bolt that fixes the spring on the housing.
There are two parts holding the bolt; a spacer where the bolt head lies and the other one is the spring cover, where the bolt is threaded.
The spring cover is considered fixed. The spacer is restricted inside the boundaries of the cover as shown in the figure. The maximum force acting on this part was calculated in section 6.6 and is 3330N.
The results showed that the maximum stresses are concentrated in the part where the head of the shoulder screw lies as expected. Therefore, the width of this part was increased to handle this load.
Finally, the stresses were estimated at 108 MPa, which is far below yield limit of aluminium 7075, (435 MPa) and below its fatigue stress (160 MPa). That gives a safety factor of 1.5. Thus, it is ensured to hold this load.

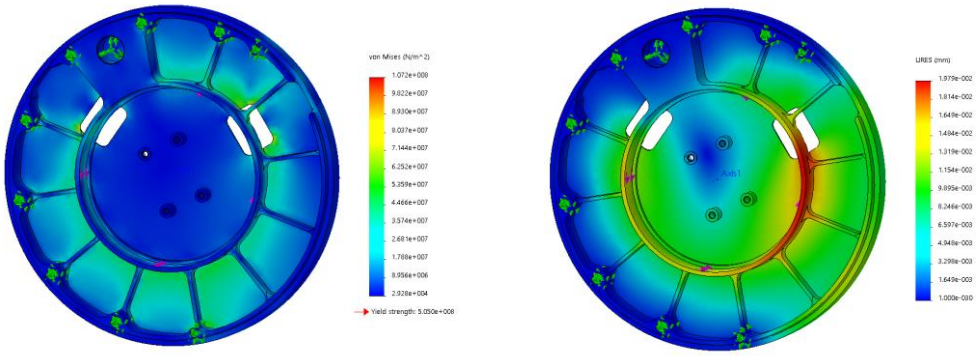

Figure 51 Spring Cover Stress simulation

5.4.3 Structural Optimization of Housing Parts

During the design, a weight reduction technique was adopted to remove excess material from the housing parts that is redundant. Ribs structures were designed to increase the structural integrity, while reducing the weight. The resulting shape is shown in the figure below. Therefore, a stress analysis was made to ensure the walls were not too thin.
The simulation showed that the stresses are quite low, thus the structure is safe from failure.
Table 21 summarizes the simulations results.

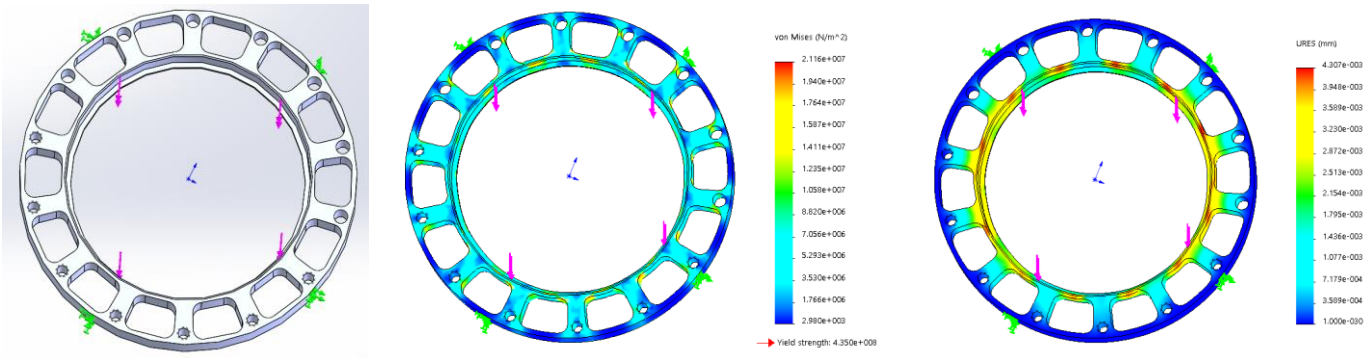

Figure 52 Housing simulation

Table 21 Safety factors for critical parts

Component	*fatigue Stress (10^7 cycles) MPa*	*Max stress MPa*	*Safety Factor*
Spring	500	417	**1.2**
Spring Cover	160	108	**1.5**
Housing	160	21	**7.6**

5.5 Design Challenges

Many challenges were faced during the design process, mostly because of the weight and size restrictions. The main challenge was to create a lightweight design, while maintaining structural integrity.
The total mass of the (first version) of the actuator was calculated at 1.790 kg, the width 103.5 mm and the diameter 108 mm*. Maximum emphasis was given to weight and size reduction. Moreover, the actuator consists of many separate parts, to allow simpler manufacturing, having a trade-off in more complicated assembly procedure. Inserts were made to ensure concentricity between the parts.
All aluminium parts were designed in a simple way, so that they can be milled easily on a 3-axis CNC milling machine and turned on a lathe machine. The aluminium used is 7075-T6, an aluminium alloy that is quenched and has high ultimate strength.

The most challenging part to manufacture is the torsion spring. The spring was manufactured with EDM Wire Cutting, as it cannot be manufactured with common CNC machining techniques. In wire electrical discharge machining (WEDM), a thin metal wire is fed through the workpiece, submerged in deionized water. This method can be programmed to cut delicate shapes.

More challenges were faced from manufacturer's constraints. For example, the HD manufacturer, only had specific sizes of components. There was a mismatch between CS thread alignments, as because the bolts inside the CS threads, could touch the joint bearings. The next size of thin section bearings was 12mm larger in diameter, which would largely increase the actuator's diameter. For this reason, a compromise was made by designing a separate part to connect the CS with the distal link.

Another problem faced was the addition of two bearings for the spring (As explained in Ch7, to hold the bending moment). The extra bearing increased the width of the design.
More similar problems were faced, which led to the current design. However, this is a first prototype, and the mechanical design can be improved in a second version.

**In the latest version of the actuator, the mass was reduced to 1.633 kg, with the width 89mm and max diameter at 102mm.*

5.5.1 Tolerance Stacking

The parts tolerances were a challenge. Because there are many parts connected, there was a concern about tolerance stacking, therefore particular precision desired in tolerances. The most critical parts were the encoder's tolerances and the bearings' tolerances. The encoder must be 0.2mm from the readhead, thus the tolerance stacking of the parts should be within this range.

6 Experiment Design

To test the capabilities of the rotary actuator and the torsion spring, tests are necessary. These tests are designed to test each aspect of the design by verifying calculations and validating finite element models. The spring stiffness needs to be measured to get accurate torque measurements. A stiffness estimation has been made, but the real result may differ from the simulation. Then the characteristics that need to be tested is the torque production of the actuator and power output. Then the performance can be determined.

6.1 Test Hardware Description

A rigid test stand was designed to perform the experiments. This is shown in figure 53 below. The test stand is a plate fixed on two ribs, which are then fixed on a rigid platform. The plate has a large hole to place the actuator and there are holes drilled on it to fix the actuator.

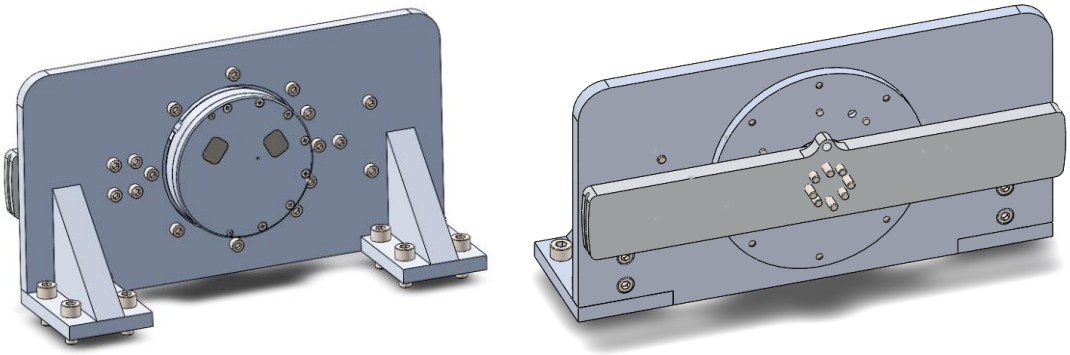

Figure 53 Test setup for Spring stiffness calibtation test

6.1.1 Electronics and Sensors

The sensors used are the AksIM and the two IC Huis absolute magnetic encoders. The first IC Huis measures motor angle, the other IC Huis measure spring angle and the AksIM measures joint output angle the sampling frequency is 1 KHz. The three encoders connect through to the Servo drive. The Servo drive used is a custom-made servo, called Modular Servo Drive (MSD). This device operates from 20 –48 VDC and has a maximum continuous current of 5 A, for a power range of 50 to 240 watts. The servo drive is powered by a power supply which regulates the voltage to the motor. The servo connects to a Linux operated PC via ethernet cable. The input currents and output signals are given through Simulink. A current limiter limits the current for safety.

6.2 Spring Stiffness Calibration

First experiment is to test the stiffness of the spring. The test for measuring the spring constant is a simple experiment using a pulley and weights, shown in figure 54. The pulley was chosen as more proper solution, to remove the sinusoid from the equation. The pulley keeps the force constant. To reduce manufacturing costs, the pulley was redesigned to a lever with rounded edges, same as the radius of the pulley. Since the angles we are measuring are small, the lever was a cheaper solution. The spring constant is measured as

$$K_s = \frac{mgr}{\theta_s}$$

The test is executed as follows. A number of weights are accumulated on the edge of the rope, producing a known torque. At each step, the weights are known, and the spring's angle deflection is measured and recorded using the IC Huis 16-bit resolution encoder. The weights are slowly increased up to reaching the maximum torque required. After reaching the maximum, the weights are decreased in each step and then recording the angle. Thus, by testing with different weights, we measured the stiffness to check if the spring is linear.

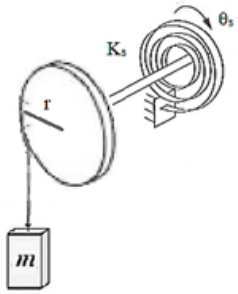

Figure 54 Experimental Setup for measuring the spring rate

6.3 Torque Density Evaluation

A design goal was to maximize performance. To measure the performance, we need to attempt to reach the mechanical limits of the actuator components in a safe controlled manner. Two experiments were designed to push the actuator to its limits. These are explained below.

To measure the peak torque that the joint is required the following experiment is designed: the actuator is output is locked and the torque is measured. We input sinusoidal current to try to achieve the required torque. Slowly increase the amplitude, creating motor torque which causes the spring to deflect. A current – torque curve can then be constructed. The output torque is measured as:

$$\tau_l = K_s\theta_s + k_\tau i$$

Torque density is calculated by dividing the maximum torque with the mass of the joint

$$r_{tw} = \frac{\tau_{l_{max}}}{m}$$

A rough estimation of the efficiency can be estimated in the following way:
Since the output link is fixed, the constraint relationship become

$$\theta_m = \frac{\theta_s}{N}$$

From the power conservation we get:

$$\eta\tau_m\dot{\theta}_m = \tau_s\dot{\theta}_s$$

Where η the total actuator efficiency, then an estimation of the efficiency would be:

$$\eta = \frac{\tau_s}{N\tau_m}$$

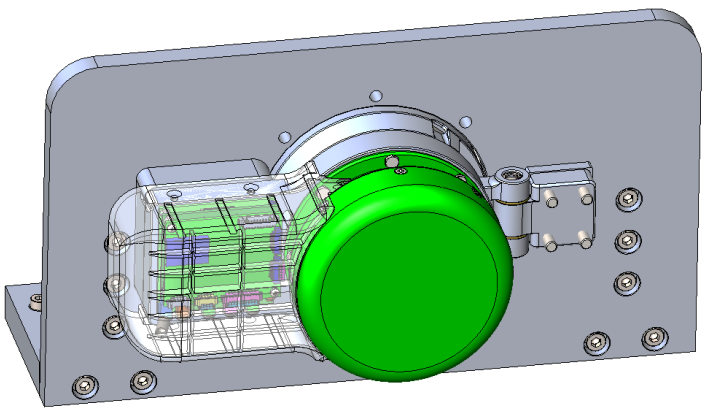

Figure 55 Test stand for torque density test

6.4 Power Density Evaluation

This test is designed to measure the maximum power the actuator can output. The experiment is explained as follows. The one end of the actuator is fixed, while the other is free to rotate. A weight is attached on the moving link and the actuator is commanded to track a position (sinusoidal). The actuator should be able to track the reference position closely with a high velocity. Measure torque and velocity outputs. The torque is known from the weight times the moment arm.

$$P_{out} = \tau_l \dot{\theta}_l = (K_s \theta_s + k_\tau i)\dot{\theta}_l$$

Power density is calculated by dividing the maximum power with the mass of the joint

$$r_{tw} = \frac{P_{out_{max}}}{m}$$

Efficiency:
The efficiency is defined as the ratio of the output to input power. The output power is measured from the previous measurements. The input Power can be measured from the current of the power supply.

$$\eta_{tot} = \frac{P_{out}}{P_{in}} = \frac{\tau_l \dot{\theta}_l}{\tau_m \dot{\theta}_m}$$

7 Results

This chapter presents the results gathered from the analyses done in previous chapters and the results of the experiments described in chapter 6. In the end of the chapter, a table is presented which summarizes the achieved results of this project.

7.1 Simulations Results

The simulations showed that, compared to other SEA configurations, the TFSEA configuration has equally good torque transmissibility and sensitivity bandwidths and similar impedance. The configurations show no significant differences. The transmissibility plot showed that the actuator can transmit torques for up to a frequency of 17 Hz. The sensitivity plot showed that the sensitivity remains 1/2000 rad/ Nm for up to this frequency, which means that it does not limit the torque transmission. Impedance seems to be increasing with increasing frequency.

Torque sensing accuracy simulation:
The torque sensing accuracy simulation showed that the TFSEA's spring deflection is not proportional to the output torque, as there are other dynamic components such as motor inertias, bearing friction and the motor torque Tm affecting it. In section 3.2 it was shown that inertias and bearing friction terms are negligible in our application (measuring much higher torques), but the motor torque cannot be neglected as it does affect the torque resolution. However, a very good approximation of the output torque can be achieved in the TFSEA configuration by combining the spring measurements with motor current measurements.

By ignoring the motor torque, the maximum error in the measurement would be 0.902 Nm. Even though it appears slightly high, it is still sufficient for our application, as the requirement set was 1 Nm. A small concern would be controlling low torques. On the other hand, if the motor torque is estimated, or measured, a much better torque resolution of 0.125 Nm can be achieved.

The simulations showed that, to increase the bandwidth, high stiffness is needed. However, the tradeoff is that the spring deformation becomes smaller with respect to external torque, therefore we needed a high-resolution encoder to compensate for this. With a spring of stiffness 1979 Nm/rad, the torque resolution with the 16-bit magnetic encoder is estimated at 0.19 Nm per step.

7.2 Spring Stiffness Calibration Results

The results of the spring calibration are presented in Figure 56 (Left), which shows the spring load-deflection curves for loading and unloading conditions. For each condition the test was made in the clockwise (CW) and counter-clockwise direction (CCW). The spring rate results showed that the spring is highly linear both conditions and regardless of direction. Regression was made to construct the linear fitted curve.

As shown in figure 56, the spring rate is estimated as the slope between torque and deflection with value between 1979 Nm/rad. The spring exhibits no hysteresis or any backlash close to the zero point. The correlation coefficient showing the linearity is estimated at 99.99%.
Comparing this value with the simulation, it is observed that the difference is 3.99%, which means the simulation was very accurate.

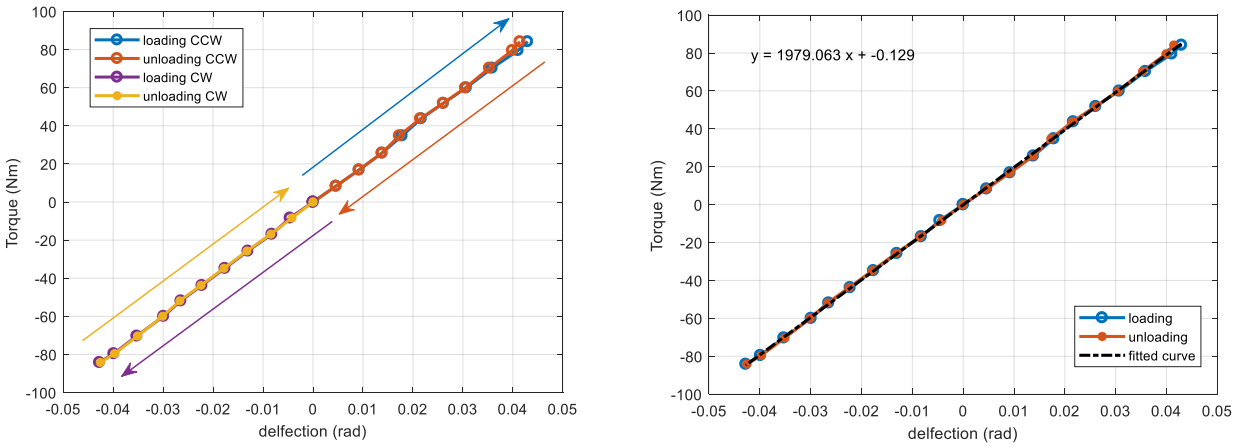

Figure 56 Experimental results and fit curves for loading and unloading the spring

By plotting the residuals of the curve, one can see how far the measurements are from the curve. Figure 56 shows the torque measurement error with respect to the fitted spring curve. The maximum error is 2.3 Nm (it is an outlier), while the root mean squared error for loading is 0.81 Nm. This value indicates the mean error in the torque measurement with respect to the expected value.

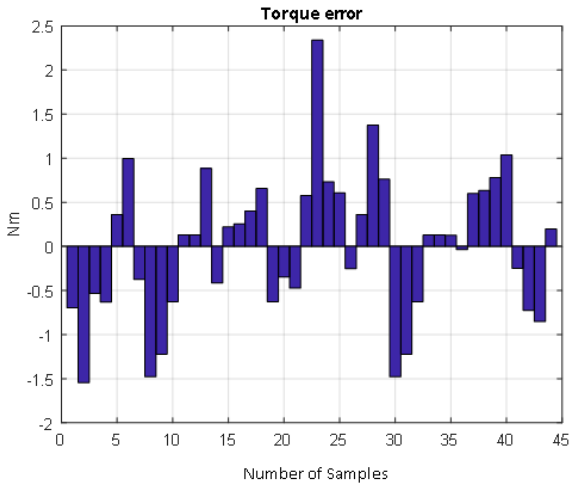

Figure 57 Torque residuals error

The titanium torsional spring was designed with predicted stiffness of 1900 Nm/rad and the manufactured prototype actually achieved a higher stiffness of 1979 Nm/rad, thus the simulation was successful and very close to the experimental results. Moreover, the spring was able to withstand 57 kg with a 0.15m radius as moment arm, thus a total of 84Nm moment without significant effort. This shows that this design is robust and can be used in this application safely.

The spring has to be stiff enough to provide sufficient bandwidth, but also not too stiff, so that the deflection can be measured with the 16-bit magnetic encoder accurately. The spring's mass optimization minimized its mass to 110 grams, while the stress simulation showed that it can handle up to 100 Nm without reaching its yield strength. The stresses at a torque of 100Nm were estimated at 408 MPa, which is far below fatigue limit of Ti-6Al-4V, (500 MPa), which gave a safety factor of 1.2.

7.3 Torque/Power Density Measurement Results

The torque density test was not performed, due to time limitations. The reason is because some manufacturing issues delayed the assembly, thus there not time to run the test. However, some initial estimations of the torque and power estimations were made.
Torque density is calculated by dividing the maximum torque with the mass of the joint

$$r_{tm} = \frac{\eta(N+1)\tau_{m_{max}}}{m} = \frac{0.6 * 80 * 2.3}{1.633} = 67.6\ Nm/kg$$

Since the torque ratio is 80, the maximum capability of the motor is 2.3 Nm and the joint mass is 1.63kg, then by assuming a conservative mean efficiency of 60%, then the torque density is estimated at 68 Nm/kg. However, it has to be tested, to validate this result.

Eventually the power tests were not performed, due to time limitations of the project. To perform this test a position controller was needed, to track the desired position. Nevertheless, this test was designed already and will be done in the near future. Then the power-to-weight ratios and power to volume ratios will be extracted, to proof the high performance of the system.

7.4 Design Achievements

The weight of the joint including the links is 1.63 kg. This was achieved by choosing powerful and lightweight components and leveraging the design of the housing parts. To reduce cost and weight, all machined components were made of aluminium 7075-T6, a lightweight aluminium alloy that is quenched and has high ultimate strength. During the design, rib structures were designed to increase the structural integrity, while reducing the weight. The stress analysis showed the structure is safe from failure. Indeed, during the tests, no failure was encountered, which proved the robustness of the design.

After the spring calibration, the torque resolution was estimated as the sum of the encoder resolution, the rms error from the inertial, friction effects, errors occurring from the current measurement and the rms error from the spring curve. Assuming the current measurement error is negligible, the resolution is:

$$res = T_{enc} + T_{ef} + T_{es} + T_{em} = 0.19 + 0.125 + 0.81 + 0 = 1.125\ Nm$$

Which is a very good resolution for this application as it is 1.35% of the maximum torque. This result is considered sufficient for torque control of the exoskeleton joint.

Finally, the results are summarized in table 22.

Table 22 TFSEA Actuator Specifications

	Requirements	Achieved
Spring Stiffness	2000 Nm/rad	1979 Nm/rad
Mass (Including links)	1.5 Kg	1.633 Kg
Torque resolution	<1 Nm	1.125 Nm*
Peak joint Torque	>80 Nm	110 Nm*
T/M ratio	53 Nm/kg	68 Nm/kg*
Peak joint Power	>100 W	540 W*
P/M ratio	74 W/kg	330 W/kg*
Mean Efficiency	highest	0.6-0.8*

**the values with * are estimated and need yet to be validated through experiments.*

8 Discussion

In the beginning, we defined the challenges that this project tried to overcome.
These were to influence mechanical design

- to increase performance while decreasing weight and size,
- to achieve compliancy without limiting the torque bandwidth and
- to overcome practical challenges concerning torque sensing issues.

This chapter discusses the results to conclude whether these challenges were countered, what went right and what wrong, and what were the lessons learned during this project.

8.1 Comparison to State of the Art

Performance
The first goal of this project was to increase performance and reduce size. More specifically, the design goal was to achieve 1.5 kg, which is very lightweight for a SEA, even for a stiff actuator without spring of similar applications. The achieved mass of the actuator is 1.633 kg including the input and output links.

Even if higher than the initial goal, this weight is still an impressive achievement, considering that the actuator is capable of more than 110 Nm output torque. If the estimations are correct, the torque density would be 68 Nm/kg (or higher). Compared to other similar state-of-the-art actuators, this would be the highest. The UT-RFSEA and BLEEX actuators, which have the highest torque densities have 51 and 49 Nm/kg which is nowhere near the torque density of our actuator. Of course, these estimations need to be validated to establish this claim.

The steps that led to this result were careful component selection after a rigorous comparison of actuation technologies, transmissions and configurations. Moreover, the intelligent design and rigorous revision of the CAD modelling managed to achieve a very compact size, with a width just 89mm and maximum diameter of 102mm. The width is very important to be small, as the exoskeleton is desired to fit in a wheelchair with the patient. The CAD was revised ten times, producing eventually the eleventh version of the CAD model as the final version.

Compliance
The second goal of this project was to design a compliant actuator without limiting the torque bandwidth. Thus, we designed a titanium torsional spring with stiffness of 1979 Nm/rad. The spring's mass optimization minimized its mass to just 110 grams, and width of 7mm, while the stress simulation showed that it can handle up to 100 Nm without reaching its yield strength with a safety factor of 1.2.

The most significant achievement is the stiffness linearity of the spring. As shown in figure 56, the linearity of the spring achieved is 99.99%. Compared to other researches, it is an excellent result, as most studies show some form of backlash or hysteresis [65],[66],[14]. In contrast, our spring did not have any observable backlash or hysteresis. Our results are comparable to the spring of MINDWALKER, [12], with the difference that our spring is half the weight and more than twice the stiffness.

However, there are flaws in the design of the spring too. For example, there is only one attachment point to the housing. This could have presented eccentricity if not taken care of or could produce high stresses if preloaded with high force during the assembly. With two attachment points (for example double spiral) concentricity is ensured.

Furthermore, the high stiffness ensures to achieve high torque control bandwidth. The simulations in chapter 3 showed that the TFSEA actuator has a transmissibility bandwidth of 17 Hz which is higher than the required 5 Hz.

8.2 Justification of the TFSEA Choice

The final goal was overcoming practical challenges concerning the spring encoder. Due to the configurations' structural differences, a major practical challenge in the actuator design is determining the

placement, attachment, and type of the encoder to measure the deformation of the spring. The encoder needs to be placed on the housing, while having its magnet on the spring.

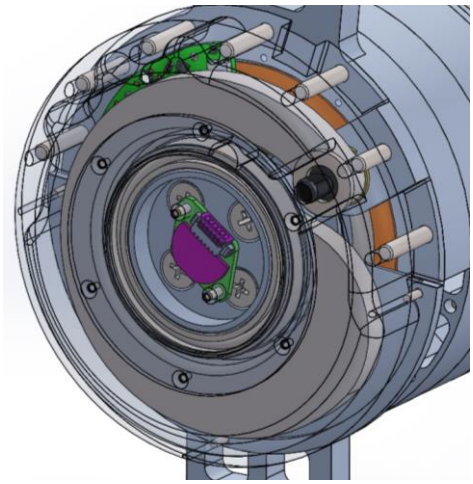

Figure 58 Spring encoder of the TFSEA design

Placing a spring encoder in the conventional rotary FSEA is difficult, because the spring has no end connected to the housing. The readhead is difficult to place on the housing and may be placed on the output link. As a consequence, the cables may rotate or twist and thus slip rings may be necessary. The only option was to place the readhead on the distal link, but doing so, a slipring would be necessary, as the distal link rotates with respect to the housing (proximal link), thus the encoder readhead also rotates. Usually spring deflection is measured using the difference of the angle motor encoder and joint. Therefore, there is noise from two encoders and it is not so accurate due to the kinematic error of the harmonic drive.

The drawback in the RFSEA design is that the spring encoder's readhead must be placed on the stator, which rotates, causing its cables to rotate too. Moreover, the RFSEA was more challenging to design because the spring's bearings placement would result in an increase in the width.

By utilizing the TFSEA configuration allowed us to place the encoder coaxially between the spring and housing, which solved the cable management issue, which has been a major challenge. The spring encoder readhead is fixed on the housing, therefore all cables are stationary, and do not twist nor rotate. Moreover, the encoder position allows for very accurate measurements.

Compared to other SEA configurations, the TFSEA configuration has equivalent torque transmissibility and sensitivity bandwidth. The configurations FRF show no significant differences at low frequencies and minor differences at high frequencies. The only drawback of the TFSEA is that the torque resolution is affected by the motor current. This issue can be surpassed by measuring or estimating the current. This way the torque resolution would reach 1.125 Nm, which is sufficient for this application, as an appropriate torque controller can be achieved.

8.3 Overall Discussion

In this section the results we discuss some issues encountered, and what were the lessons learned in this project.

Issues encountered

Many issues were encountered during the assembly. In order to achieve this compactness of the joint, very precise tolerances were required, in the order of tenths of micrometers. The trade-off of minimizing the dimensions to this extent was that it made the assembly more complicated, as careful fitting of the parts was necessary to avoid contact of moving parts. This high precision was also a challenge for the CNC manufacturers, but the results were very good. Only a few parts needed to be modified or re-manufactured because they didn't match the fitting tolerances.

An issue faced was the sequence of parts comprising the spring assembly. In this sequence, five parts are connected by eight screws. The problem was applying enough preload to create enough friction to prevent the parts from moving relative to each other. This may have happened because the holes where the screws were passing by, had some clearance. The M5 screws can only reach up to 12 Nm preload, which may not have been enough to hold all the five parts.
In the next version, it was decided to reduce the amount of parts to four, by re-manufacturing two parts as one and also changing the screws to custom-made shoulder screws which ensure the clearance is non-existent.

A significant factor that was not considered in the design, was friction from the oil/grease seals. The seals actually introduced a lot of friction, much more than expected. This fact caused reconsidering of even placing them. In the first prototype, it was chosen to use sealed bearings instead of seals, presuming that the grease would remain sealed by the bearings. Since grease is more viscous than oil, the bearings seals should be enough to prevent leakage. During the tests, it was observed that this solution seemed successful, as no amount of grease leaked. However, there might be problems in the long-term use.

Another problem faced came from the thin section radial bearings which had an unpredicted issue. They had significant amount of axial play, which introduced large play in the joint. (Axial play is the relative axial movement of the inner ring with respect to the outer ring). This internal looseness was eventually removed by applying an axial preload using shims. The shims introduced axial preload to the inner and outer rings of the bearings, preventing them from relative motion. However, in the next design, angular contact bearings should be chosen, or duplex bearings, to avoid having to deal with this effect.

Lessons Learned
During this project, valuable lessons were learned. First, the design of this specific robotic actuator turned out to be an extremely rigorous procedure. That is because of the very strict constraints in spatial dimensions and mass set in the beginning. Furthermore, generating this concept took a lot of time and effort. Also, there was the risk whether the concept will work as expected, as there is little or no prior art, thus the concept was not yet proven to work. There were many uncertainties to take into account when designing, like tolerance stacking, ensuring concentricity, deformation of components, applying preload, thermal expansions, lubrication and these are only a just few.

By assembling the actuator, it came to the author’s understanding that the human input greatly affects the parameters of the system. For example, a small design error providing a higher tolerance in the bearing shaft, would make the bearing press-fitted and would compress the inner ring to the balls, resulting in increased viscous friction. Any step in the design has consequences later in the assembly. For this reason, all design steps had to be revised many times and even repeated, to minimize errors.

On the other hand, even if the design is perfect, errors from the manufacturing side would also affect the end result. Thus, one can argue that there is no perfect design. There will always be issues needed to be fixed. We engineers use the scientific methods (i.e models and simulations) to predict and solve these issues, but sometimes they are not sufficient, and thus practical solutions are applied to solve them [64]. This is where engineers differ from scientists.

Closing, this project had two aspects. The modelling aspect which includes the model and simulations, and the practical aspect, which is includes the assembly and testing. The major lesson taken from the practical aspect, is that the actual system differs from the simulations. The simulations are useful because they provide some insight of how the actuator will behave, but they don’t show the complete picture.

For these reasons the designer requires not only intellectual and temporal effort, but also experience. Experience allows the engineer to be proactive and be able to predict the problems before these occur. Mechanical engineering design is a continuous and repeatable procedure. Only by repeated testing and constantly improving, one can achieve optimal results.

9 Conclusions & Recommendations

9.1 Summary

In this work, we introduced the mechanical requirements of a high performance, lightweight exoskeleton actuator and defined the methods necessary to realise it. Models of different configurations of rotary SEAs using harmonic drive were analysed, which can be used for independent joint control. A Transmissive Force Sensing Elastic Actuator was designed and fabricated and a torque controller was proposed based on the model. The actuator utilizes a brushless DC motor with an 80:1 gear reduction from a harmonic drive. This actuator can produce torques similar to a human knee/hip joint and will be implemented in an exoskeleton in the near future.

9.2 Conclusions

A TFSEA actuator was fabricated. Light weight and compactness were achieved through many iterations of designing. Compliance was also achieved by designing a lightweight torsion spring and through mass optimization. Accurate torque sensing was achieved by placing a high-resolution encoder coaxially to the spring's axis, measuring its radial deflection. Our design solved a cable routing problem by allowing all the cables to be fixed on the housing.
The goal was to design a high-performance actuator. The experimental results showed the following:

- The stiffness of the spring was measured at 1979 Nm/rad.
- The total mass is 1.650 kg.
- The torque resolution achieved is 1.125 Nm.
- The 900 W motor provides up to 110Nm of peak output torque
- The torque density was estimated at 68 Nm/kg

9.3 Recommendations

Torque accuracy
Concluding, the simulations showed that a good approximation of the output torque can be achieved in the TFSEA configuration by using the spring measurements and the motor current. But to get the most accurate measurement, a Kalman filter could be designed, using the model to estimate the states required to calculate these terms. For maximum accuracy, the $\boldsymbol{\tau_l}$ can be estimated precisely using an observer or a Kalman filter, by estimating the $\ddot{\theta}_s$, $\dot{\theta}_s$. Moreover, the τ_m must be accurately known.

9.4 Future Work

Even though some tests were made, we cannot conclude yet on the actuator's performance. As shown in table 22, there are still some measurements to be made to have a complete picture. The torque and power output tests must be done, to measure the T/W, P/W and P/V ratios. The torque test was not done due to manufacturing delays, while power tests were a more complicated and rigorous to complete on time, as they required a position controller. A position controller based on the model of the system should be implemented. Furthermore, to check its performance, the torque controller needs to be implemented and tested using multiple tests on the real actuator. For this to be realised, system identification and parameter estimation is necessary. Techniques like grey box or black box can be adopted.

Then after the controller is designed, it needs to be tested and tuned in realistic conditions. It has to be able to reject disturbances and compensate friction. Only after the torque controller is optimized, a test should be made to identify the control bandwidth of the actuator. The actuator should be commanded to follow high torques at different frequencies to determine its control bandwidth. Moreover, safety features should be implemented to ensure safety.

In later stages, the torque and position/velocity controllers can be utilized to design an impedance or human-machine interaction controller. After these steps are completed, in later development stage, the

actuator will be installed on the exoskeleton frame, where a series of tests need to be made. High level control should be implemented, sensor integration. Overall power consumption should be optimized, and even energy saving should be considered. Next, once the robot is complete, it shall be tested on healthy subjects and lastly, on paraplegics. Only after the exoskeleton passes the tests it will be ready for the market.

Bibliography

[1] S. Federici, F. Meloni, M. Bracalenti, and M. L. De Filippis, “The effectiveness of powered, active lower limb exoskeletons in neurorehabilitation: A systematic review,” *NeuroRehabilitation*, vol. 37, no. 3, pp. 321–340, Nov. 2015.

[2] G. Chen, C. K. Chan, Z. Guo, and H. Yu, “A Review of Lower Extremity Assistive Robotic Exoskeletons in Rehabilitation Therapy,” *Crit. Rev. Biomed. Eng.*, vol. 41, no. 4–5, pp. 343–363, 2013.

[3] S. Federici, F. Meloni, and M. Bracalenti, “Gait Rehabilitation with Exoskeletons,” in *Handbook of Human Motion*, B. Müller, S. I. Wolf, G.-P. Brueggemann, Z. Deng, A. McIntosh, F. Miller, and W. S. Selbie, Eds. Cham: Springer International Publishing, 2016, pp. 1–38.

[4] M. Cenciarini and A. M. Dollar, “Biomechanical considerations in the design of lower limb exoskeletons,” in *IEEE International Conference on Rehabilitation Robotics*, 2011, pp. 1–6.

[5] J. M. Hollerbach, I. W. Hunter, and J. Ballantyne, “The Robotics Review 2,” O. Khatib, J. J. Craig, and T. Lozano-Pérez, Eds. Cambridge, MA, USA: MIT Press, 1992, pp. 299–342.

[6] N. A. Paine, “High-Performance Series Elastic Actuation,” PhD Thesis, University of Texas at Austin, 2014.

[7] F. Casolo, S. Cinquemani, and M. Cocetta, “On active lower limb exoskeletons actuators,” presented at the Mechatronics and Its Applications, 2008. ISMA 2008. 5th International Symposium on, 2008, pp. 1–6.

[8] J. M. Hollerbach, I. W. Hunter, and J. Ballantyne, “The Robotics Review 2,” O. Khatib, J. J. Craig, and T. Lozano-Pérez, Eds. Cambridge, MA, USA: MIT Press, 1992, pp. 299–342.

[9] J. L. Pons, Ed., *Wearable robots: biomechatronic exoskeletons*. Chichester: Wiley, 2008.

[10] H. van der Kooij, J. F. Veneman, and R. Ekkelenkamp, “Compliant Actuation of Exoskeletons,” in *Mobile Robots: towards New Applications*, A. Lazinica, Ed. I-Tech Education and Publishing, 2006.

[11] S. Wang *et al.*, “Design and Control of the MINDWALKER Exoskeleton,” *IEEE Trans. Neural Syst. Rehabil. Eng.*, vol. 23, no. 2, pp. 277–286, Mar. 2015.

[12] S. Wang, S. Wang, and C. Meijneke, “Mindwalker series elastic joint Modeling , Design , and Optimization of Mindwalker Series Elastic Joint,” *IEEE Int. Conf. Rehabil. Robot. Proc.*, vol. 2013, no. June, p. 6650381, 2013.

[13] J. Gancet *et al.*, “MINDWALKER: Going one step further with assistive lower limbs exoskeleton for SCI condition subjects,” 2012, pp. 1794–1800.

[14] M. K. Shepherd and E. J. Rouse, “Design and Validation of a Torque-Controllable Knee Exoskeleton for Sit-to-Stand Assistance,” *IEEEASME Trans. Mechatron.*, vol. 22, no. 4, pp. 1695–1704, Aug. 2017.

[15] H. Yu, S. Huang, G. Chen, and N. Thakor, “Control design of a novel compliant actuator for rehabilitation robots,” *Mechatronics*, vol. 23, no. 8, pp. 1072–1083, Dec. 2013.

[16] A. Zoss and H. Kazerooni, “Design of an electrically actuated lower extremity exoskeleton,” *Adv. Robot.*, vol. 20, no. 9, pp. 967–988, Jan. 2006.

[17] Hian Kai Kwa, J. H. Noorden, M. Missel, T. Craig, J. E. Pratt, and P. D. Neuhaus, “Development of the IHMC Mobility Assist Exoskeleton,” 2009, pp. 2556–2562.

[18] P. D. Neuhaus, J. H. Noorden, T. J. Craig, T. Torres, J. Kirschbaum, and J. E. Pratt, “Design and evaluation of Mina: A robotic orthosis for paraplegics,” 2011, pp. 1–8.

[19] N. C. Karavas, N. G. Tsagarakis, and D. G. Caldwell, “Design, modeling and control of a series elastic actuator for an assistive knee exoskeleton,” 2012, pp. 1813–1819.

[20] G. A. Day, “Synthesis and Design of a Bimodal Rotary Series Elastic Actuator,” Thesis, Virginia Tech, 2016.

[21] N. Aliman, R. Ramli, and S. M. Haris, “Design and development of lower limb exoskeletons: A survey,” *Robot. Auton. Syst.*, vol. 95, pp. 102–116, Sep. 2017.

[22] *Ekso Bionics - An exoskeleton bionic suit or a wearable robot that helps people walk again*. .

[23] *Rex Bionics - Reimagining Rehabilitation*. .

[24] “ReWalk 6.0 – Home,” *ReWalk – More Than Walking*. [Online]. Available: http://rewalk.com/. [Accessed: 24-Jan-2018].

[25] B. Chen *et al.*, “Recent developments and challenges of lower extremity exoskeletons,” *J. Orthop. Transl.*, vol. 5, pp. 26–37, Apr. 2016.

[26] R. Bogue, “Exoskeletons and robotic prosthetics: a review of recent developments,” *Ind. Robot Int. J.*, vol. 36, no. 5, pp. 421–427, 2009.

[27] B. Chen *et al.*, “Recent developments and challenges of lower extremity exoskeletons,” *J. Orthop. Transl.*, vol. 5, pp. 26–37, Apr. 2016.
[28] M. W. Whittle, “Clinical gait analysis: A review,” *Hum. Mov. Sci.*, vol. 15, no. 3, pp. 369–387, Jun. 1996.
[29] K. E. Zelik and A. D. Kuo, “Human walking isn’t all hard work: evidence of soft tissue contributions to energy dissipation and return,” *J. Exp. Biol.*, vol. 213, no. 24, pp. 4257–4264, Dec. 2010.
[30] Shiqian Wang, W. van Dijk, and H. van der Kooij, “Spring uses in exoskeleton actuation design,” 2011, pp. 1–6.
[31] G. Bovi, M. Rabuffetti, P. Mazzoleni, and M. Ferrarin, “A multiple-task gait analysis approach: Kinematic, kinetic and EMG reference data for healthy young and adult subjects,” *Gait Posture*, vol. 33, no. 1, pp. 6–13, Jan. 2011.
[32] Z. Yang, W. Gu, J. Zhang, and L. Gui, *Force control theory and method of human load carrying exoskeleton suit*, 1st ed. 2017. [Beijing, China] Berlin: National Defense Industry Press, 2017.
[33] D. A. Winter, *Biomechanics and Motor Control of Human Movement*. John Wiley & Sons, 2009.
[34] N. A. Paine, “High-performance series elastic actuation,” PhD Thesis, 2014.
[35] P. D. Neuhaus, J. H. Noorden, T. J. Craig, T. Torres, J. Kirschbaum, and J. E. Pratt, “Design and evaluation of Mina: A robotic orthosis for paraplegics,” presented at the Rehabilitation Robotics (ICORR), 2011 IEEE International Conference on, 2011, pp. 1–8.
[36] T. Vouga, R. Baud, J. Fasola, M. Bouri, and H. Bleuler, “TWIICE — A lightweight lower-limb exoskeleton for complete paraplegics,” presented at the Rehabilitation Robotics (ICORR), 2017 International Conference on, 2017, pp. 1639–1645.
[37] R. M. Crowder, *Electric drives and electromechanical systems*. Burlington: Butterworth-Heinemann, 2006.
[38] A. Zoss and H. Kazerooni, “Design of an electrically actuated lower extremity exoskeleton,” *Adv. Robot.*, vol. 20, no. 9, pp. 967–988, Jan. 2006.
[39] T. Zhang, M. Tran, and H. Huang, “Design and Experimental Verification of Hip Exoskeleton With Balance Capacities for Walking Assistance,” *IEEEASME Trans. Mechatron.*, vol. 23, no. 1, pp. 274–285, Feb. 2018.
[40] J. E. Pratt and B. T. Krupp, “Series Elastic Actuators for legged robots,” in *Proceedings of the SPIE*, 2004, pp. 135–144.
[41] C. Lee, S. Kwak, J. Kwak, and S. Oh, “Generalization of Series Elastic Actuator Configurations and Dynamic Behavior Comparison,” *Actuators*, vol. 6, no. 3, p. 26, Aug. 2017.
[42] J. P. Cummings, D. Ruiken, E. L. Wilkinson, M. W. Lanighan, R. A. Grupen, and F. C. Sup, “A Compact, Modular Series Elastic Actuator,” *J. Mech. Robot.*, vol. 8, no. 4, p. 041016, Apr. 2016.
[43] K. Anam and A. A. Al-Jumaily, “Active Exoskeleton Control Systems: State of the Art,” *Procedia Eng.*, vol. 41, pp. 988–994, 2012.
[44] W. Huang, “Shape Memory Alloys and their Application to Actuators for Deployable Structures,” Phd Dissertation, University of Cambridge, Peterhouse, 1998.
[45] L. Ionov, “Polymeric Actuators,” *Langmuir*, vol. 31, no. 18, pp. 5015–5024, May 2015.
[46] S. John, J. Sirohi, G. Wang, and N. M. Wereley, “Comparison of Piezoelectric, Magnetostrictive, and Electrostrictive Hybrid Hydraulic Actuators,” *J. Intell. Mater. Syst. Struct.*, vol. 18, no. 10, pp. 1035–1048, Oct. 2007.
[47] C. C. Hong, “Application of a magnetostrictive actuator,” *Mater. Des.*, vol. 46, pp. 617–621, Apr. 2013.
[48] A. J. Veale and S. Q. Xie, “Towards compliant and wearable robotic orthoses: A review of current and emerging actuator technologies,” *Med. Eng. Phys.*, vol. 38, no. 4, pp. 317–325, Apr. 2016.
[49] I. W. Hunter and S. Lafontaine, “A comparison of muscle with artificial actuators,” 1992, pp. 178–185.
[50] J. Varghese, A. V.m., R. P.k., and S. K.s., “A rotary pneumatic actuator for the actuation of the exoskeleton knee joint,” *Theor. Appl. Mech. Lett.*, vol. 7, no. 4, pp. 222–230, Jul. 2017.
[51] J. F. Veneman, “A Series Elastic- and Bowden-Cable-Based Actuation System for Use as Torque Actuator in Exoskeleton-Type Robots,” *Int. J. Robot. Res.*, vol. 25, no. 3, pp. 261–281, 2006.
[52] G. A. Pratt and M. M. Williamson, “Series elastic actuators,” in *Proceedings 1995 IEEE/RSJ International Conference on Intelligent Robots and Systems. Human Robot Interaction and Cooperative Robots*, 1995, vol. 1, pp. 399–406.
[53] M. Cempini *et al.*, “Relevance of Series-Elastic actuation in rehabilitation and assistance robotic: Two cases of study,” in *2015 IEEE 1st International Forum on Research and Technologies for Society and Industry, RTSI 2015 - Proceedings*, 2015, pp. 76–81.
[54] A. Calanca, R. Muradore, and P. Fiorini, “A Review of Algorithms for Compliant Control of Stiff and Fixed-Compliance Robots,” *IEEEASME Trans. Mechatron.*, vol. 21, no. 2, pp. 613–624, Apr. 2016.

[55] N. Paine, S. Oh, and L. Sentis, “Design and control considerations for high-performance series elastic actuators,” *IEEEASME Trans. Mechatron.*, vol. 19, no. 3, pp. 1080–1091, 2014.
[56] *IMSystems \textbar Technology*. .
[57] R. Ekkelenkamp, J. Veneman, and H. van der Kooij, “LOPES: a lower extremity powered exoskeleton,” 2007, pp. 3132–3133.
[58] M. Lauria, M.-A. Legault, M.-A. Lavoie, and F. Michaud, “Differential elastic actuator for robotic interaction tasks,” in *2008 IEEE International Conference on Robotics and Automation*, Pasadena, CA, USA, 2008, pp. 3606–3611.
[59] C. Lee and S. Oh, “Configuration and performance analysis of a compact planetary geared Elastic Actuator,” in *IECON 2016 - 42nd Annual Conference of the IEEE Industrial Electronics Society*, Florence, Italy, 2016, pp. 6391–6396.
[60] X. D. Wu, M. L. Bai, Y. Li, Q. H. Cao, and X. C. Du, “Analysis of Harmonic Gear Drive Efficiency Based on the 3D Simplified Model,” *Adv. Mater. Res.*, vol. 1006–1007, pp. 249–252, Aug. 2014.
[61] N. Hogan, “Stable execution of contact tasks using impedance control,” 1987, vol. 4, pp. 1047–1054.
[62] H. Zhang, S. Ahmad, and G. Liu, “Torque Estimation for Robotic Joint With Harmonic Drive Transmission Based on Position Measurements,” *IEEE Trans. Robot.*, vol. 31, no. 2, pp. 322–330, Apr. 2015.
[63] “| Harmonic Drive | Harmonic Drive.” [Online]. Available: http://www.harmonicdrive.net/downloads/catalogs. [Accessed: 14-Oct-2018].
[64] R. G. Budynas and J. K. Nisbett, *Shigley’s mechanical engineering design*, 9th ed. New York: McGraw-Hill, 2011.
[65] C. Lagoda, A. C. Schouten, A. H. A. Stienen, E. E. G. Hekman, and H. Van Der Kooij, “Design of an electric series elastic actuated joint for robotic gait rehabilitation training,” in *2010 3rd IEEE RAS and EMBS International Conference on Biomedical Robotics and Biomechatronics, BioRob 2010*, 2010, pp. 21–26.
[66] F. Sergi, D. Accoto, G. Carpino, N. L. Tagliamonte, and E. Guglielmelli, “Design and characterization of a compact rotary Series Elastic Actuator for knee assistance during overground walking,” in *2012 4th IEEE RAS & EMBS International Conference on Biomedical Robotics and Biomechatronics (BioRob)*, Rome, Italy, 2012, pp. 1931–1936.
[67] K. Nas, “Rehabilitation of spinal cord injuries,” *World J. Orthop.*, vol. 6, no. 1, p. 8, 2015.
[68] P. A. Costigan, K. J. Deluzio, and U. P. Wyss, “Knee and hip kinetics during normal stair climbing,” *Gait Posture*, vol. 16, no. 1, pp. 31–37, Aug. 2002.
[69] S. Kinoshita, R. Kiyama, and Y. Yoshimoto, “Effect of Handrail Height on Sit-To-Stand Movement,” *PLOS ONE*, vol. 10, no. 7, p. e0133747, Jul. 2015.
[70] L. Satria Adiputra, S. Parasuraman, A. Khan, and I. Elamvazuthi, “Bio mechanics of Desending and Ascending Walk,” *ElsevierProcedia Comput. Sci.*, vol. 76, 2015.
[71] U. Onen, F. M. Botsali, M. Kalyoncu, M. Tinkir, N. Yilmaz, and Y. Sahin, “Design and Actuator Selection of a Lower Extremity Exoskeleton,” *IEEEASME Trans. Mechatron.*, vol. 19, no. 2, pp. 623–632, Apr. 2014.
[72] M. Wisse, A. L. Schwab, and F. C. T. Van Der Helm, “Passive Dynamic Walking Model with Upper Body,” *Robotica*, vol. 22, no. 6, pp. 681–688, Nov. 2004.
[73] X. Jin, Y. Cai, A. Prado, and S. K. Agrawal, “Effects of exoskeleton weight and inertia on human walking,” in *2017 IEEE International Conference on Robotics and Automation (ICRA)*, 2017, pp. 1772–1777.
[74] H. Olsson, K. J. Åström, C. Canudas de Wit, M. Gäfvert, and P. Lischinsky, “Friction Models and Friction Compensation,” *Eur. J. Control*, vol. 4, no. 3, pp. 176–195, Jan. 1998.

Appendices

Appendix A: Clinical Gait data used for exoskeleton requirements

Degrees of freedom
The human leg has 8 degrees of freedom (DOFs), three in the hip and ankle and two on the knee joint. An optimal exoskeleton design utilizes only the DOFs needed to achieve the movements desired, to save mass and volume and energy. Actuating less DOFs typically means less weight. In our case, the desired movements are level-ground walking, sit-to-stand motion and stair ascending-descending. These movements are very common activities of daily living (ADL), which if are achieved, they can greatly improve a paraplegic's daily routine [67]. According to [29], [68], [69] the main DOFs used in these activities are the following:

- Hip flexion/extension (HFE)
- Knee flexion/extension (HFE)
- Ankle plantar flexion/ dorsi flexion (APD)
- Hip adduction/abduction (HAA)

Range of motion (ROM)
The actuator needs to be able to respond and produce the kinematic ranges of the joints. Considering that the main purpose of the exoskeleton is to assist in walking, the range of motion for normal walking is investigated. In rehabilitation exoskeletons that help a person regain walking ability, the ROM is usually the range for normal walking speed, plus a bit extra as a safety margin. The second use of the exoskeleton is to perform sit to stand action, thus this kind of motion is also investigated, to determine the angle ranges required to achieve this.

M. W. Whittle [29] recorded the joint angles of normal gait in the sagittal plane. From the Clinical Gait Analysis (CGA) data of [29] the required angles that define the range of motion were extracted.
Another requirement is climbing stairs (ascend-decend), thus the joint angles for this action are investigated too. The walking speed requirements have been investigated. The proposed exoskeleton has the requirements to enable paralyzed people to walk stable on level ground with a slow speed 0.8m/s and execute sit-to-stand movements.

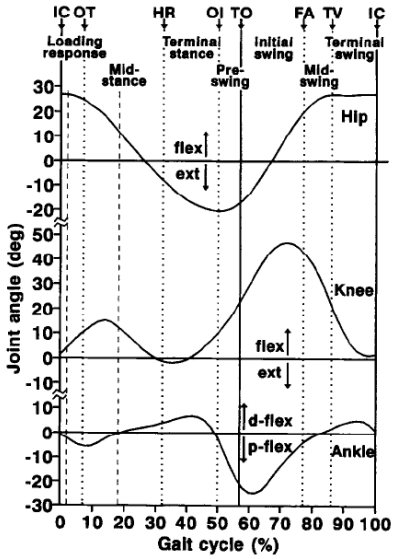

Figure 59 angles of normal gait in the sagittal plane (Whittle (1996)) [29]

Table 23 summarizes the kinematic Range of motion of human joints for different tasks, as obtained from literature [23],[24],[25], [70]. For the HAA and HIE, no data for the angles were found.

Table 23 Range of motion of human joints for different tasks

Joints' Range of motion (degrees)	*Hip Flex/ Extension*	*Knee Flex/ Extension*	*Ankle plantar/ dorsiflexion*	*Hip Ab/ Adduction*	*Hip Rotation*
ground - walking	from -15^o to +28^o	from -2^o to +50^o	from -7^o to +13^o	from -5^o to +5^o	from -20^o to +34^o
Sit to Stand	from 0^o to +100	from -3^o to +92^o	from -25^o to -0^o	N/A	N/A
Stairs ascending/decending	from 0^o to +45	from 0^o to +95^o	from -15^o to +15^o	N/A	N/A

According to the studies, the maximum torques for gait are almost 1 Nm/kg for knee and hip respectively. The required torque and power characteristics can be calculated by using the joint angle data and normalized joint torque data obtained from CGA database. Joint torque requirements for the actuators can be calculated by using

$$T_R = T_N . m_T$$

where T_R is the required joint torque, T_N is the normalized joint torque, and m_T is the total mass carried by the exoskeleton. We calculate power in a similar way from the normalized power graphs.

$$P_R = P_N . m_T$$

The total mass m_T is assumed to be the toal mass of the exoskeleton and the human ($m_T = m_{exo} + m_{user}$) where m_{exo} is the total mass of the exoskeleton including actuation, auxiliary equipment and battery, m_{user} is the mass of the user [71].

Exoskeleton weight

A portable exoskeleton should weigh as less as possible, because it has to carry its own mass plus the mass of the wearer. Also a lightweight design makes transport easier and adds less inertia to the patient. A larger exoskeleton inertia will increase the torque and power requirements. This means larger energy storage will be needed and it could result to greater power consumption. Moreover, according to [72] the walking motion is “a repetition of unstable forward falls”. For an exoskeleton design, it is very important that the swing leg must swing forward as fast as possible to “catch the fall”. To make this possible, the inertia of the exoskeletons’ limbs (especially the foot), must be as small as possible [9]. A study by [73] investigated the effects of the exoskeleton’s inertia on walking of healthy adults. It showed that “increasing the exoskeleton mass increases step length, decreases step height, and reduces maximum knee flexion”.

Estimating the exoskeleton’s weight is difficult because it depends on several design factors, like the actuators weight and the materials of the structure. By designing the actuators in a smart and efficient way, the desired mass reduction can be achieved. A commercialized exoskeleton, Indigo, has achieved an overall mass of 12 kg, which shows that this limit (or even less) is attainable [2].
Aassuming that a heavy person can be up to 100 kg and the exoskeleton mass will be 12kg, a total of 112kg is assumed

Velocity, torque and power requirements

The joint torque requirements for walking with 0.8 m/s according to [36], are 0.6 Nm/kg for HFE and 0.75 Nm for KFE. For walking, joint power requirements data were obtained from [29] [30].

A study by [36] measured gait data for the walking speeds 0.8 and 1,2 m/s shown in Figure 60. Figure 60 provides all the information needed; normalized angles, velocities, torques and power for all the degrees of freedom of interest in the hip and knee joints. These are presented in Table 24.

Table 25 and Table 26 present the peak torques and powers of human joints for different tasks, as obtained from literature [36], [37], [38]. It is clear that stairs ascend/descend is the most power demanding task. Note that these are the torque and power requirements at the joints. That means the actual requirements for the actuators will be higher. To calculate the transmission efficiency, the losses due to friction and the

actuator efficiency should be considered. One can notice that the stair climbing task has the highest power demands for all joints.

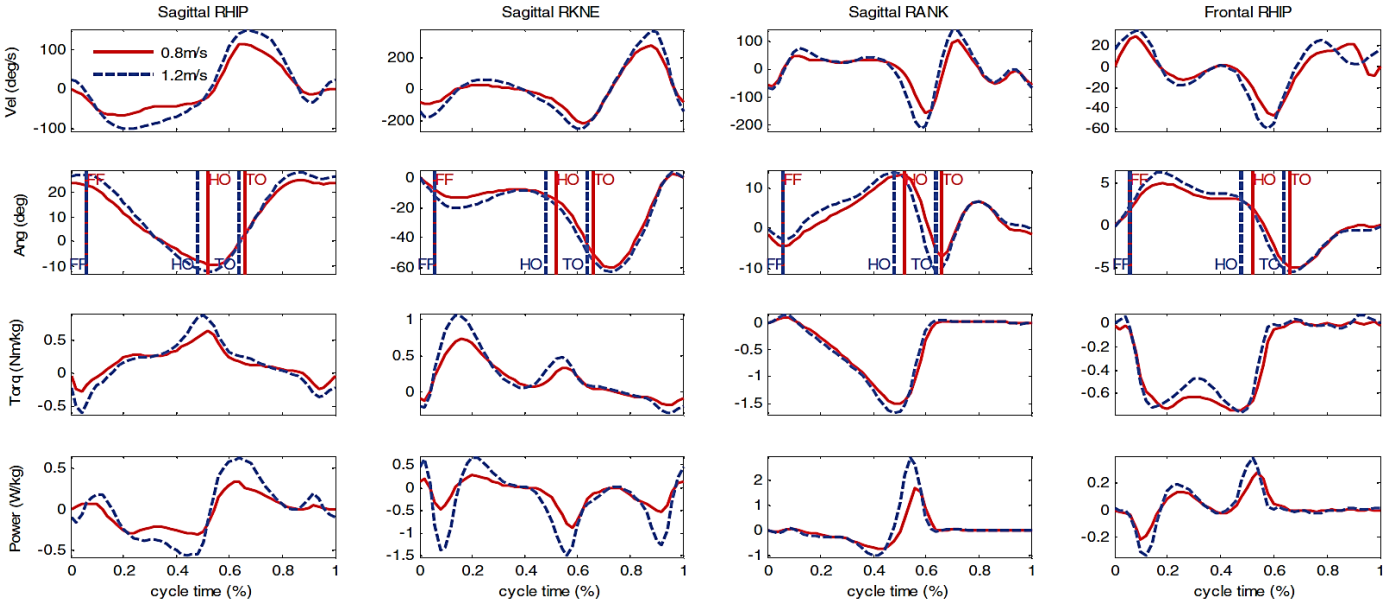

Figure 60 Normalized Gait data for two different speeds. RHIP = right hip, RKNE= right knee, RANK = right ankle [37]

Regarding able-bodied sit-to-stand (STS) motion, the normalized peak knee torques are typically reported in the range of 0.5–0.8 Nm/kg.

Table 24 Maximum velocities of joints for different tasks

Velocity (rad/s)	*Hip Flex/Extension*	*Knee Flex/Extension*	*Ankle plantarflex/dorsiflexion*	*Hip Ab/Adduction*
ground - walking	**2**	**4.8**	**2.7**	**0.87**
Sit to Stand	1.4	1.74	0.35	N/A
Stairs ascend/descend	1.8	2.4	1.7	N/A

From table 3 it can be observed that the maximum joint velocities occur when walking.

Table 25 Generalized maximum torque of joints

Torque (Nm/kg)	*Hip Flex/Extension*	*Knee Flex/Extension*	*Ankle plantar/ dorsiflexion*	*Hip Ab/Adduction*
ground - walking	0.6	0.75	**-1.5**	-0.75
Sit to Stand	**0.75**	0.85	0.4	N/A
Stairs ascend/ descend	0.6	**0.9**	1.2	0.76

Table 26 Generalized maximum power of joints

Power (W/kg)	*Hip Flex/Extension*	*Knee Flex/Extension*	*Ankle plantar/ dorsiflexion*	*Hip Ab/Adduction*
ground - walking	0.5	0.9	1.7	0.3
Sit to Stand	1	1.3	0.15	N/A
Stairs ascend/descend	**1**	**2.5**	**2**	N/A

Torque Bandwidth Requirements

The force bandwidth shows the maximum frequency to which the human joints can generate the desired torques. The minimum torque bandwidth is determined by the Power Spectral Density (PSD) of the joint torques from [32]. (PSD shows the power in the signal as a function of frequency). During level-ground walking, 99% of the power in kinematic signals is contained below 6 Hz [32]. Regarding that more than 95%

of the PSD of the hip and knee joint torque is in the frequency range between 0 and 5Hz, thus a minimum bandwidth of 5Hz is defined as a requirement to torque control for the full torque range.

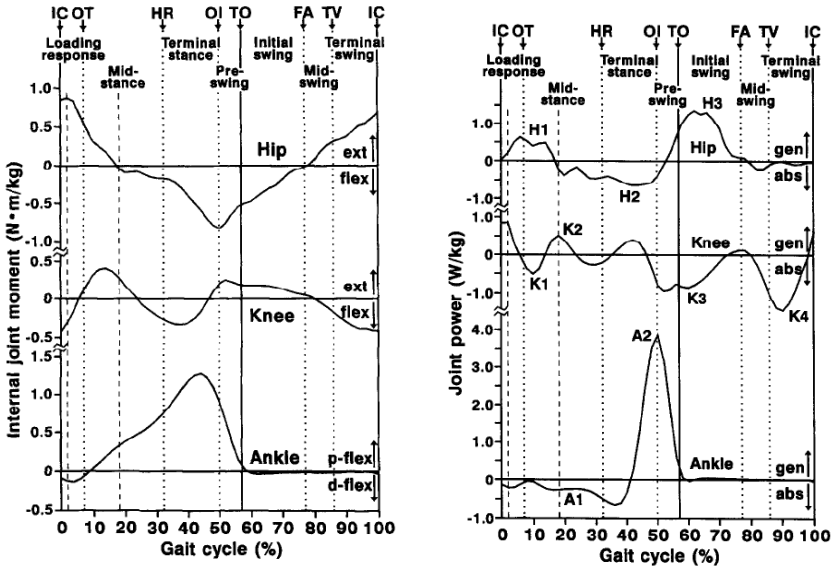

Figure 61 Normalized Internal torques and power of hip, knee and ankle joints during a single gait cycle (Whittle (1996))

Appendix B: Kinematics of exoskeleton

Kinematic analysis of human gait
Kinematics is the study of motion without regard to forces that cause it. Kinematic analysis provides all the possible physical positions, velocities and accelerations of all the parts of the linkage with respect to the time as it goes through a cycle.

Lumped model:
The human body can be considered as a link of rigid segments. The exoskeleton is modelled in the following way: it is assumed to be fixed on the human legs, therefore the human segments and the exoskeleton behave as one segment.

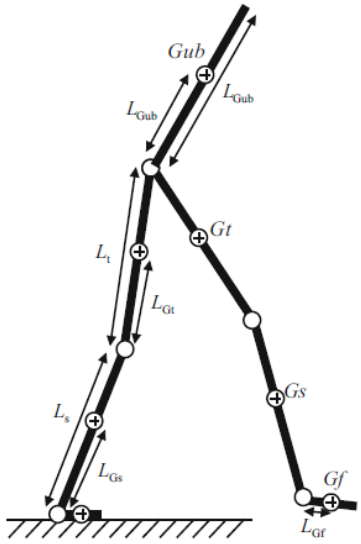

Figure 62 Lumped Exoskeleton model

Transformation matrix
The transformation matrix between the inertial frame (the global frame) and a segment frame provides orientation (angular position) information of the segment the reference frame is attached to. Any vector expressed in the segment frame can be transformed by the transformation matrix to its expression in the global frame.

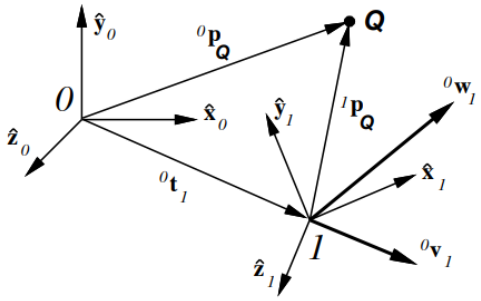

Figure 63 Vector transformation

The position vector of each segment's center of mass is defined as:

$$ {}^0\mathbf{p}_Q = {}_0R_1\ {}^1\mathbf{p}_Q + {}^0\mathbf{t}_1 $$

Where R is the rotation matrix of the link with respect to global frame, p is the position of the center of mass and t the initial position.
By differentiating the position vectors, the velocities of the Centers of mass of the segments are calculated as:

$$ {}^{0}\mathbf{v}_{Q} = {}_{0}R_{1}\,{}^{1}\dot{\mathbf{p}}_{Q} + ({}^{0}\boldsymbol{\omega}_{1} \times {}_{0}R_{1}\,{}^{1}\mathbf{p}_{Q}) + {}^{0}\mathbf{v}_{1} $$

Where ω is the rotational velocity of each segment, and $0V_1$ the linear velocity of the previous joint

As for the linear acceleration vector V_dot, it is obtained by double numerical differentiation of the position vector of the centre of gravity. The position vector is obtained by linearly combining the positions of the proximal and distal joint centres, respectively denoted as p and d

Hence, the expression of the acceleration vector of the centre of gravity as observed from the global frame is:

$$ \begin{aligned} {}^{0}\dot{\mathbf{v}}_{Q} = {} & {}_{0}R_{1}\,{}^{1}\ddot{\mathbf{p}}_{Q} + ({}^{0}\boldsymbol{\omega}_{1} \times {}_{0}R_{1}\,{}^{1}\dot{\mathbf{p}}_{Q}) + ({}^{0}\dot{\boldsymbol{\omega}}_{1} \times {}_{0}R_{1}\,{}^{1}\mathbf{p}_{Q}) \\ & + ({}^{0}\boldsymbol{\omega}_{1} \times {}_{0}R_{1}\,{}^{1}\dot{\mathbf{p}}_{Q}) + ({}^{0}\boldsymbol{\omega}_{1} \times {}^{0}\boldsymbol{\omega}_{1} \times {}_{0}R_{1}\,{}^{1}\mathbf{p}_{Q}) + {}^{0}\dot{\mathbf{v}}_{1} \end{aligned} $$

Appendix C: Information about Speed Reducers

Rotary Drives

Several Gears including planetary, cycloidal and strain wave gears (harmonic drives) were investigated. From these gear reducers, the best options considered are the harmonic drives. The harmonic drives and the cycloids have the highest reduction ratio, which is very important in the exoskeleton joints. The planetary gears have high friction, and also the reduction ratios are not very high. Gear efficiencies depend on reduction ratio, with higher ratios reducing the efficiency.

Figure 64 Different types of rotary gears

A simulation study by Sensinger J, 2012 compares harmonic drive with cycloidal for robotic applications [86]. Cycloid drive designs were found to be thinner, more efficient, and to have lower reflected inertia than corresponding harmonic drives. However, the cycloid designs had larger gear ratio ripple and substantial backlash, and they could not meet the maximum gear ratio provided by the corresponding harmonic drives in 1/3 of the cases.

Cycloids have recently been improved in regards to weight and packaging to become competitive [33]. However, a major issue is that there are poor commercial options that meet the torque and weight requirements. Harmonic drives are very lightweight gearheads with a wide range of available torques that can be purchased and have several options that could be customized for almost any motor.

Strain wave gear working principle

The harmonic drive consists of 3 parts. Wave generator is the driven part. The ellipse shape of the generator is fitted with a specially design of ball bearing. The Flex spline is a high-strength flexible component with external teeth and transmits high loads.

The circular spline has internal teeth, but has 2 more teeth than flex. The flax spline takes the elliptical shape of the wave generator. When wave generator rotates, causes the flex spline to deform radially. Because the flex has 2 teeth less, the rotation of the WG, causes relative motion between FS and CS. The WG can rotate very fast, while the resulting motion is very slow. This leads to very high reduction ratios. Reduction ratio is defined as:

$$N = \frac{(n_{FS} - n_{CS})}{n_{FS}}$$

Where n_{FS} = flex spline teeth, n_{CS} = Circular spline teeth

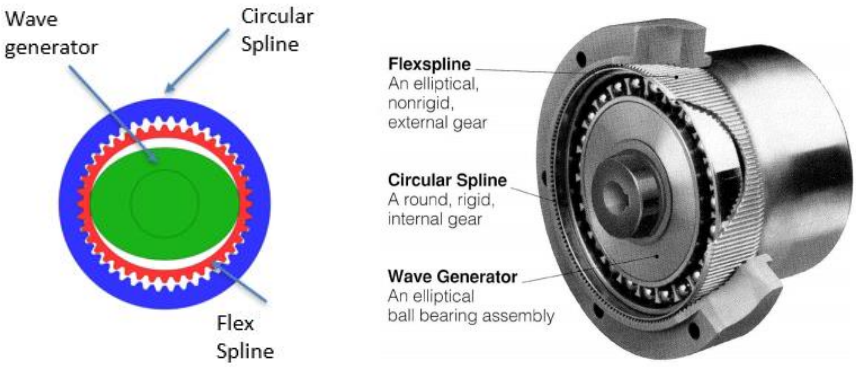

Figure 65 Harmonic gearbox (cup shaped) components [41]

Linear drives

Linear transmissions were also investigated, including Lead screws, roller and ball screws. From those, the ball screws are a very appealing reduction type too, because of high efficiency. Ballscrews have theoretical efficiency 95%. This means the friction is and energy losses will be minimal. Moreover, they are backdrivable which is also desired. Exoskeletons with linear actuators, like Mindwalker and LOPES prefer ball screws [20], [28]. Some modern exoskeletons like a knee exoskeleton from Shepherd et al. (2017) use ball screws and many bipedal robots like UT-Series elastic actuator also [15] [42].
A ball screw is the power is transmitted to the nut via ball bearings located in the thread on the nut. Ball screws have much less friction than lead and are preferred in precision applications [41].

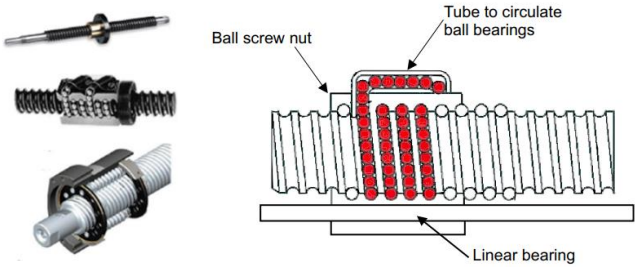

Figure 66 Different types of linear drives

In the screw drives, as the screw is rotated, the nut, which is constrained from rotating, moves along the thread. The distance moved by one turn of the lead screw is called lead. The pitch is the distance between the threads. In the case of a single start thread, the lead is equal to the pitch; however , the pitch is smaller than the lead on a multi-start thread [41]. In a lead screw there is direct contact between the screw and the nut, and this leads to relatively high friction. A ball screw is identical in principle to a lead screw, but the power is transmitted to the nut via ball bearings located in the thread on the nut. Ball screws have much less friction than lead and are preferred in precision applications [88].

Table 27 Efficiencies for lead and ball screws [41]

System type	Efficiency
Ball screw	0.95
Lead screw	0.90
Rolled-ball lead screw	0.80
ACME threaded lead screw	0.40

In a lead screw there is direct contact between the screw and the nut, and this leads to relatively high friction. A ball screw is identical in principle to a lead screw, but the power is transmitted to the nut via ball bearings located in the thread on the nut. Ball screws have much less friction than lead and are preferred in precision applications [41].

The linear speed of the load is determined by the rotational speed of the screw and the screw's lead. The relationship between the rotational and linear speed for both the lead and ball screw is given by:

$$\Omega_L = \frac{2\pi\, V_L}{L}$$

Where Ω_L is the rotational speed in rev min^{-1}, V_L is the linear speed in meters*min^{-1}, and L is the lead (in metres). The inertia of the complete system is the sum of the screw inertia J_s and the reflected inertia of the load J_L

$$J_{tot} = J_s + J_L$$

Where

$$J_s = \frac{M_s r^2}{2}\,, \qquad J_L = M_L \left(\frac{L}{2\pi}\right)^2$$

where M_L is the load's mass in kg, M_s is the screw's mass in kg and r is the radius of the lead screw (in metres).
In addition, the static forces, both frictional and the forces required by the load, need to be converted to a torque at the lead screw's input. The torque T_L caused by external forces, F_L, will result in a torque requirement of

$$T_L = \frac{LF_L}{2\pi}$$

and a possible torque resulting from slideway friction of

$$T_f = \frac{LM_L g cos\theta\, \mu}{2\pi}$$

where θ is the inclination of the slideway. It has been assumed so far that the efficiency of the lead screw is one hundred per cent. In practice, losses will occur and the torques will need to be divided by the lead-screw efficiency, ε. Thus the required Torque is:

$$T_r = \frac{T_L + T_f}{\varepsilon}$$

Ballscrew Selection
The requirements for the ballscrew are Efficiency, Dynamic load rating, Static load rating, Screw & nut weight. The reduction ratio depends on the lever arm d and the lead L. The moment arm depends on the linkage structure. Thus, by assuming a maximum moment arm 0.06 m we can calculate the reduction ratio.

$$N = \frac{2\pi d}{p_h}$$

Practical Efficiency is given by SKF as

$$\eta_p = 0.9\,\eta$$

Where η the theoretical efficiency defined as

$$\eta = \frac{0.9}{1 + \frac{\pi d \mu}{p_h}}$$

Where μ = 0,006 is the friction coefficient, d = nominal diameter of screw shaft [mm], p_h = lead [mm]

	Name	*diameter*	*dynamic load rating (kN)*	*static load rating (kN)*	*Lead (m)*	*Max Reduction ratio (d=0.06)*	*Nut Weight (kg)*	*Screw Weight (kg) for 0.12m*	*total weight (kg)*	*Practical efficiency 0.9η_theoretical*
SKF	SD/BD 10x4 R	0.01	4.5	5.5	0.004	94.25	0.040	0.052	0.092	0.859
SKF	**SD/BD 12x4 R**	**0.012**	**4.9**	**6.6**	**0.004**	94.25	**0.066**	**0.085**	**0.151**	**0.852**
SKF	SD/BD 12x5 R	0.012	4.2	5.4	0.005	75.40	0.058	0.085	0.143	0.861
THK	SDA1510-2.8 (d15)	0.015	5.5	7.8	0.01	37.70	0.16	0.158	0.318	0.875
THK	SDA1520-3.6 (d15)	0.015	6.4	10.3	0.02	18.85	0.18	0.162	0.342	0.887
thomson	RM 10 03 Z3 – 0120 – F L X – MK S – K X	0.01	4.8	8.6	0.003	125.66	0.077	0.070	0.147	0.847
thomson	RM 10 04 Z3 – 0120 – F L X – MK S – K X	0.01	4.2	7.4	0.004	94.25	0.077	0.070	0.147	0.859

From the table we can see that the SKFs are quite light and efficient. All ballscrews have close efficiency between 85-89%. The SKFs however can achieve good reduction ratios, and they can handle a significant amount of load.

Appendix D: Equations of motion and Transfer functions of SEA configurations

FSEA Differential & Algebraic Equations in Matrix form:
The ideal torque relationship between the transmission elements is:

$$\tau_{wg-fs} = \tau_{cs-fs} = \frac{\tau_{cs}}{(N+1)}$$

The Differential & Algebraic Equations are:

$$J_{rw}\ddot{\theta}_m + B_{rw}\dot{\theta}_m = \tau_m + \frac{1}{(N+1)}\tau_{cs}$$
$$J_{cs}\ddot{\theta}_s + B_{cs}\dot{\theta}_s + K_s\theta_s = -\tau_{cs}$$
$$J_l\ddot{\theta}_l + B_l\dot{\theta}_l = \tau_l - \tau_{cs}$$
$$\frac{\ddot{\theta}_m}{N+1} - \ddot{\theta}_s - \ddot{\theta}_l = 0$$

Then the DAE become:

$$\begin{bmatrix} M_{ij} & D_{k,i} \\ D_{k,j} & 0_{kk} \end{bmatrix}\begin{bmatrix} \ddot{\theta}_j \\ \tau_{cs} \end{bmatrix} + \begin{bmatrix} B_{ij} & 0_{k,i} \\ 0_{k,j} & 0_{kk} \end{bmatrix}\begin{bmatrix} \dot{\theta}_j \\ \tau_{cs} \end{bmatrix} = \begin{bmatrix} \tau_i - K_s\theta_s D_{v,i} \\ 0 \end{bmatrix}$$

Where Mass matrix $M_{ij} = \begin{bmatrix} J_{rw} & 0 & 0 \\ 0 & J_{cs} & 0 \\ 0 & 0 & J_l \end{bmatrix}$

Where Damping matrix $B = \begin{bmatrix} B_{rw} & 0 & 0 \\ 0 & B_{cs} & 0 \\ 0 & 0 & B_l \end{bmatrix}$

Partial derivatives (Jacobian) of constraints with respect to time: $D_{k,i} = \begin{bmatrix} \frac{1}{N+1} & -1 & -1 \end{bmatrix}^T$

$$D_{k,j} = \left(D_{k,i}\right)^T$$

External torques $\tau_i = [\,\tau_m \;\; 0 \;\; \tau_l]^T$

The relationship $D_{v,i}$ of the spring acting on the bodies in terms of the coordinates of the center of mass of the bodies. $D_{v,i} = [0 \;\; -1 \;\; 0]^T$

FSEA Transfer functions
The Open Loop Transfer functions are obtained as follows:
The **output-input** torque transfer function is described as:

$$\frac{T_{cs}(s)}{T_m(s)} = \frac{P_m(s)}{(N+1)D(s)}$$

The transfer function from output torque to spring deformation given as

$$\frac{\Theta_s(s)}{T_l(s)} = \frac{P_l(s)P_s(s)}{(N+1)D(s)}$$

The Impedance is described by the transfer function of the load torque vs output angle given by:

$$\frac{T_l(s)}{\Theta_l(s)} = \frac{D(s)}{P_l(s)(P_m(s)N^{-2} + P_s)}$$

Where

$$D(s) = P_l(s) + (N+1)^{-2}P_m(s) + P_s(s)$$

TFSEA Differential & Algebraic Equations in Matrix form:

The ideal torque relationship between the transmission elements is:

$$\tau_{wg-fs} = \tau_{cs-fs} = \frac{\tau_{cs}}{(N+1)}$$

The Differential & Algebraic Equations are:

$$J_{rw}\ddot{\theta}_m + B_{rw}\dot{\theta}_m = \tau_m + \frac{1}{(N+1)}\tau_{cs}$$
$$J_{fs}\ddot{\theta}_s + B_{fs}\dot{\theta}_s + K_s\theta_s = -\frac{N}{(N+1)}\tau_{cs}$$
$$J_l\ddot{\theta}_l + B_l\dot{\theta}_l = -\tau_{cs} + \tau_l$$
$$\frac{\ddot{\theta}_m}{N+1} - \frac{N}{(N+1)}\ddot{\theta}_s - \ddot{\theta}_l = 0$$

Then the DAE become:

$$\begin{bmatrix} M_{ij} & D_{k,i} \\ D_{k,j} & 0_{kk} \end{bmatrix}\begin{bmatrix} \ddot{\theta}_j \\ \tau_{cs} \end{bmatrix} + \begin{bmatrix} B_{ij} & 0_{k,i} \\ 0_{k,j} & 0_{kk} \end{bmatrix}\begin{bmatrix} \dot{\theta}_j \\ \tau_{cs} \end{bmatrix} = \begin{bmatrix} \tau_i - K_s\theta_s D_{v,i} \\ 0 \end{bmatrix}$$

Where Mass matrix $M_{ij} = \begin{bmatrix} J_{rw} & 0 & 0 \\ 0 & J_{fs} & 0 \\ 0 & 0 & J_l \end{bmatrix}$

Where Damping matrix $B = \begin{bmatrix} B_{rw} & 0 & 0 \\ 0 & B_{fs} & 0 \\ 0 & 0 & B_l \end{bmatrix}$

Partial derivatives (Jacobian) of constraints with respect to time: $D_{k,i} = \left[\frac{1}{N+1} \; -\frac{N}{(N+1)} \; -1\right]^T$

$$D_{k,j} = \left(D_{k,i}\right)^T$$

External torques $\tau_i = [\,\tau_m \; 0 \;\; \tau_l]^T$

The relationship $D_{v,i}$ of the spring acting on the bodies in terms of the coordinates of the center of mass of the bodies. $D_{v,i} = [0 \; -1 \;\; 0]^T$

RFSEA Transfer functions

The Transfer functions are obtained as follows:
The output-input torque transfer function is described as:

$$\frac{T_{cs}(s)}{T_m(s)} = \frac{(N+1)P_m(s)}{D(s)}$$

To quantify this force measurement and response characteristic, the transfer function from external force to spring deformation given as

$$\frac{\Theta_s(s)}{T_l(s)} = \frac{N(N+1)P_l(s)P_s(s)}{D(s)}$$

The Impedance is described by the transfer function of the External load vs output angle given by:

$$\frac{T_l(s)}{\Theta_l(s)} = \frac{D(s)}{P_l(s)(P_m(s) + N^2P_s(s))}$$

Where

$$D(s) = N^2P_s(s) + (N+1)^2P_l(s) + P_m$$

RFSEA Differential & Algebraic Equations in Matrix form:

The ideal torque relationship between the transmission elements is:

$$\tau_{wg-fs} = \tau_{cs-fs} = \frac{\tau_{cs}}{(N+1)}$$

The Differential & Algebraic Equations are:

$$J_{rw}(\ddot{\theta}_m + \ddot{\theta}_s) + B_{rw}(\dot{\theta}_m + \dot{\theta}_s) = \tau_m + \frac{1}{(N+1)}\tau_{cs}$$

$$J_{fs}\ddot{\theta}_s + B_{fs}\dot{\theta}_s + K_s\theta_s = -\frac{N}{(N+1)}\tau_{cs} - \tau_m$$

$$J_l\ddot{\theta}_l + B_l\dot{\theta}_l = -\tau_{cs} + \tau_l$$

$$\frac{\ddot{\theta}_m}{N+1} - \frac{N}{(N+1)}\ddot{\theta}_s - \ddot{\theta}_l = 0$$

Then the DAE become:

$$\begin{bmatrix} M_{ij} & D_{k,i} \\ D_{k,j} & 0_{kk} \end{bmatrix}\begin{bmatrix} \ddot{\theta}_j \\ \tau_{cs} \end{bmatrix} + \begin{bmatrix} B_{ij} & 0_{k,i} \\ 0_{k,j} & 0_{kk} \end{bmatrix}\begin{bmatrix} \dot{\theta}_j \\ \tau_{cs} \end{bmatrix} = \begin{bmatrix} \tau_i - K_s\theta_s D_{v,i} \\ 0 \end{bmatrix}$$

Where Mass matrix $M_{ij} = \begin{bmatrix} J_{rw} & J_{rw} & 0 \\ 0 & J_{fs} & 0 \\ 0 & 0 & J_l \end{bmatrix}$

Where Damping matrix $B = \begin{bmatrix} B_{rw} & B_{rw} & 0 \\ 0 & B_{fs} & 0 \\ 0 & 0 & B_l \end{bmatrix}$

Partial derivatives (Jacobian) of constraints with respect to time: $D_{k,i} = \left[\frac{1}{N+1} \; -\frac{N}{(N+1)} \; -1\right]^T$

$$D_{k,j} = \left(D_{k,i}\right)^T$$

External torques $\tau_i = [\,\tau_m \;\; -\tau_m \;\; \tau_l]^T$

The relationship $D_{v,i}$ of the spring acting on the bodies in terms of the coordinates of the center of mass of the bodies. $D_{v,i} = [0 \;\; -1 \;\; 0]^T$

TFSEA Transfer functions

The Transfer functions are obtained as follows:

The output-input torque transfer function is described as:

$$\frac{T_{cs}(s)}{T_m(s)} = \frac{(N+1)(P_m(s) - NP_s(s))}{D(s)}$$

To quantify this force measurement and response characteristic, the transfer function from external force to spring deformation given as

$$\frac{\Theta_s(s)}{T_l(s)} = \frac{N(N+1)P_l(s)P_s(s)}{D(s)}$$

The Impedance is described by the transfer function of the External load vs output angle given by:

$$\frac{T_l(s)}{\Theta_l(s)} = \frac{D(s)}{P_l(s)(P_m(s) + N^2P_s(s))}$$

Where

$$D(s) = N^2P_s(s) + (N+1)^2P_l(s) + P_m$$

Appendix E: Calculation of Non-linear frictions

In the TFSEA model, in section 3.2, The simplified torque model considers some non-linear friction terms. These include bearing frictions and gear-tooth interface of the harmonic drive's gears. This section explains how these terms were calculated.

The friction equation considers the following physical phenomena:

- Stribeck friction at low velocities
- Coulomb friction

Viscous friction is included in the linear terms.
It calculates the possible torque resulting from slideway friction [74]

$$f_m = \underbrace{\left(\tau_S - \tau_{C_m}\right) exp\left(-\left(\frac{\dot{\theta}_m}{\omega_s}\right)^2\right) sign(\dot{\theta}_m)}_{Stribeck\ friction} + \underbrace{\tau_{C_m} tanh\left(\frac{\dot{\theta}_m}{\omega_C}\right)}_{Coulomb}$$

$$f_{cs} = \underbrace{\left(\tau_S - \tau_{C_j}\right) exp\left(-\left(\frac{\dot{\theta}_l}{\omega_s}\right)^2\right) sign(\dot{\theta}_l)}_{Stribeck\ friction} + \underbrace{\tau_{C_j} tanh\left(\frac{\dot{\theta}_l}{\omega_C}\right)}_{Coulomb}$$

Where $\tau_C = F_{eq} * \mu * \frac{d_b}{2}$ is the coulomb friction
F_{eq} the Equivalent Load on the bearing
μ the Coefficient of friction (typically 0.0015 for ball bearings)
d_b the Pitch diameter of bearing
$(\tau_S - \tau_C)$ additional stiction torque
ω_s the Stribeck velocity threshold
ω_C Coulomb velocity threshold

The exponential function used in the Stribeck portion of the force equation is continuous and decays at velocity magnitudes greater than the breakaway friction velocity.
The hyperbolic tangent function used in the Coulomb portion of the force equation ensures that the equation is smooth and continuous through v = 0, but quickly reaches its full value at nonzero velocities []

Appendix F: TFSEA Parametric analysis

A parametric analysis was made to investigate how the TFSEA's behaviour changes by varying different parameters. In this section, only the TFSEA is analysed, since it was the one selected for design. The FRFs examined are torque transmissibility, torque sensitivity and impedance.

Effects of Load inertia J_l

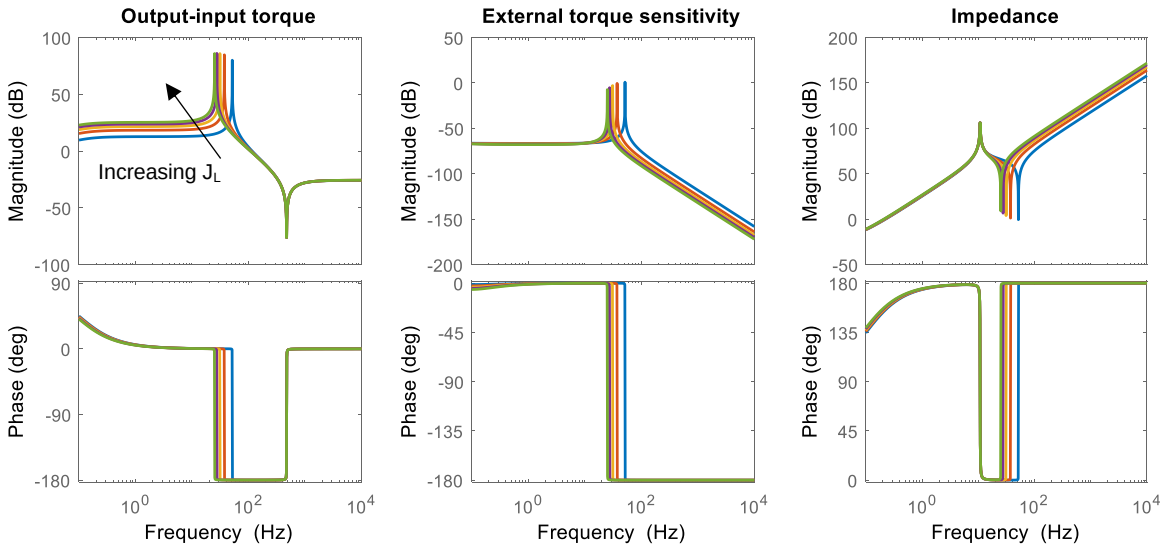

Figure 67 Effects of varying load inertia

In a real application, the exoskeleton will be used with different users, thus the load inertia is different for each. Moreover, the inertia changes for different robot postures, and hence it is important to know how the system will behave. Plotting for a wide range of load inertias we can observe how the TFSEA would respond to these changes. The FRFs are shown in figure 67. As expected, decreasing the load inertia increases the transmissibility and sensitivity bandwidths. Thus, a design goal is to decrease the actuators' output inertia. However, in this application the load inertia depends on the masses of the human legs' segments, which cannot be altered. The human limb's inertias are much larger than the actuator's link. Another observation is that high inertia increases the torque transmissibility magnitude. This means that as the inertia increases, the transmitted torque ratio becomes larger.
In the impedance plot, it can be seen that the anti-resonant frequency increase as the inertia decreases, which means the TFSEA becomes compliant in higher frequencies.

Effects of Spring Constant K_s

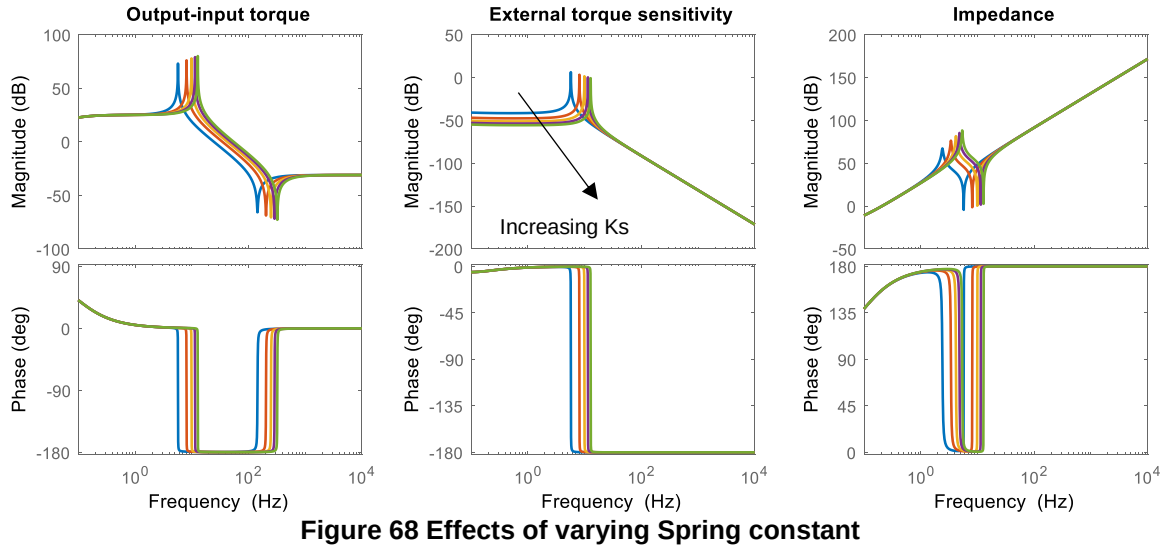

Figure 68 Effects of varying Spring constant

Next, the effect of stiffness on the bandwidth was examined. It is well known that spring with high stiffness allows for higher bandwidth of torque control. By plotting the FRF with varying spring rates, we can observe how the system behaves at different stiffness.
It is noticeable that increasing the Stiffness, increases the range of Transmissibility, Sensitivity bandwidths. That means we can measure and transmit torques at higher frequencies.
Moreover, the motion becomes impeded at higher frequency. These observations conclude that, to increase the performance a high stiffness is needed.

However, the spring constant is a trade-off between SEAs. As seen in the middle graph, the torque sensitivity magnitude becomes lower with a higher spring constant, the magnitude decreases, which means the spring deformation becomes smaller with respect to external force.
For using a stiffer spring, we can measure at higher frequencies, but it also means that a high-resolution encoder might be needed to measure this deflection. The conclusion is that higher stiffness is better, as it increases all ranges, but a high-resolution encoder is needed.

Effects of inertia added on the Spring, J_s

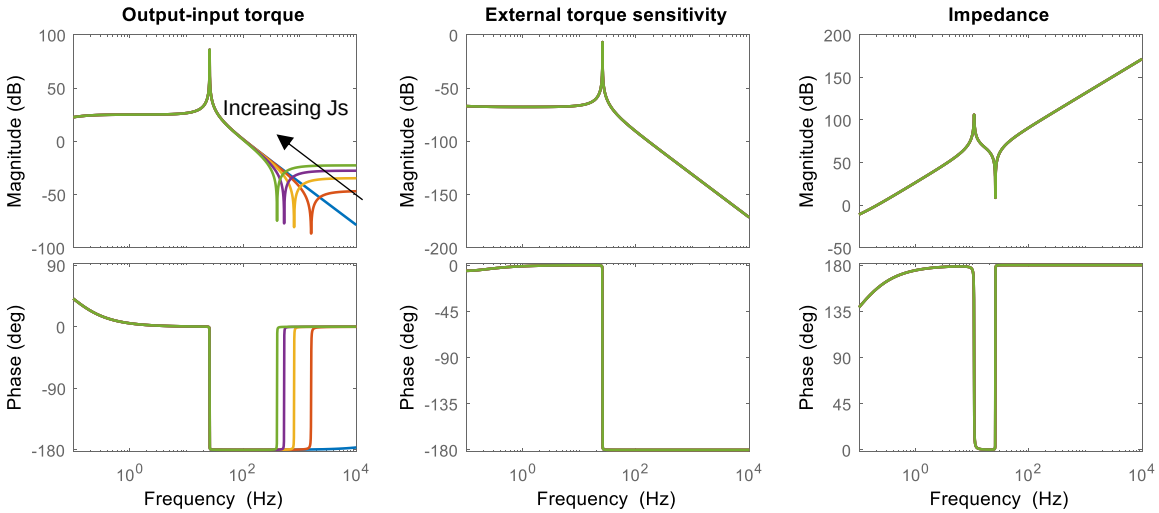

Figure 69 Effects of Increasing Spring inertia

In these graphs, we can observe the effect of the spring inertia. One can notice that when the Spring Inertia is negligible (close to zero), the system behaves like a typical 2nd order underdamped system. That is understood because two poles in the characteristic polynomial disappear. But when increasing the spring inertia, we can see the antiresonance occurring at high frequencies. For increasing the Js the antiresonance occurs in earlier frequency. The Spring sensitivity and the SEA impedance are not affected by the spring's Inertia.